TARGET DETECTION AND IMAGING ON PASSIVE BISTATIC RADAR SYSTEMS

A THESIS

SUBMITTED TO THE DEPARTMENT OF ELECTRICAL AND

ELECTRONICS ENGINEERING

AND THE GRADUATE SCHOOL OF ENGINEERING AND SCIENCE

OF BILKENT UNIVERSITY

IN PARTIAL FULFILLMENT OF THE REQUIREMENTS

FOR THE DEGREE OF

MASTER OF SCIENCE

By

Rasim Akın Sevimli

September, 2014

I certify that I have read this thesis and that in my opinion it is fully adequate, in scope and in quality, as a thesis for the degree of Master of Science.

Prof. Dr. A. Enis Çetin (Advisor)

I certify that I have read this thesis and that in my opinion it is fully adequate, in scope and in quality, as a thesis for the degree of Master of Science.

Prof. Dr. Orhan Arıkan

I certify that I have read this thesis and that in my opinion it is fully adequate, in scope and in quality, as a thesis for the degree of Master of Science.

Prof. Dr. Uğur Güdükbay

Approved for the Graduate School of Engineering and Science:

Prof. Dr. Levent Onural
Director of the Graduate School

ABSTRACT

TARGET DETECTION AND IMAGING ON PASSIVE BISTATIC RADAR SYSTEMS

Rasim Akın Sevimli
M.S. in Electrical and Electronics Engineering
Supervisor: Prof. Dr. A. Enis Çetin
September, 2014

Passive Bistatic Radar (PBR) systems have become more popular in recent years in many research communities and countries. Papers related to PBR systems have increasingly received significant attention in research. There are many target detection methods for PBR system in the literature. This thesis assumes a system scenario based on stereo FM signals as transmitters of opportunity. Ambiguity function (AF) is a function that determines the locations of targets in range-Doppler map turns out to be noisy in practice. This can cause a problem with low SNR-valued targets because they cannot be visible. To solve this problem, compressive sensing (CS) and projection onto the epigraph set of the ℓ_1 ball (PES-ℓ_1) are used to denoise the range-Doppler map. Some CS methods are applied to the system scenario, which are Basis Pursuit (BP), Orthogonal Matching Pursuit (OMP), Compressed Sampling Matching Pursuit (CoSaMP), Iterative Hard Thresholding (IHT). In addition, AF is generally used to determine the similarities between two signals. Therefore, different correlation methods can be also used to compare the surveillance and time delayed frequency shifted replica of the reference signal. Maximal Information Coefficient (MIC), Pearson correlation coefficient, Spearman's rank correlation coefficient are used for the target detection. This thesis proposes a least squares (LS) based method which outperforms other correlation algorithms in terms of PSNR and SNR. Two LS coefficients are obtained from the real and imaginary parts of predicting the surveillance signal using the modulated reference signal. Norm of LS coefficients exhibit a peak at target locations. The proposed method detects close targets better than the ordinary AF method and decreases the number of sidelobes on multiple FM channels based the PBR system.

Keywords: Passive Bistatic Radar, Stereo FM, Ambiguity Function, Recursive Least Squares (RLS), Least Mean Squares (LMS), Constant False Alarm Rate (CFAR), Compressive Sensing, Denoising, Correlation Methods.

ÖZET

PASİF BİSTATİK RADAR SİSTEMLERİ ÜZERİNDE HEDEF TESPİTİ VE GÖRÜNTÜLENMESİ

Rasim Akın Sevimli
Elektrik ve Elektronik Mühendisliği Bölümü, Yüksek Lisans
Tez Yöneticisi: Prof. Dr. A. Enis Çetin
Eylül, 2014

Pasif Bistatik Radar (PBR) sistemleri son yıllarda birçok araştırma topluluklarında ve ülkede çok popüler olmuştur. PBR sistemleri ile ilgili makaleler, araştırmada giderek büyük bir ilgi toplamaktadır. Literatürde, PBR sistemleri için bir çok hedef tespit metodları bulunmaktadır. Bu tez, ticari kaynaklı vericilerden gelen sinyaller olan çift kanallı FM sinyali tabanlı bir sistem senaryosunu varsaymaktadır. Belirsizlik fonksiyonu (BF), uzaklık-Doppler haritasında hedeflerin yerlerini saptayan bir fonksiyondur ki pratik olarak gürültülü bir şekilde gelmektedir. Bu, düşük SNR değerli hedefler için probleme yol açmaktadır çünkü görünemeyebilirler. Bu problemi çözmek için, sıkıştırılmış algılama (SA) ve dışbukey maliyet fonksiyonunun epigraf kümesine dikey iz düşümü (PES-ℓ_1) algoritmaları uzaklık-Doppler haritasını gürültüden arındırmak için kullanılmıştır. Bazı SA metodları sistem senaryosuna uygulanmıstır ki bunlar Taban Kovalama (BP), Ortogonal Uyum Kovalama (OMP), Sıkıştırılmış Örneklemeli Uyum Kovalama (CoSaMP), Döngülü Sert Eşikleme (IHT)'dir. Ek olarak, BF genel olarak iki sinyal arasındaki benzerlikleri bulmak için kullanılır. Bu yüzden, farklı ilinti metodları da tarama sinyali ile kaynak sinyalinin zaman geciktirmeli frekans kaydırmalı türünü karşılaştırmak için kullanılmıştır. Maksimal Bilgi Katsayıları (MIC), Pearson ilinti kaysayıları, Spearman'ın düzey ilinti katsayıları, hedef tespiti için kullanılmıştır. Bu tez, diğer ilinti algoritmalarına göre PSNR ve SNR bakımından iyi sonuç veren en küçük kareler (LS) tabanlı bir metod önermektedir. İki en küçük karelerin katsayıları, kaynak sinyaliyle kiplenen tarama sinyalinin tahmininin gerçel ve sanal kısımları tarafından elde edilir. En küçük kareler kaysayılarının normu hedef olan yerlerde bir tepe oluşturmaktadır. Önerilen metod, yakın hedefleri tipik BF'den daha iyi tespit etmektedir ve çoklu FM kanalları tabanlı PBR sistemleri üzerinde yan kulakların sayısını düşürmüştür.

Anahtar sözcükler: Pasif Bistatik Radar, Çift Kanallı FM, Belirsizlik Fonksiyonu, Özyinelemeli En Küçük Kareler (RLS), En Küçük Ortalama-Kare (LMS), Sıkıştırılmış Algılama, Gürültüden Arındırma, İlinti Metodları.

Acknowledgement

I would like to express my gratitude to Prof. Dr. A. Enis Cetin for his supervision, suggestions and encouragement throughout the development of his thesis.

Furthermore, I would like to offer my special thanks to Prof. Dr. Orhan Arıkan and Prof. Dr. Uğur Güdükbay for accepting to read and review this thesis.

I would also like to express my appreciation to following:

- TÜBİTAK for supporting this work under Grant Number 113A010.
- Havelsan-EHSİM for providing software and their support during this thesis.
- Dr. Kıvanç Köse, Osman Günay, Y. Hakan Habiboğlu, Ahmet Yazar, Dr. İbrahim Onaran, Mohammad Tofighi for giving me valuable advice on many topics.
- To members of Signal Processing Group for collaboration and constructive friendship: Serdar Çakır, Onur Yorulmaz, İhsan İnaç, Alican Bozkurt, M. Tunç Arslan, Cem E. Akbaş, Oğuzhan Oğuz, Sebastian Hetenkofer.
- My closest friends: Abdullah Gümüş, Ömer K. Ahıskalı, Şeyma Canik, Polat Göktaş, Saeed Ahmed, Serkan Sarıtaş, A. Başar Akbay, Oğuzhan Teke, Mehmet Dedeoğlu, M. Ömer Sayın.

Of course, I would like to thank to my family for supporting me for all of my life. They have always excellent contributions on everything I have done.

Contents

List of Figures

List of Tables

Chapter 1

Introduction

Bistatic Radar (BR) systems have been studied and developed since the development of earliest radars [3]. Before the pulsed waveforms and transmitter/receiver technology, the first radars had been all bistatic. BR systems were used by many countries in air defense networks during the early 1930s. For example, the British, the French, the Soviet Union and the Japanese used BP systems at different platforms. The Germans used them in World War II. After invention of pulsed radars, bistatic radars became very expensive and less efficient when compared to other types.

In recent years, Passive Bistatic Radar (PBR) became popular interest due to the low-cost computing power and digital receiver technology. PBR systems have been analyzed since the mid 1980s. Because of increasing digitalization of broadcast, they are heavily under analysis today. Especially, they have been using TV and FM signals, but many other commercial broadcasts like DVB, DAB are under investigation to deploy in PBR systems. PBR has also received much interest in the academic world as well as military communities [4]. In Figure 1.1, a system block diagram of a PBR system is shown.

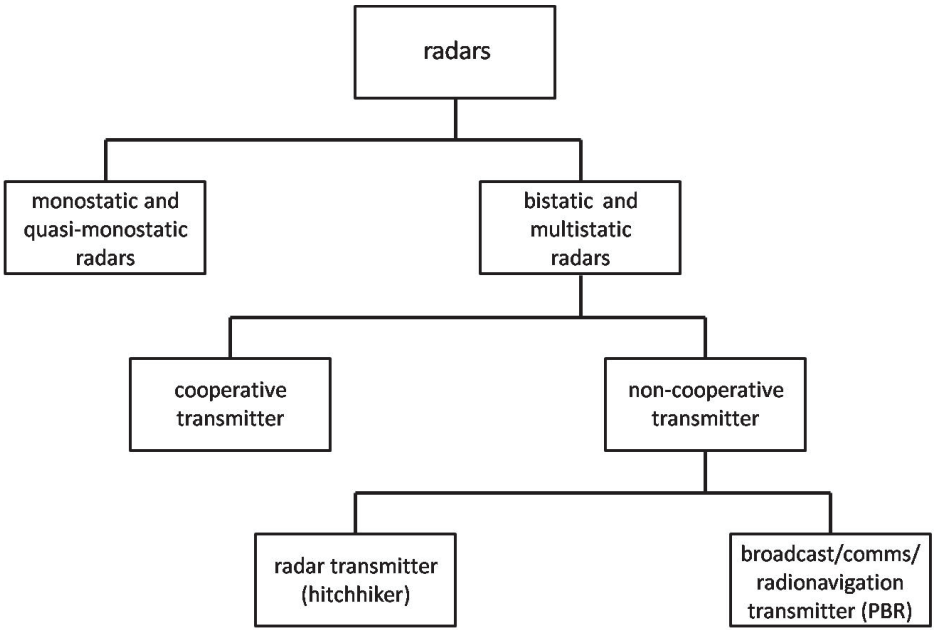

Figure 1.1: A schema for radar and passive bistatic radar systems. Courtesy of "Chris J. Baker" [1].

Bistatic radars can work either with their own transmitters, which are only designed for bistatic operation or with *transmitters of opportunity*, which are designed for other purposes especially for broadcasting purposes. When it is from a monostatic radar, the bistatic radar is often called a *hitchhiker* [5]. If it is provided from non-radar transmission, such as broadcast, communications or radionavigation signal, the bistatic radar has been called many things including *passive radar* [6], *passive coherent location* [7], *parasitic radar* [8] and *piggy-back radar* [9]. In this thesis, we will study *Passive Bistatic Radar* (PBR) systems. In military applications, transmitters of opportunity can be specified as *cooperative* and *non-cooperative*. Cooperative transmitters are friendly transmitters and non-cooperative transmitters correspond to hostile transmitters or ordinary broadcasting systems. Most PBR systems uses non-cooperative transmitters.

PBR is a kind of radar in which the transmitter and the receiver are at separate locations [10]. While monostatic radar systems have transmitters and receivers

at the same location, passive bistatic radar systems have transmitter and receiver antennas at separate locations. Basically, the idea behind this radar type is that it does not illuminate the target itself, but uses illuminations by transmitters of opportunity, which are generally commercial broadcasts [11].

Advantages and disadvantages of PBR systems are listed below:

- Advantages:
  - Due to being passive, they are potentially undetectable.
  - They may be lower cost compared to ordinary radars because they do not need a dedicated transmitter.
  - They can update the target positions very fast.
  - They have the potential ability to detect stealth targets.
  - They do not need any specific frequency allocations.
  - Possible enhanced Radar Cross Section (RCS) of the target due to geometrical effects.
- Disadvantages:
  - More complex geometry.
  - Lack of control over transmitter.
  - The technology is relatively immature.

Stealth technology starts to have a big interest in military aircrafts. PBR systems allow users to detect and track the target piloted and unpiloted stealth systems. There are many ongoing researches in that area [12]. Even though the target is a stealth aircraft, the characteristics of omnipresent radio signals enable us the detection of them. Unlike conventional radar emits the radiation, PBR systems do not emit radiation. Instead, they analyze radiation reflection from the emitters.

1.1 Thesis Outline and Contribution

This thesis starts with giving a background for Passive Bistatic Radar systems in introduction part. Simulation a system scenario according to given target and clutter positions and Doppler frequencies is provided with stereo FM signals and also the detection process of a target by Ambiguity Function (AF) is explained in Chapter 2. Adaptive algorithms for canceling the clutters and CFAR algorithm are presented. Afterwards, Compressive Sensing (CS) and PES-ℓ_1 method are described and applied to the PBR systems to denoise the 2D range-Doppler map in Chapter 3. All methods are compared at the end of the chapter. Finally, Chapter 4 discusses whether comparison of correlation between surveillance signal and time delayed frequency shifted replica of reference signal can be used instead of AF. For this purpose, least squares based new method called Cross-term free Least Squares (CLS) is proposed in this thesis. It is observed that it is possible to detect close targets when multichannel based PBR system is used. Simulations and performance comparisons are also presented.

Chapter 2

Properties of Passive Bistatic Radar

In this chapter, we review some properties of passive radar systems. There can be many targets of which we want to detect both positions and frequencies (velocities) in the environment. The first property of the PBR system is the *bistatic geometry* that has many operating characteristics, such as bistatic range, Doppler frequency, radar cross section (RCS) and range resolution. Therefore, one needs to understand the bistatic geometry before handling the PBR system. On the other hand, the *bistatic radar equation* should be known to predict the performance of the PBR system. Since our aim is the detection and imaging of the PBR system based on some signal processing algorithms, it is important to create a *system scenario*. For this reason, we need to decide upon an illumination source type and simulate it. In this thesis, stereo FM signals generated by the MATLAB computer program are used as transmitters of opportunity. After this step, surveillance and receiver antennas are defined instead of a receiver antenna, which provides us surveillance and reference signals. As we consider these surveillance and reference antennas, targets, clutters located at the Cartesian coordinate system we can create a PBR system scenario, whose specifications depend on users. Therefore, any user can specify the number of targets ands clutters that will be used in this system scenario.

2.1 Bistatic Geometry

As the terma 'bistatic' implies, the bistatic geometry is based on a pair of transmitter and receiver with different locations. Together with a target and its velocity V, this is illustrated in Figure 2.1. All additional parameters can be found in Table 2.1.

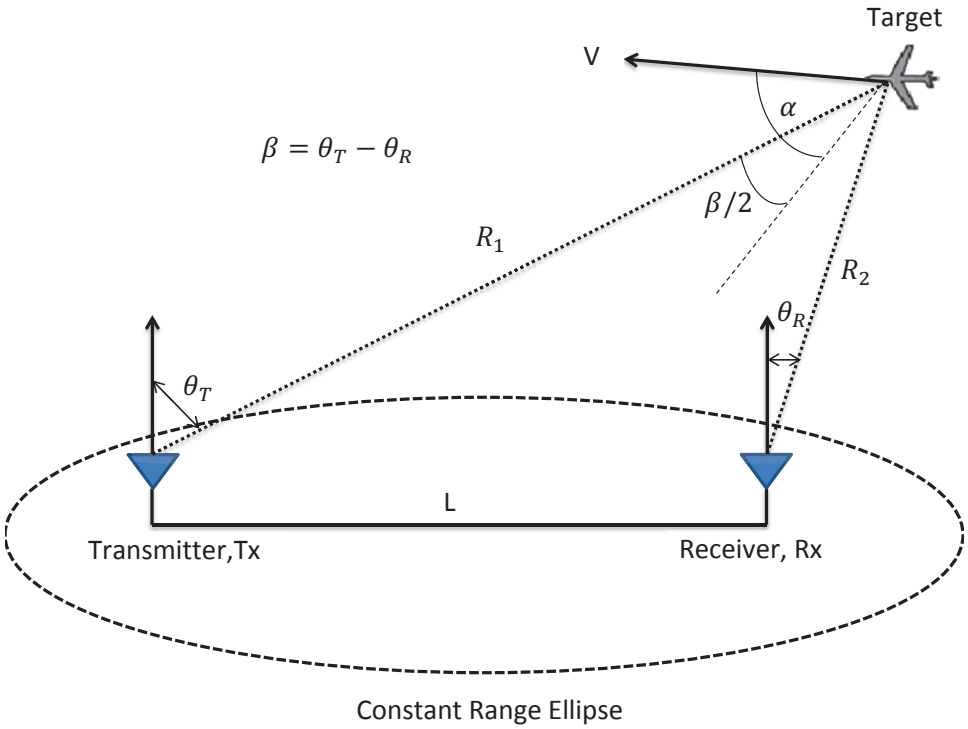

Figure 2.1: Illustration of bistatic radar geometry. Bistatic geometry show the parameters defining the bistatic radar operation in the constant range ellipse containing the transmitter (Tx), receiver (Rx) and the target with velocity V. The bistatic triangle lies in the constant range ellipse plane. The distance L between transmitter and receiver is called baseline range. The angles, θ_T and θ_R are transmitter and receiver looking angles, respectively. The target's velocity vector proejcted onto the the plane has magnitude V and aspect angle α. Bistatic angle is $\beta = \theta_T - \theta_R$. Courtesy of "M. Jackson" [2].

The bistatic geometry has some important basic measurements, such as

Table 2.1: Parameters used in bistatic geometry.

Symbol	**Meaning**
β	Bistatic angle
α	Velocity aspect angle
R_1	Target-receiver distance
R_2	Target-transmitter distance
L	Baseline range
V	Target velocity
θ_R	Receiver looking angle
θ_T	Transmitter looking angle

bistatic range and *Doppler frequency*. *Bistatic range* can be defined as a measurement of target positions in the constant range ellipse. This ellipse shown in Figure 2.1 is centered on a transmitter and a receiver. Let R_1/R_2 be the distance between the target and transmitter/receiver. The distance is denoted by L. Hence we can calculate the target location at the range ellipse as $R_1 + R_2 - L$. Since the positions of the transmitter and receiver antennas are specified by users, L, R_1 and R_2 can be calculated as follows:

$$\begin{aligned} L &= \sqrt{|Tx_x - Rx_x|^2 + |Tx_y - Rx_y|^2} \\ R_1 &= \sqrt{|Tx_x - Ta_x|^2 + |Tx_y - Ta_y|^2} \\ R_2 &= \sqrt{|Rx_x - Ta_x|^2 + |Rx_y - Ta_y|^2}, \end{aligned} \tag{2.1}$$

where Tx_x and Tx_y are transmitter antenna positions, Rx_x and Rx_y are receiver antenna positions, Ta_x and Ta_y are target positions respectively in Cartesian coordinate system.

Another measurement by looking at this geometry is *Doppler frequency*, which measures the velocity of targets. The Doppler frequency of the reflected by the target is calculated as follows:

$$f_B = \frac{1}{\lambda}\left[\frac{d}{dt}(R_1 + R_2)\right], \tag{2.2}$$

where λ is the wavelength of the signal. This equation shows that Doppler frequency is proportional to the rate of change of the bistatic range. Then, derivatives of R_1 and R_2, $\frac{dR_1}{dt}$ and $\frac{dR_2}{dt}$, can be found by projecting the velocity vector onto R_1 and R_2, so we can get the Doppler frequency f_B as follows:

$$f_B = \frac{2V}{\lambda} cos(\alpha) cos(\beta/2). \tag{2.3}$$

Using Equation 2.3, we can define the term v_B as follows:

$$v_B = V cos(\alpha) cos(\beta/2)), \tag{2.4}$$

which is called the projected target velocity. Finally, Doppler frequency can be represented by:

$$f_B = \frac{2v_B}{\lambda}. \tag{2.5}$$

In PBR systems, there is another issue for the bistatic geometry, which is called *Radar Cross Section* (RCS). RCS is a function of target size, shape, material and some kind of its dynamic. Furthermore, we can say that the target detection and location are dependent on it [13]. This parameter also takes part in the passive radar equation as discussed in the next section and it is proportional to the received power. RCS can be regarded as a property of the target reflectivity. For example, as a stealth aircraft gives a low RCS because of smooth surfaces and directing the signal to different directions than the source. As opposed to this, passenger planes a high RCS because of bare material etc. Bistatic radar cross section equation, σ_B is defined as follows:

$$\sigma_b = \frac{4\pi A^2}{\lambda^2}, \tag{2.6}$$

where A is the physical cross-sectional area. The angular width of the scattered signal horizontal or vertical plane is defined as follows:

$$\theta_b = \frac{\lambda}{d}, \tag{2.7}$$

where d is the target linear dimension.

Another important parameter in PBR systems is the *range resolution*. A target resolution of the bistatic radar is its capability to separate two targets which are very close each other in a range. Radar range resolution, $\triangle r$ can be approximately found as follows:

$$\triangle r = c/2B, \tag{2.8}$$

where B is the bandwidth of the signal. This equation shows that if we increase the bandwidth of the reference signal, we may have better range resolution. As we know from Appendix A, a typical FM radio occupies a bandwidth of about $B = 100$ kHz, so radar range resolution will be equal to $\triangle r = 1.5$ km in our system.

2.2 Bistatic Radar Equation

In this section, the bistatic radar equation is presented and shown as follows:

$$P_r = P_t \cdot \frac{G_t}{4\pi R_1^2} \cdot \sigma_b \cdot \frac{G_r}{4\pi R_2^2} \cdot \frac{\lambda^2}{4\pi}, \tag{2.9}$$

where P_r is the received signal power, P_t is the transmit power, G_t is the transmit antenna gain, G_r is the receive antenna gain, R_1 is the transmitter-target distance, R_2 is the target-receiver distance, λ is the radar wavelength.

The bistatic radar equation can be used to predict the performance of the PBR systems. Each parameter is important to understand how to affect the performance. In some cases, receivers have inefficient antennas and poor noise figures. These losses and inefficiencies can be overcome by using high transmit power. If you increase transmit power, you can get more receive power. To increase the receiver power, the range between target-receiver and transmitter-target may be reduced or transmitter and receiver antenna gains may be enlarged.

2.3 System Scenario

In PBR systems, there are two essential things to create a system scenario. One of them is the reference signal (direct signal) and the another one is the surveillance signal. In practice these signals are obtained from reference and surveillance antennas [6]. Reference and surveillance antennas are represented more general and shown as a receiver antenna in Figure 2.1. However, they are assumed as separate antennas for the purpose of the analysis in this thesis. In addition, there can be some unwanted echoes called as clutters/multipaths in the system environment. These echoes occur when the transmitting signal is reflected by objects or obstacles and reach the surveillance antenna after two or more paths. A lot of examples can be given for these objects, such as houses, cars, ground, etc. This system environment is illustrated in Figure 2.2.

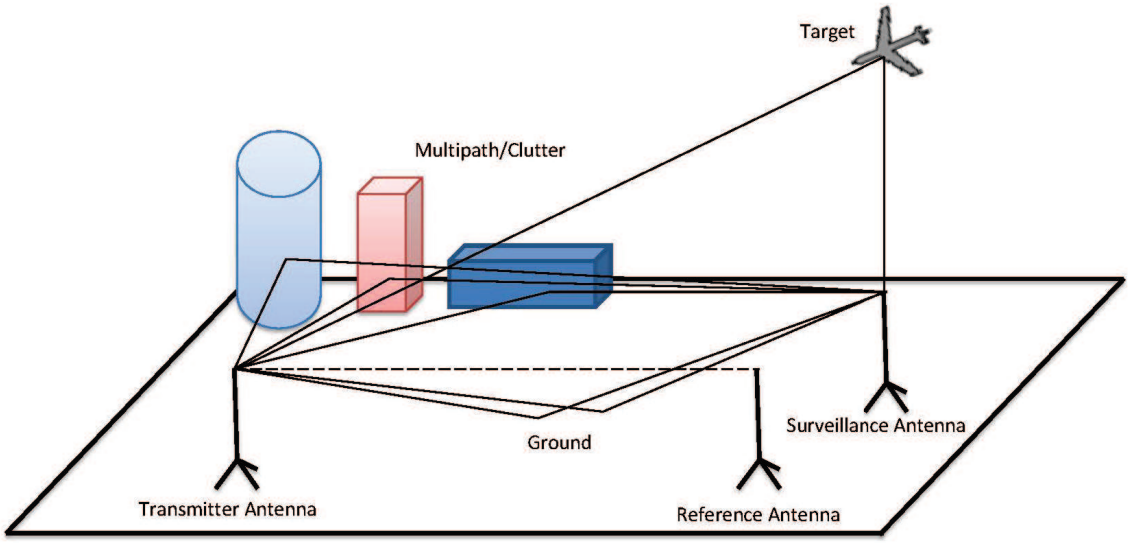

Figure 2.2: System environment with a surveillance and a reference antenna.

Based on this environment, the reference signal can be modeled as follows:

$$s_{ref} = A_{ref}s(t) + n_{ref}(t), \tag{2.10}$$

where A_{ref} is the complex amplitude, n_{ref} is the noise and $s(t)$ is the transmitted complex baseband signal. Echoes in the reference antenna are neglected in this thesis. The complex envelope of the modulated signal has already been generated in Appendix A. After that, the surveillance signal with the effect of multipaths and clutters can be modeled by using the complex baseband signal $s(t)$ and it is presented as follows:

$$s_{surv} = \sum_{m=1}^{N_T} G_m s(t - \tau_m) e^{j2\pi f_{dm} t} + n_{surv}(t), \tag{2.11}$$

where G_m is the complex amplitude, τ_m is the time delay, f_{dm} is the Doppler frequency. Due to the bistatic geometry described in Section 2.1, the bistatic range is calculated by computing $\triangle R_{bis} = R_1 + R_2 - L$, so the time delay can be calculated as follows:

$$\tau_m = \frac{R_1 + R_2 - L}{c}, \tag{2.12}$$

where $c = 3 \times 10^8$ is the speed of light. If we assume to have the information about system scenario specifications which consist of gain, time delay, Doppler frequencies of each target and clutters, the position of the transmitter, receiver antenna and the clutters, it is possible to generate a table with bistatic ranges in km, Doppler frequencies in Hz and gains in dB of targets. There are a transmitter, a receiver, 6 targets and 6 clutters whose positions are created randomly in a coordinate system. Bistatic ranges, Doppler frequencies and gains of these 6 targets are shown in Table 2.2. It is important to know that the Doppler frequency for clutters are supposed to be "0" because they do not move. The surveillance signal created by 6 targets and 6 clutters is illustrated in Figure 2.3.

Table 2.2: System specifications for six targets.

	Target 1	Target 2	Target 3	Target 4	Target 5	Target 6
Bistatic Range (Km)	40,65	51,63	14,14	4,14	23,03	60
Doppler Frequency (Hz)	150	-250	50	300	-150	-300
Gain (dB)	4,1	-3,8	-20,8	-21,1	-21,6	-22,1

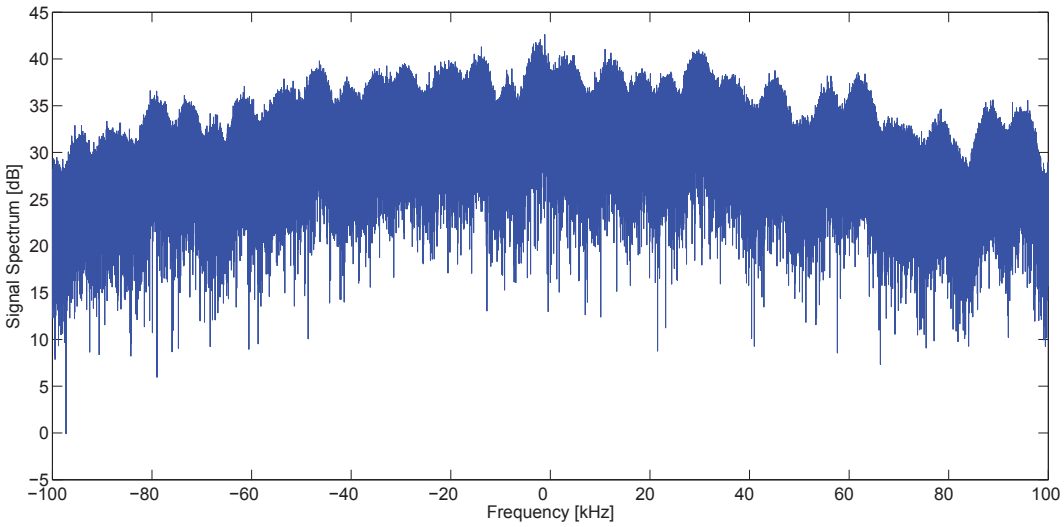

Figure 2.3: The surveillance signal according to the system scenario.

2.4 Ambiguity Function

In this section, the detection process of targets and clutters given in a system scenario is presented. The target and clutter detection in passive bistatic radar is based on the evaluation of the range-Doppler cross-section function called Ambiguity Function (AF). This function can be implemented with the Fast Fourier Transform (FFT) operation. Surveillance and reference signals generated at previous sections are applied to plot the range-Doppler map. All calculations are performed in MATLAB R2013b (8.2.0.701) 64-bit computer program.

Whichever waveform is used, it is an important requirement to extract the best information about the target from the received signal as possible [14]. Surveillance and reference signals are applied to the matched filtering [15]. Then, the output of the matched filter at time T is given by

$$\xi(T) = \int_0^T s_{surv}(t) s_{ref}^*(t-\tau) e^{-j2\pi f_{dm} t}. \tag{2.13}$$

Instead of Eq. 2.13, the output of the matched filter can be generalized and expressed as a function of τ and f_{dm}, which corresponds to the range and Doppler frequency of the target. In addition, the matched filter is often implemented on digital computers in practice, so $s_{surv}(t)$ and $s_{ref}(t)$ signals are converted to discrete signals $s_{surv}[n]$ and $s_{ref}[n]$, respectively. In practice, AF is calculated in terms of *range (time) bins* and *Doppler bins*. Range bins are obtained by $l = \tau.f_s$, which explains how much the reference signal will be delayed. Furthermore, $p = f_{dm}.NT_s$ is the Doppler bin representing the Doppler frequency of the backscattered echo from the target. The target velocity can be calculated using $v = \lambda.f_{dm}$. Lastly, the discrete implementation of the 2D ambiguity function is given as follows:

$$\xi[l,p] = \sum_{i=0}^{N-1} s_{surv}[i] s^*_{sref}[i-l] e^{-\frac{j2\pi ip}{N}}, \tag{2.14}$$

where N is the number of samples, l is the bistatic range bin and p is the Doppler bin. This equation is demonstrated in Figure 2.4 according to the system scenario shown in Table 2.2. If we recall $b_l[i] = s_{surv}[i] s^*_{ref}[i-l]$, AF can be implemented by computing the FFT of $b_l[i]$. AF can be rearranged in the following equation:

$$\begin{gathered} \xi[l,p] = \sum_{i=0}^{N-1} b_l[i] e^{-\frac{j2\pi ip}{N}}, \\ l = 0, 1, ..., L, \quad p = 0, 1, ..., N-1. \end{gathered} \tag{2.15}$$

In this thesis , the sampling frequency, f_s and the integration time are 2×10^5 Hz and 1 sec., respectively, so the length of surveillance and reference signals is 2×10^5. This discrete-time signal is decimated in time and the length of signals is reduced to $N = 4096$. After this point, the Doppler frequency axis is focused between -500 and 500 Hz to show targets clearly. The values for L and p are chosen as $L = 150$ and $p = -500, ..., 500$. The reason for choosing $L = 150$ is that, PBR systems use stereo FM signals to detect and track targets in the range of approximately 250 km [16]. We know that the bistatic range is equal to $\triangle R_{bis} = lT_sc$. Since the bistatic range is 250 km, the maximum range bin should be approximately $\frac{250}{T_sc} \cong 150$ km. In addition, gains of targets are normalized

between 0 and 1. We have used 6 clutters, so it is likely to see clutters at the zero frequency with different bistatic ranges. In Section 2.5, different adaptive filter algorithms are applied to cancel the clutter effect.

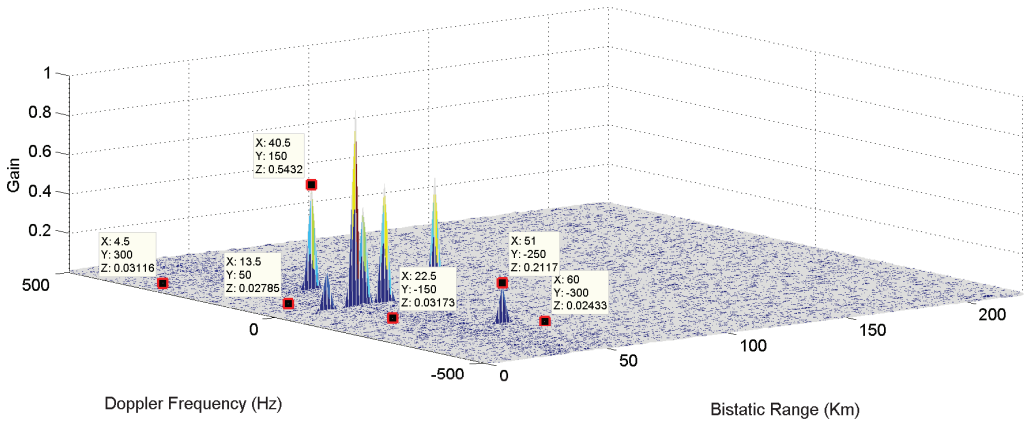

(a)

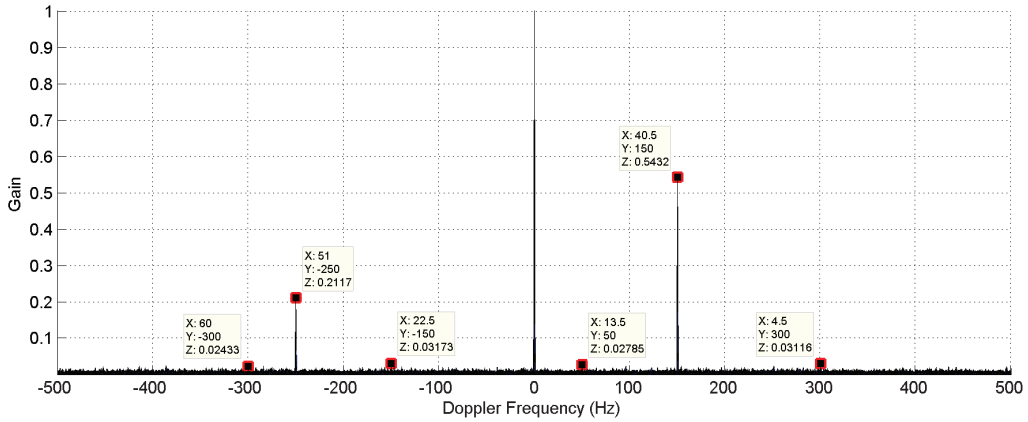

(b)

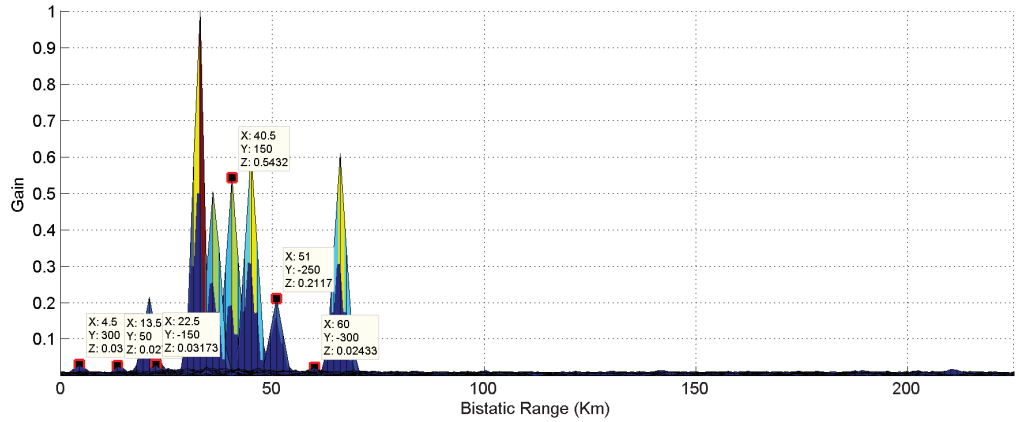

(c)

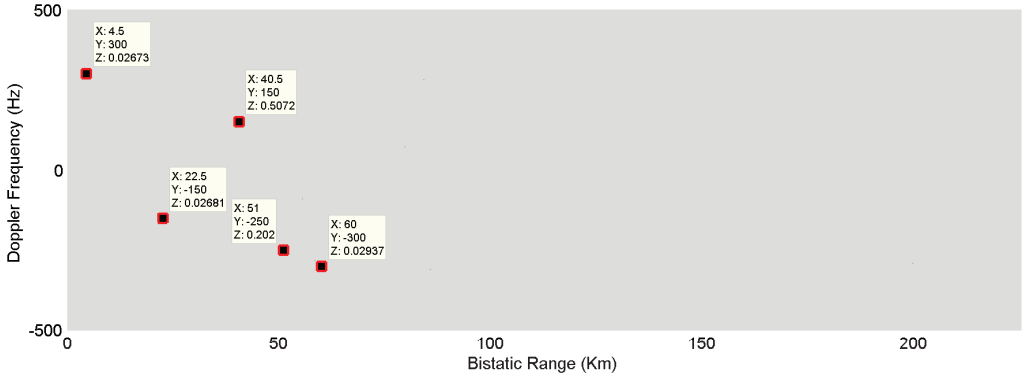

(d)

Figure 2.4: Plotting the 6 target positions according to system scenario: (a) 3D plot; (b) Doppler frequency plot; (c) Bistatic range plot; (d) view from the top.

2.5 Clutter Cancellation and Detection of a Target with CFAR algorihtm

In any bistatic radar system the first step is the clutter removal. As can be seen in Section 2.4, the range-Doppler map can have many clutter/multipath echoes at zero Doppler frequency. This is a really important problem because it is sometimes impossible to see if there are targets near to zero Doppler frequency or not. This means that the clutter can mask potential targets. Therefore, we prefer to apply adaptive filters, such as least mean squares (LMS) and recursive least squares (RLS) to cancel the clutter in this thesis. Basically, the system

flow chart of the bistatic radar target detection system is shown in Figure 2.5. First, adaptive filters are applied to reference and surveillance signals and then the range-Doppler map is computed using the DFT of the ambiguity function.

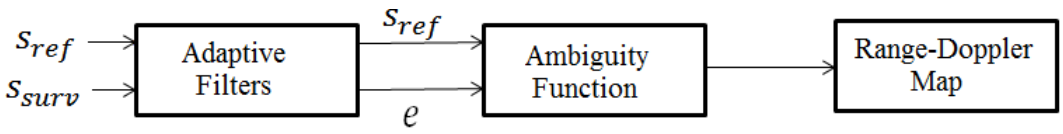

Figure 2.5: System flow chart.

In addition, constant false alarm rate (CFAR) algorithm is applied to our system. Normally, we may have certain noise level in range-Doppler map, so this algorithm tries to find out the noise level and low SNR-valued targets more clearly [17].

2.5.1 Adaptive Filters

Adaptive filters are used in many signal processing applications [18]. One of the application is to cancel the clutter effect on passive bistatic radar systems. As known from the previous section, the surveillance signal is obtained by time-delayed frequency shifted replica of the reference signal. Ambiguity function most probably comes out with many clutters/multipaths peaks at zero Doppler frequencies as shown in Figure 2.4. These kind of peaks may mask the peaks of actual target. This is an important problem in real life applications. Although there are some techniques mentioned in [19] and [20], we used adaptive filter algorithms, such as least mean square (LMS) and recursive least square (RLS) to remove the clutter. Basically, our main purpose of using adaptive filters in PBR systems is to simulate the reference signal to the surveillance signal so that clutters/multipaths may be canceled at zero-Doppler frequency. For both algorithms, the schematic filter diagram is shown in Figure 2.6. In general, the error signal is to adjust the coefficients of the adaptive filters [21] and calculated as follows:

$$e[n] = s_{surv}[n] - y[n] \tag{2.16}$$

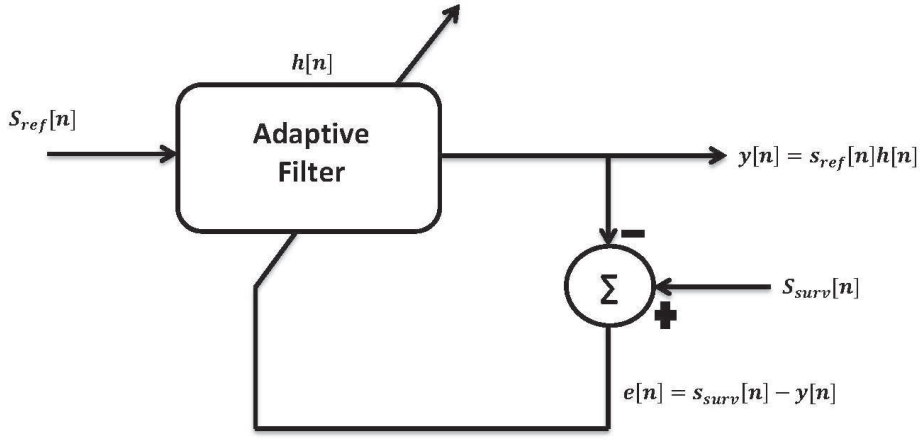

Figure 2.6: General representation of the adaptive filter used in PBR.

In this section, a brief description of the considered adaptive algorithms is presented to cancel clutter/multipath effects. The system scenario is revised by using adaptive filter algorithms and plotted. Lastly, their efficiencies are compared according to convergence time.

2.5.1.1 Least Mean Squares (LMS)

Least mean squares (LMS) algorithm uses a stochastic gradient algorithm in that the filter is adapted based on the error. The idea behind this approach is to minimize the least mean square of adaptive filter output [22]. The error of the filter $e_{lms}[n]$ is given by

$$e_{lms}[n] = s_{surv}[n] - w_{lms}^{H} s_{ref}[n], \tag{2.17}$$

where w_{lms} is the weight vector of the filter at n'th iteration. For this case, the weight vector update equation can be displayed as follows:

$$w_{lms}[n+1] = w_{lms}[n] + \mu e_{lms}^{*}[n] s_{ref}[n], \tag{2.18}$$

where $w_{lms}[n]$ is the current weight value vector, $w_{lms}[n+1]$ is the next weight value vector and μ is the step-size of the algorithm. Since μ affects the rate of convergence and the accuracy of the algorithm, it controls the performance of the algorithm. The step size μ must be a positive number. If μ is large, the convergence speed is fast, but filtering may not be proper. If μ is small, the filter gives slow response, but filtering is proper and gives good results. Additionally, filter order, p is taken as 50 in our simulations. According to these specifications, the error in the filter and time are plotted in Figure 2.7. In this figure, the number of samples and integration time are chosen as 2×10^5 and 1 sec., respectively.

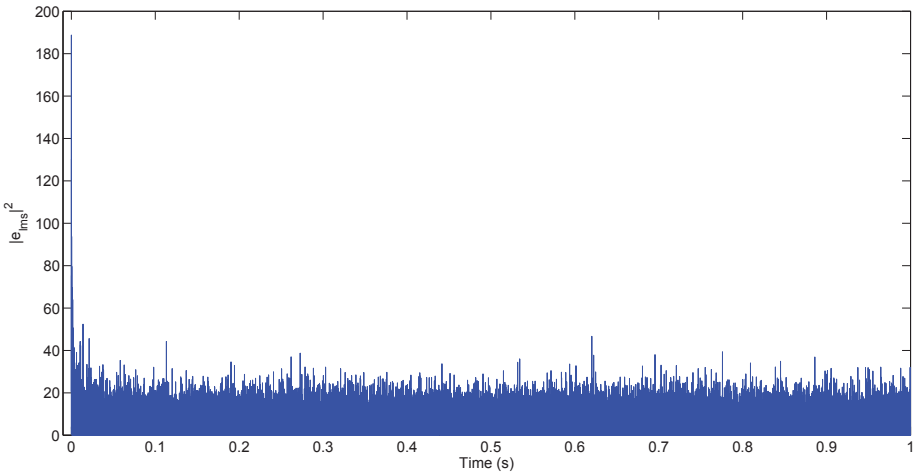

Figure 2.7: Filter output vs time for LMS.

When we investigate the output, LMS adopts the approximate correct output in 800 samples (0.004 sec.). Using the same system scenario, the range-Doppler map is plotted in Figure 2.8. As compared to Figure 2.4(a), clutters are canceled successfully. Running time took about 1.62 sec.

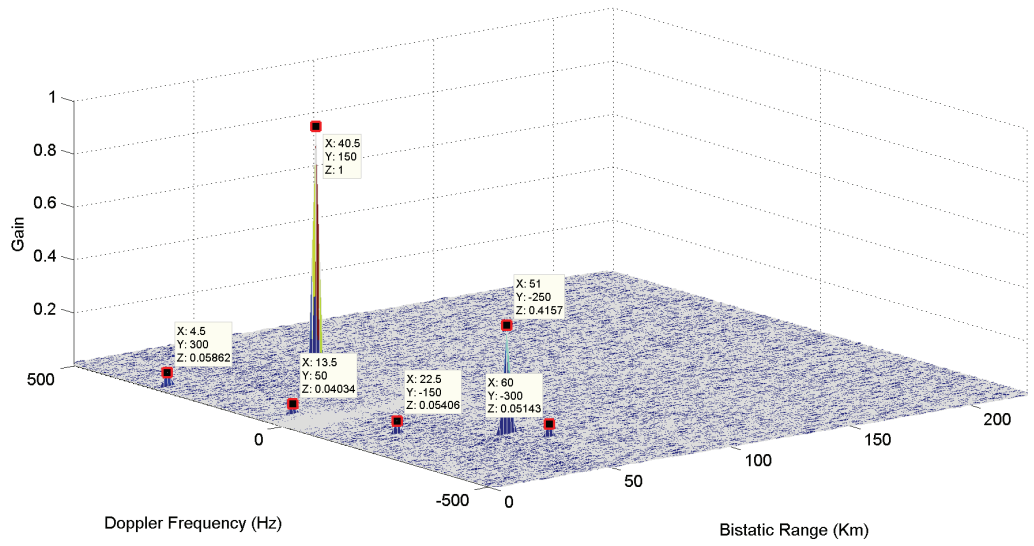

(a)

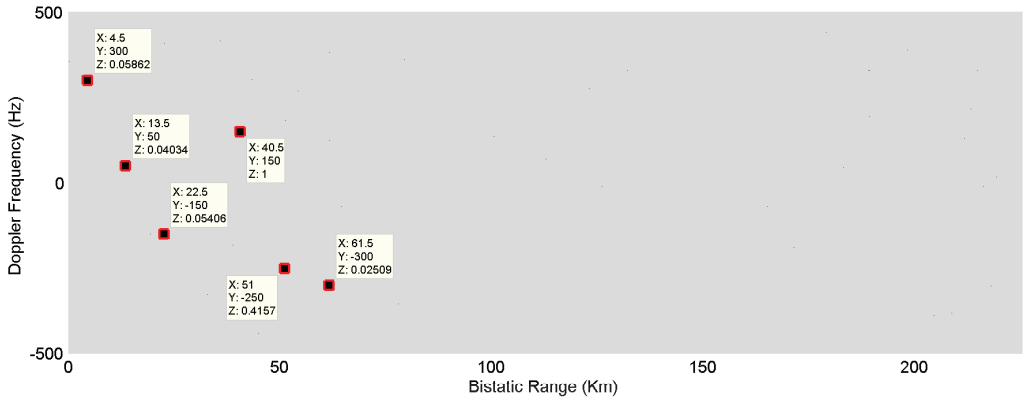

(b)

Figure 2.8: Illustration of range-Doppler map with LMS adaptive filter, $\mu = 0.001$, $p = 50$: (a) 3D plot; (b) view from the top.

2.5.1.2 Recursive Least Squares (RLS)

Recursive Least Squares (RLS) algorithm is a recursive version of the least squares (LS) algorithm. This algorithm recursively finds the filter coefficients that minimize the LS cost function relating to the input signal [23]. Even though RLS is known for its good performance, it has increased computational complexity and

some stability problems. The error of the filter $e_{rls}[n]$ is given by

$$e_{rls}[n] = s_{surv}[n] - w_{rls}^{H} s_{ref}[n], \tag{2.19}$$

where $e_{rls}[n]$ is the weight vector. To update the weight vector, the following expression is used:

$$w_{rls}[n+1] = w_{rls}[n] + k[n]e_{lms}^{*}[n], \tag{2.20}$$

where $k[n]$ is the gain factor and calculated as follows:

$$k[n] = \frac{P[n-1]s_{ref}[n]}{\lambda + s_{ref}^{T}[n]P[n]s_{ref}[n]} \quad \text{such that,}$$
$$P[n+1] = \lambda^{-1}P[n] - k[n]s_{ref}^{T}\lambda^{-1}P[n], \tag{2.21}$$

where λ is the forgetting factor which determines the convergence rate of the algorithm. Filter order and forgetting factor are chosen as $p = 50$ and $\lambda = 0.7$. The relation between the output error of filter and time are shown in Figure 2.9. If we consider the convergence time, RLS adopts the approximate correct output in 100 samples (5×10^{-4} sec.). The range-Doppler map is shown in Figure 2.10 according to the implementation of RLS on system scenario. In this adaptive filter type, running time took 20.75 sec. As a result, LMS adaptive filter is shown that it is much faster than RLS filter, so LMS filter is applied to the 2D range-Doppler map to cancel the clutter for whole calculations in this thesis.

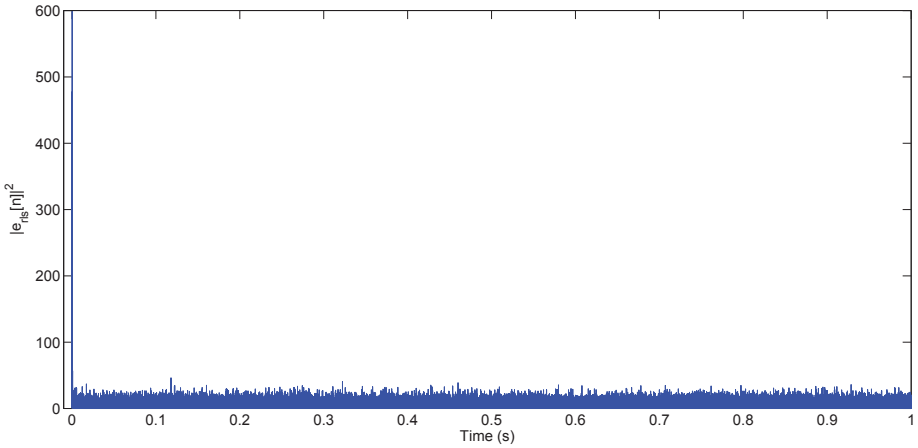

Figure 2.9: Filter output vs time for RLS.

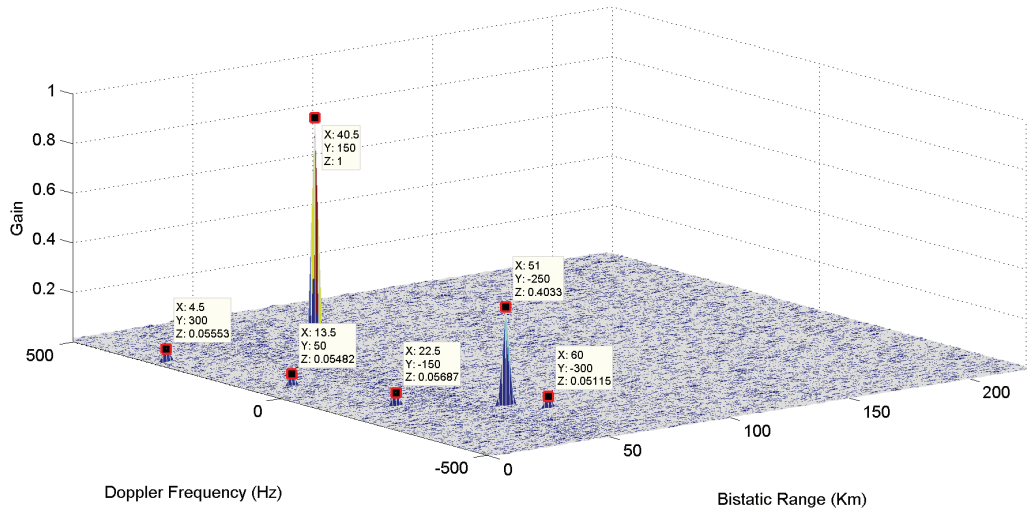

(a)

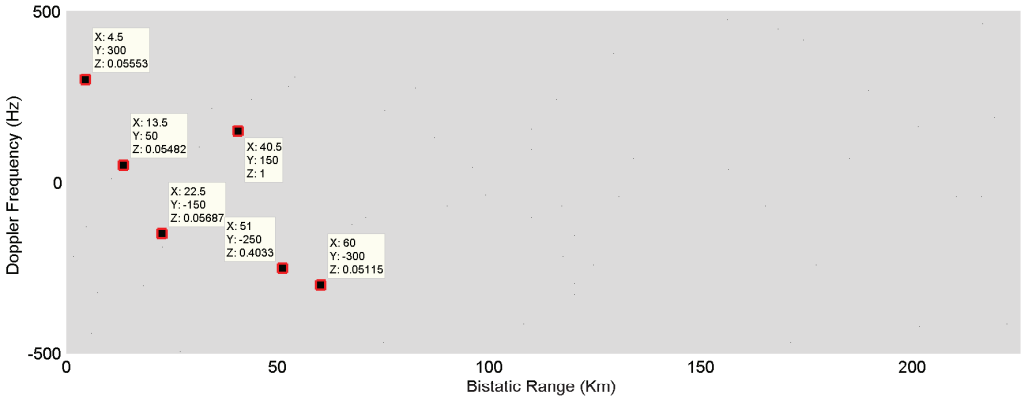

(b)

Figure 2.10: Illustration of range-Doppler map with RLS adaptive filter, $\lambda = 0.7$, $p = 50$ in view of: (a) 3D plot; (b) view from the top.

2.5.2 Constant False Alarm Rate (CFAR)

Constant False Alarm Rate (CFAR) algorithm is an adaptive algorithm used in radar systems to detect targets against noise [24]. The idea behind CFAR algorithm is to determine the adaptive threshold and indicate the target's positions at 0 and 1. If the determined threshold is low, more targets are detected with increased numbers of false alarms. If the threshold is high, some targets may

not be detected with low false alarms. For many cases, this threshold is changed according to probability of false alarm rate (P_{fa}) adaptively [25].

In many CFAR detection applications, the noise floor around the cell under test (CUT) is estimated and then the threshold level is calculated. For this reason, a block of cells is considered and average power level is calculated. However, we need to avoid corruption of the power from the CUT, so some cells *guard cells* are ignored. Average power level is estimated by calculating the remaining cells called as *training cells*. A target can be detected if CUT power is higher than the average power level of training cells. This approach is called as cell-averaging CFAR (CA-CFAR) illustrated in Figure 2.11.

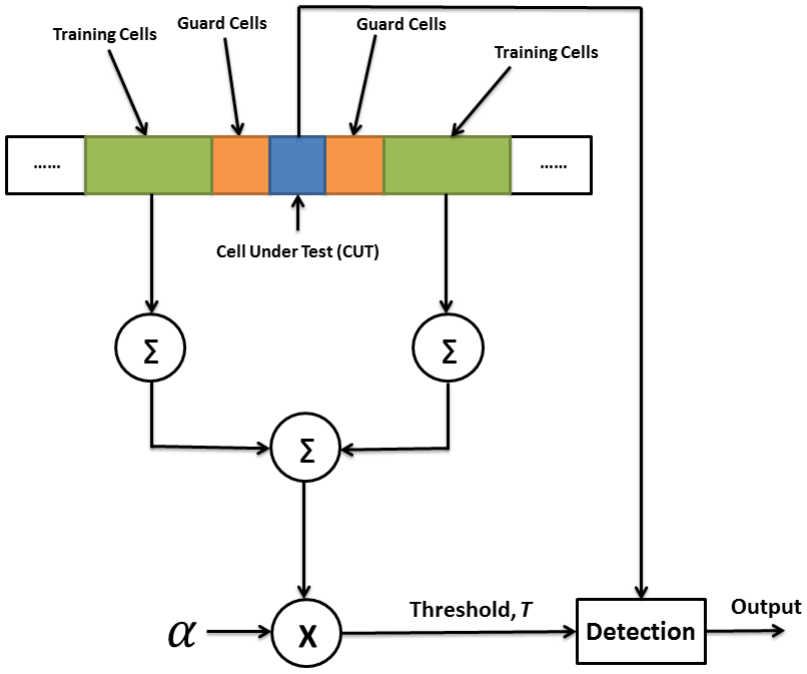

Figure 2.11: The block diagram of the CA-CFAR algorithm.

Suppose that the detection threshold T, is given by

$$T = \alpha P_N, \tag{2.22}$$

where α is the threshold factor and P_N is the estimated noise estimate. P_N can be calculated by averaging the training cells with size N. Another variable, the threshold factor is obtained as follows:

$$\alpha = N(P_{fa}^{-1/N} - 1), \tag{2.23}$$

where P_{fa} is the desired probability of false alarm rate.

After a brief background information, CFAR algorithm is applied and tested using it on PBR systems. Although there are many ways to implement the CFAR algorithm, we used MATLAB keyword, `Phased.CFARDetector` because of speed and efficiency. In our tests, different training and guard cell sizes and P_{fa} values are used. In Figures 2.12, 2.13, 2.14 and 2.15, range-Doppler maps with training cell sizes $10, 100, 10, 20$, guard cell sizes $10, 10, 10, 10$ and P_{fa}=$10^{-4}, 10^{-4}, 10^{-5}, 10^{-7}$ are shown, respectively. Here, red squared points show actual target positions and other points show false alarm positions.

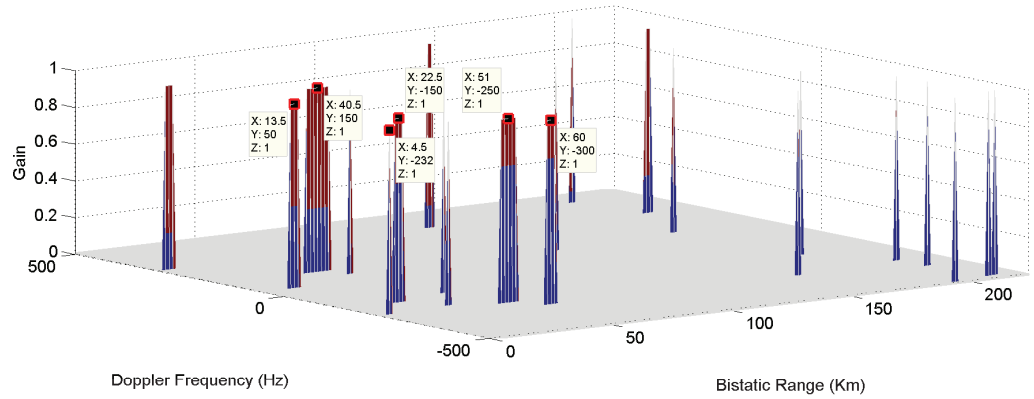

(a)

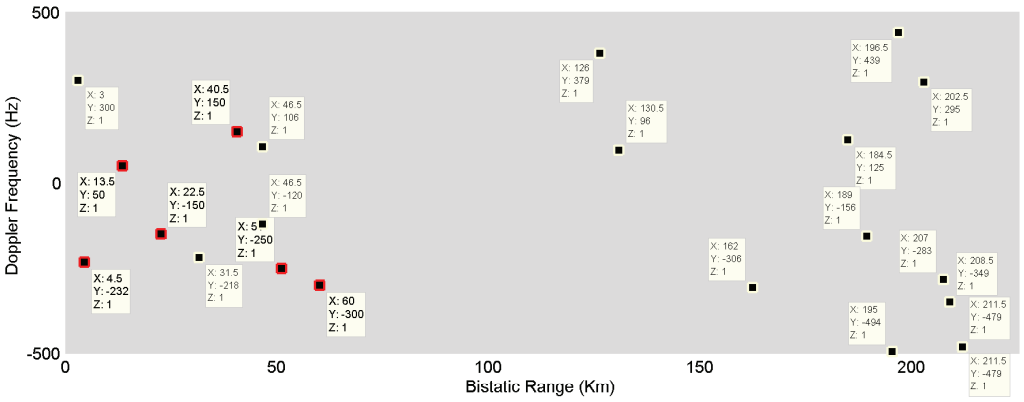

(b)

Figure 2.12: Range-Doppler map for CFAR algorithm with training cell size 10, guard cell size 10, $P_{fa} = 10^{-4}$: (a) 3D plot; (b) view from the top.

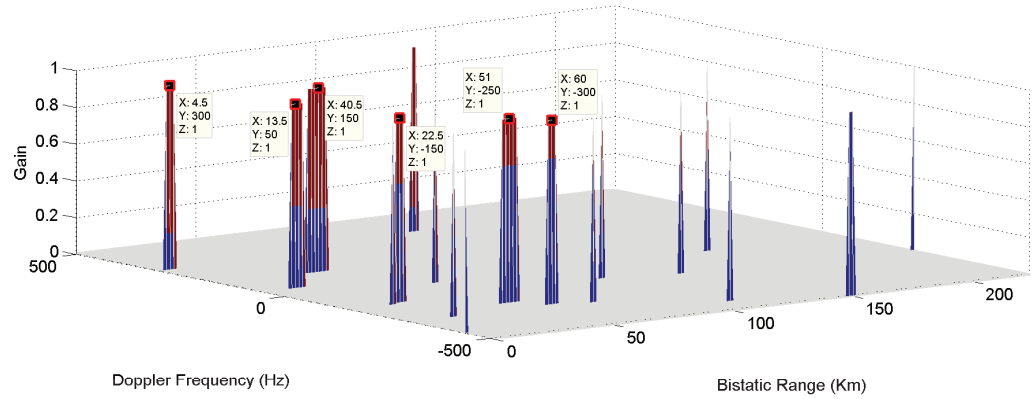

(a)

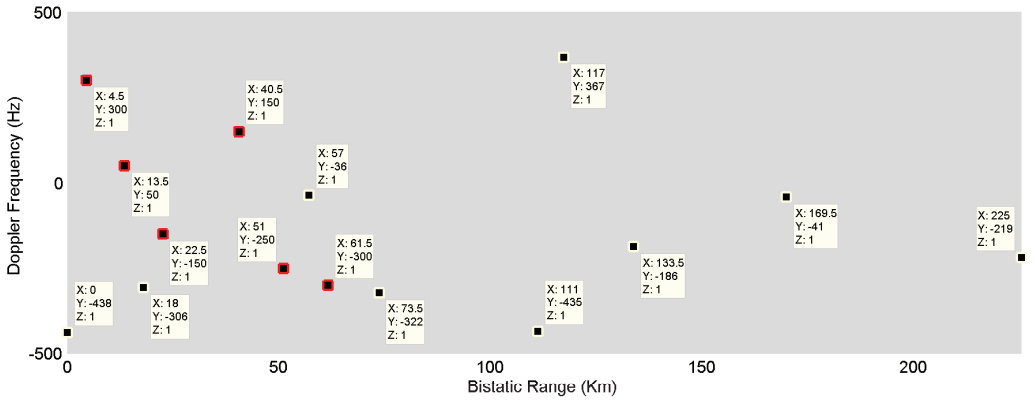

(b)

Figure 2.13: Range-Doppler map for CFAR algorithm with training cell size 100, guard cell size 10, $P_{fa} = 10^{-4}$: (a) 3D plot; (b) view from the top.

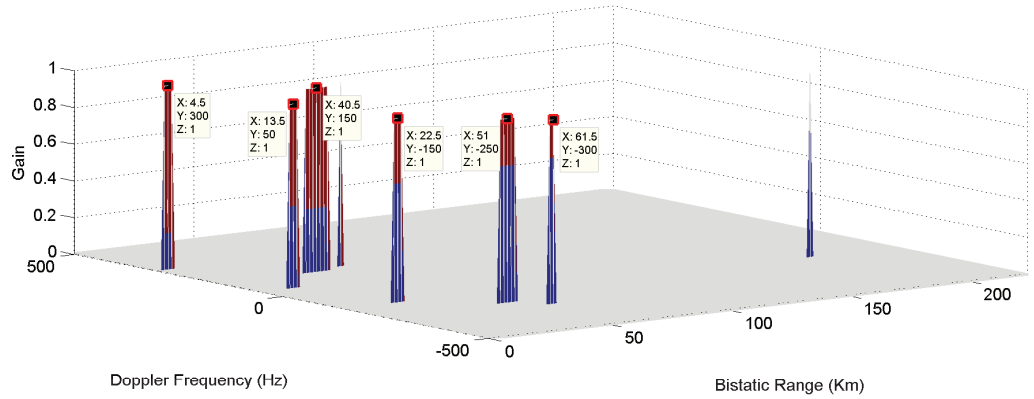

(a)

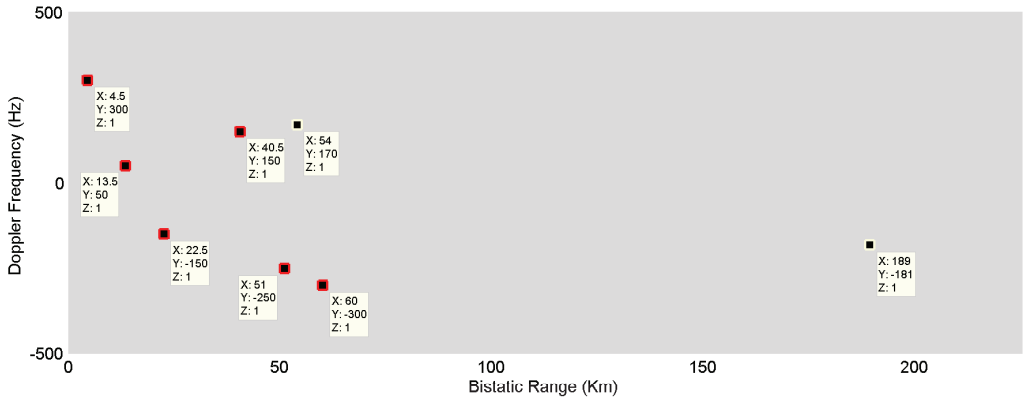

(b)

Figure 2.14: Range-Doppler map for CFAR algorithm with training cell size 10, guard cell size 10, $P_{fa} = 10^{-5}$: (a) 3D plot; (b) view from the top.

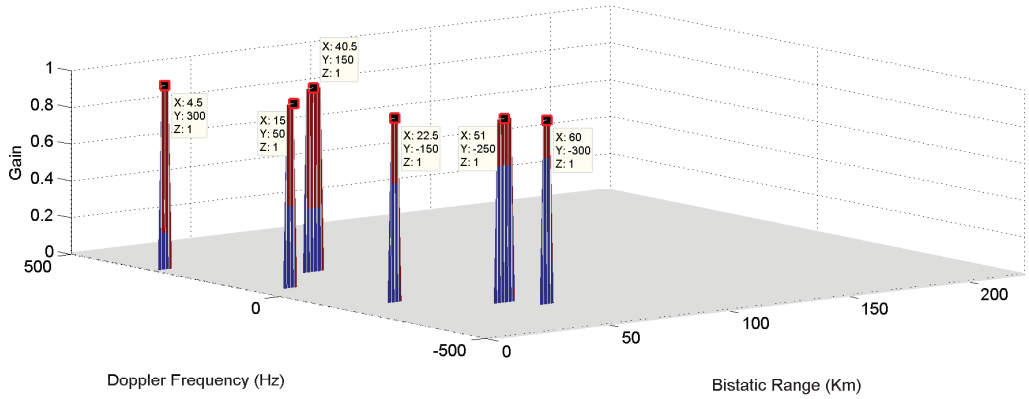

(a)

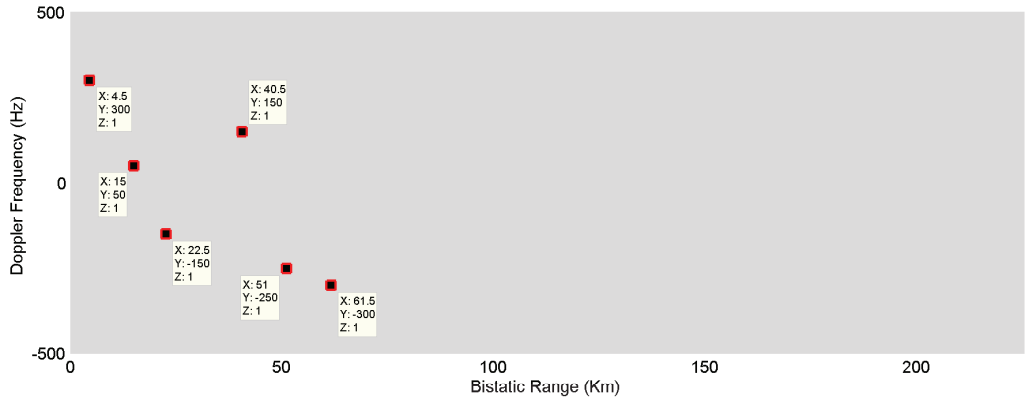

(b)

Figure 2.15: Range-Doppler map for CFAR algorithm with training cell size 20, guard cell size 10, $P_{fa} = 10^{-7}$: (a) 3D plot; (b) view from the top.

Although more simulations can be done with different probability of false alarm rates, training and guard cells, these plots are sufficient to comment on the relationship between CFAR and PBR system. As can be seen from Figure 2.15, all targets are detected successfully without any false alarms even though there are false alarms in Figures 2.12, 2.13 and 2.14, so we can say that the best results are observed with lower P_{fa} values. In addition, 6 targets are detected for all of them. True target detection performance increases as the probability of false alarm decreases because the system scenario has low SNR-valued targets, which can be regarded as noise. Moreover, one can understand, by comparing Figures 2.12 and 2.13, that the detection performance also increases if we increase the

training cell size.

2.6 Summary

In this chapter, some properties of passive bistatic radar are introduced. The bistatic geometry is shown schematically and the bistatic range, Doppler frequency, radar cross section (RCS) and range resolution are explained in detail. Bistatic radar equation is given to predict the performance. After giving background information, a system scenario is given as an example with some targets and clutters specifications, such as the bistatic range, the Doppler frequency and the gain. Then, this scenario is implemented by using the ambiguity function and plotted. By the way, stereo FM signals are created for commercial broadcast and described in detail in Appendix A. Adaptive filter theory is also reviewed. Adaptive filters are applied to cancel clutters/multipath effects that form unwanted peak/s at zero Doppler frequency in the range-Doppler map. For this purpose, LMS and RLS adaptive filters are applied and compared in performances. LMS method is the best method according to performance comparasion and used in all parts of this thesis. The detection of targets can be done by using the CFAR algorithm with different specifications. CFAR algorithm is also simulated within the PBR system scenario and performance results are presented.

Chapter 3

Denoising for Range-Doppler Target Detection Within Compressive Sensing Framework and PES-ℓ_1

Compressive Sensing (CS) theory has become a relatively recent research area used in various signal processing applications, such as photography [26], medical imagining [27] and sensor networks [28,29]. One of the applications is radar target detection [30–33]. CS approach can be used in radar signal processing because of inherently sparse nature of the range-Doppler domain [34]. As indicated in [35], CS is applied to pulse compression, radar imaging and DoA estimation. Above referenced papers describe applications of CS theory to active radar systems.

In many cases, the ambiguity function turns out to be very noisy. In this chapter, the ambiguity function is denoised by using the CS methods, such as Basis Pursuit (BP), Orthogonal Matching Pursuit (OMP) [36], Compressive Sampling Matched Pursuit (CoSaMP) [37], Iterative Hard Thresholding (IHT) [38]. Also, a new denoising method based on the projection onto the epigraph set of the ℓ_1 ball is developed for this purpose [39, 40].

3.1 Compressive Sensing

The main purpose of this section is to review the compressive sensing framework and describe how it can be implemented in PBR systems. Many review articles in the literature can be found about CS in [41].

According to Nyquist-Shannon theorem, it is possible to reconstruct a band-limited signal, if it is sampled with a sampling frequency twice the highest frequency of the signal. The CS theory researchers claim that the sampling with a Nyquist rate is not necessary, if the signal is sparse in some transform domain. It is possible to represent "big signal data" as small data in a subspace or a set in the transform domain. This is also the main idea in most digital waveform coding schemes. Recent image and signal denoising methods also assume the sparse nature of the signal in some transform domain such as Fourier, DCT and/or wavelet domains [42, 43]. As a solution, CS reconstruction algorithms are developed for sparse signal reconstruction problems. The same set of algorithms can also be used in signal denoising. Compressive sensing theory enables us the reconstruction of a sparse signal from a small number of measurements.

Transform domain representation of the CS framework is reviewed below. Suppose that we have a one-dimensional, discrete-time signal $\mathbf{v}$, which is the $N \times 1$ column vector. Any signal can be constructed from its $N \times 1$ basis vectors. Using the $N \times N$ basis matrix, $\Psi = [\psi_1|\psi_2|...|\psi_N]$, the signal $\mathbf{v}$ can be formed as follows:

$$\mathbf{v} = \sum_{i=1}^{N} x_i \psi_i \qquad \text{or} \qquad \mathbf{v} = \Psi \mathbf{x}, \tag{3.1}$$

where $\Psi \in \mathbb{C}^{N \times N}$ is a non-singular, and generally orthonormal transform domain, $\mathbf{x}$ is the $N \times 1$ column vector of weighting coefficients and $\mathbf{v}$ is the non-sparse signal in domain Ψ. Clearly, signals $\mathbf{v}$ and $\mathbf{x}$ are different representations of the same signal, with $\mathbf{v}$ is in the time domain and $\mathbf{x}$ is in the Ψ domain. Using non-singularity property of Ψ, the sampled signal can be calculated as follows:

$$x_i = \psi_i^H \mathbf{v}, \tag{3.2}$$

where $.^H$ denotes the Hermitian transpose operation. Furthermore, if it is enough to represent the signal $\mathbf{v}$ with K basis vectors for $K << N$, the signal $\mathbf{v}$ is called K-sparse. It means that K of s_i's are nonzero and rest of them, $N-K$ are zero.

To illustrate the transform domain representation, let us give a simple example. Suppose that time-sampled signal $\mathbf{v} \in \Re^{512}$ as shown in Figure 3.1(a). All elements are non-zero in the time domain representation. The basis matrix Ψ is selected Inverse Discrete Fourier Transform (IDFT) matrix with 512×512 size because the time-sampled signal has 512 samples. IDFT matrix can be obtained by calculating the IDFT of identity matrix and it is given by

$$\Psi_{l,p} = \frac{1}{N^2} \sum_{n_x=0}^{N-1} \sum_{n_y=0}^{N-1} I_N(n_x, n_y) e^{j2\pi[n_x l + n_y p]/N}, \tag{3.3}$$

where $I_N(n_x, n_y)$ represents the identity matrix with $N \times N$ size and $\Psi_{l,p}$ is the (l,p)'th element of the matrix Ψ. The sparse signal $\mathbf{x}$ in domain Ψ is shown in Figure 3.1(b). The sparsity level is selected as 25, so there should be 25 peaks in the Fourier domain.

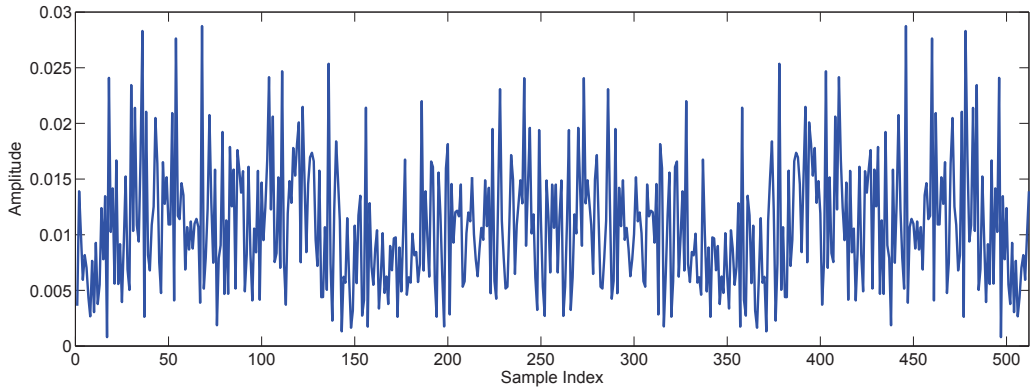

(a)

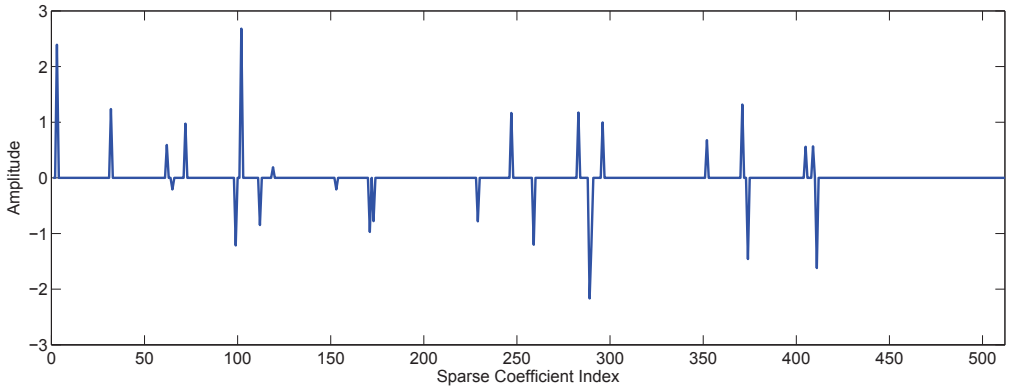

(b)

Figure 3.1: (a) Time-sampled signal $\mathbf{v}$; (b) the sparse signal $\mathbf{x}$ in domain Ψ .

As can be seen from Figure 3.1, it is possible to represent a time-sampled signal $\mathbf{v}$ with length 512 in the other domain Ψ as a sparse signal $\mathbf{x}$ with 25 coefficients. Then, it comes up with an important result that a time-sampled data with length 512 can be compressed to 25 sparse coefficients in another domain for our example. This type of property leads both low computational cost and high efficiency.

Up to now, the transform domain representation is introduced, but the basic idea has not been defined. The main purpose of the CS framework is to represent a sparse signal in some known basis by using a small number set of measurements. If we define the measurement matrix as $\Phi \in \mathbb{C}^{M \times N}$, the observation signal $\mathbf{y}$ is

calculated instead of time-sampled signal $\mathbf{v}$ as follows:

$$\mathbf{y} = \Phi\mathbf{v}, \tag{3.4}$$

where Φ is a $M \times N$ measurement matrix containing zero-mean Gaussian random numbers. The number of random measurements M is smaller than N. As a result, K-sparse vector $\mathbf{v}$ is expressed as follows:

$$\mathbf{y} = \Theta\ \mathbf{x} = \Phi\ \Psi\ \mathbf{x}, \tag{3.5}$$

where $\Theta = \Phi\ \Psi$ is a matrix with $M \times N$ size as $\Theta \in \mathbb{C}^{M \times N}$. In CS reconstruction algorithms, the main purpose is to find the sparse vector $\mathbf{x}$ and this vector can be reconstructed by using the vector $\mathbf{y}$ provided that $K < M < N$. For K-sparse signals, this problem can be solved as follows:

$$\hat{\mathbf{x}} = argmin \parallel \mathbf{x} \parallel_1 \qquad \text{such that} \qquad \mathbf{y} = \Theta\ \mathbf{x}. \tag{3.6}$$

In sparsity based denoising methods there is no measurement matrix and the following problem or related problems are solved:

$$\min_{\mathbf{w}} \parallel \mathbf{w} - \mathbf{v} \parallel_2^2 + \lambda \parallel \mathbf{x} \parallel_1, \tag{3.7}$$

where $\mathbf{v}$ is the observed noisy signal and $\mathbf{x}$ is the transform of $\mathbf{w}$. Another related problem is

$$\min_{\mathbf{w}} \parallel \mathbf{w} - \mathbf{v} \parallel_2^2 + \lambda \parallel \mathbf{w} \parallel_1 . \tag{3.8}$$

In Eq. 3.6, 3.7 and 3.8, the minimization of the ℓ_1 norm is the common feature. Because of the ℓ_1 norm, the solution $\mathbf{w}^*$ turns out to be sparse depending on the nature of the problem in some domain.

Many algorithms have been developed for the above optimization problems. It has beens shown that minimizing the ℓ_1 norm forces small amplitude coefficients of $\mathbf{x}$ vector to zero and it leads to a sparse solution. As pointed out in [44], measurement is not adaptive and does not change according to signal $\mathbf{v}$. There are some problems with that. One of the problems is to create a stable

measurement matrix. To construct the Θ matrix, matrices Φ and Ψ must be maximum incoherent, which requires that rows of the matrix Φ must not be represented sparsely as the columns of Ψ. Another problem is to design a suitable reconstruction method for optimization of the signal. For this problem, many algorithms have been developed. These algorithms can be based on ℓ_0, ℓ_1 and ℓ_2 norm reconstruction. It is shown in [30] that ℓ_0 and ℓ_2 norm reconstruction is not suitable to find K-sparse solution, but optimization based on ℓ_1 norm is shown to recover K-sparse signals exactly. Unlike convex optimization methods, there are also greedy techniques to find the optimal solution. In the following section, the ambiguity function is denoised using the CS approach with different reconstruction methods for the range-Doppler radar target detection.

3.2 Reconstruction Algorithms

This section describes how to implement the CS algorithm in PBR systems. It also describes what kind of reconstruction algorithms should be used for denoising the range-Doppler map. For this purpose, there is a need to recall Section 2.4, which states that the correlation of surveillance and reference signals $\mathbf{b}_l[i] = s_{surv}[i]s^*_{ref}[i-l],\ l = 0, 1, ...L = 150,\ i = 0, 1, ...N-1 = 4095$ may determine the range and the speed of the target(s). We know that the DFT of the correlations $\mathbf{b}_l[i]$ provides the range-Doppler matrix $\xi[l, p]$ which should be sparse in Fourier domain. We expect to see peaks in the range-Doppler map only at the locations of the target(s). Therefore, we can denoise the range-Doppler map using the state-of-the-art denoising algorithms using the sparsity assumption. We can assume both the ambiguity function $\xi[l, p]$ or $\mathbf{b}_l[i]$ as the measured "signal" in a typical PBR system and pose ℓ_1 optimization problems based on them. The relation between $\xi[l, p]$ and $\mathbf{b}_l[i]$ can be expressed as follows:

$$\mathbf{b}_l = \Psi\ \boldsymbol{\xi}_l\ , \qquad l = 0, 1, ..., L.\ , \tag{3.9}$$

where the vector $\boldsymbol{\xi}_l$ is the l'th row of $\xi[l,p]$ and its size is $N = 4096$ in this thesis. We can define an observation signal $\mathbf{y}_l$ which is calculated as follows:

$$\mathbf{y}_l = \Phi \ \mathbf{b}_l, \tag{3.10}$$

$$\mathbf{y}_l = \Theta \ \boldsymbol{\xi}_l = \Phi \ \Psi \ \boldsymbol{\xi}_l, \tag{3.11}$$

where Θ is a matrix of size $M \times N$. Therefore, the observation signal $\mathbf{y}_l$ is of size M, which is smaller than N. In this chapter, several M values are selected and the CS problem is posed as reconstruction of $\xi[l,p]$ from $\mathbf{y}_l$ vectors. Since sparsity assumption is used, denoising is also achieved during the CS reconstruction. Another approach is to denoise $\boldsymbol{\xi}_l$ vectors without using any measurement matrix. In this case, the following problem is solved:

$$\min_{w} \parallel \mathbf{w}_l - \boldsymbol{\xi}_l \parallel_2^2 + \lambda \parallel \mathbf{w}_l \parallel_1 . \tag{3.12}$$

The solution $\mathbf{w}_l^*$ will be the denoised vector. Both the complex and magnitude of $\boldsymbol{\xi}_l$ can be used. There are many stable reconstruction methods based on ℓ_1 minimization for noisy measurements in the literature [45, 46]. In this thesis, basis pursuit (BP), orthogonal matching pursuit (OMP), compressive sampling matched pursuit (CoSaMP), iterative hard thresholding (IHT) are used. In addition, the PES-ℓ_1 method is proposed to denoise the range-Doppler map.

3.2.1 Basis Pursuit

Basis Pursuit (BP) solves the optimization problem 3.13 and searches the best representation of a signal by minimizing the ℓ_1 norm of the vector $\boldsymbol{\xi}_l$. The main goal is to find the sparsest possible representation of the vector $\boldsymbol{\xi}_l$. Therefore, each observation vector, $\mathbf{y}_l$ is used in the following minimization problem:

$$\min \parallel \boldsymbol{\xi}_l \parallel_1 \qquad \text{such that} \qquad \mathbf{y}_l = \Theta \ \boldsymbol{\xi}_l. \tag{3.13}$$

The above CS reconstruction problem is solved for each row of the AF function for the values of $l = 0, 1, ..., L$. To deal with noisy data, a related approach

called basis pursuit denoising (BPDN) can be also used to solve mathematical optimization problem of the form:

$$\min \| \mathbf{y}_l - \Theta \boldsymbol{\xi}_l \|_2^2 + \lambda \| \boldsymbol{\xi}_l \|_1, \tag{3.14}$$

where λ is the parameter determining the sparsity level of the solution. It is clear that this problem becomes a least square problems for $\lambda = 0$. In our experiments, different λ values are used and results for various λ are presented.

3.2.2 Orthogonal Matching Pursuit

Orthogonal Matching Pursuit (OMP) is a greedy algorithm that also determines a sparse solution to the CS problem. It is an extension of the Matching Pursuit (MP) algorithm. Advantages of this algorithm are its speed and computational efficiency. It is also used at the output of the matched filter to find the strongest target in [47]. OMP constructs an approximation with an iteration process. Given a compressed observation vector $\mathbf{y}_l$ for $l = 0, 1, ..., L$, the locally optimum solution is tried to be calculated at each iteration. To do this, it searches which columns of Θ contributing most to the observation vector $\mathbf{y}_l$, which means that residual vector $\mathbf{r}$ should resemble the column vector in Θ [48]. The residual vector is taken as the observation vector $\mathbf{r} = \mathbf{y}_l$ at the first iteration. It is hoped that local optimum solutions are going to result the global optimum solutions, but this algorithm does not guarantee the global optimum. During each iteration, columns of Θ are picked and correlated with the the resdiual $\mathbf{r}$ and this correlation is subtracted form the previously selected vector $\mathbf{r}_{t-1}$ at each iteration. OMP algorithm keeps on iterating until the norm of resulting residual smaller than a some halting threshold. After M iterations, this algorithm finds a set of columns from the basis set representing the vector $\boldsymbol{\xi}_l$. OMP uses a least-squares at each iteration to update residual vector $\mathbf{r}$. Lastly, total computational complexity increases linearly as K increases [36].

3.2.3 Compressed Sampling Matching Pursuit

Compressive Sampling Matched Pursuit (CoSaMP) is an iterative greedy algorithm that recovers a compressible signal from its noisy samples [37]. It is efficient for some optimization problems. CoSaMP is one of the latest algorithms based on OMP. It also considers a number of vectors to generate approximation at each step. It requires a measurement vector Θ, observation matrix $\mathbf{y}_l$ and a sparsity level estimation (K). Different form OMP, CoSaMP does not search the maximum correlation. It takes $2K$ dictionary vectors with the largest normalized inner products. After calculating intersection between current solution set and a set of $2K$ column vectors of Θ, the solution is obtained with least-squares. Then, CoSaMP iterates until the stopping criteria is satisfied. CoSaMP algorithm changes the solution vector at each iteration, so this property enables to correct previous errors.

3.2.4 Iterative Hard Thresholding

Iterative hard thresholding (IHT) algorithm is a simple iterative method [38]. It can be considered that it is a different algorithm from the previous ones. This algorithm is not based on OMP. The convergence of this algorithm is guaranteed in [49] under condition that ℓ_2 norm of matrix Θ smaller than 1 ($\| \Theta \|_2 < 1$). IHT is supposed to exhibit similar performance with CoSaMP [48]. Some properties of this algorithm are as follows: (i) it is robust to observation noise and it(ii) succeeds with a minimum number of observations. Basically, IHT algorithm uses the following update equation:

$$\boldsymbol{\xi}_{l,t+1} = H_n(\boldsymbol{\xi}_{l,t} + \Theta^T(\mathbf{y}_l - \Theta\boldsymbol{\xi}_{l,t})) \tag{3.15}$$

where $H_n(.)$ denotes the operator that reduces the value of ℓ_0 at each iteration for n sparse entries. First solution vector $\boldsymbol{\xi}_{l,0}$ is taken as zero. The Eq. 3.15 is repeated until a threshold is satisfied.

3.3 Projection Onto the Epigraph Set of the ℓ_1 ball (PES-ℓ_1)

Projections Onto Epigraph Set Of A Convex Cost Function (PES-ℓ_1) is a new signal processing framework described in [39, 40]. In this new denoising method, each row of the magnitude of AF data: $\xi_l[p] = |\xi[l,p]|$ is first filtered by a low-pass filter with cut-off $\pi/4$ (normalized angular frequency) and subtracted from the original data, producing a high-pass filtered version $\xi_{high}[p]$. Let the low-pass filtered version be $\xi_{low}[p]$. The signal $\xi_{high}[p]$ is projected onto the epigraph set of ℓ_1-norm function. The output of the projection operation $\xi_{out}[p]$ is combined with the low-pass signal $\xi_{low}[p]$ to obtain the denoised version of $|\xi[l,p]|$ as discussed in [50–52]. This denoising method takes advantage of the sparse nature of the data and it does not require any measurement matrix. The block diagram of the denoising structure is shown in Figure 3.2.

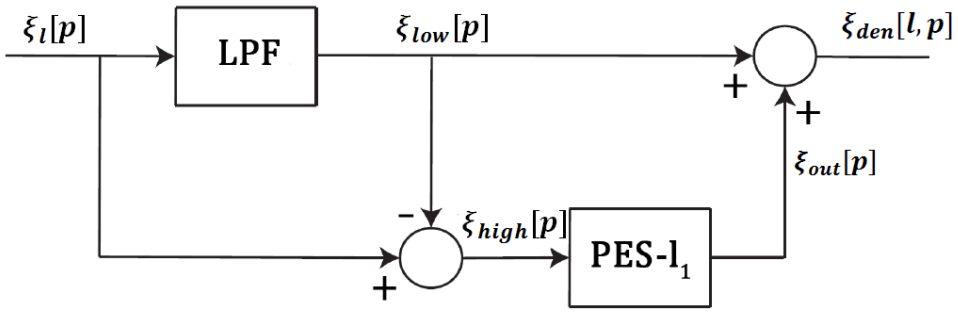

Figure 3.2: The block diagram of PES-ℓ_1 algorithm.

In PES-ℓ_1 block, the signal $\mathbf{v}_{high}[p]$ is processed by projection onto epigraph set of ℓ_1-ball as said before and the projected signal $\mathbf{v}_{out}[p]$ is obtained after that. Firstly, $[\mathbf{v}_{high}[p], 0]^T$ is projected onto the nearest hyperplane of the epigraph set shown as follows:

$$\sum_{p=0}^{K-1} sign(\mathbf{v}_{high}[p])\mathbf{v}_{high}[p] - z = 0, \tag{3.16}$$

where z is the boundary condition of the ℓ_1-ball expressed as follows:

$$\sum_{p=0}^{K-1} |\mathbf{v}_{high}[p]| \leq z. \tag{3.17}$$

The projection signal $\mathbf{v}_{out}[p]$ can be calculated as follows:

$$\mathbf{v}_{out}[p] = \mathbf{v}_{high}[p] - \frac{\sum_{p=0}^{K-1} sign(\mathbf{v}_{high}[p])\mathbf{v}_{high}[p]}{K+1} sign(\mathbf{v}_{high}[p]) \tag{3.18}$$

3.4 Simulation Results

This section presents the simulation results of each method mentioned above. In Figures 3.4,. . . ,3.15, range-Doppler maps based on same PBR system scenario with 6 targets and 6 clutters mentioned in Table 2.2 are denoised with basis pursuit (BP), orthogonal matching pursuit (OMP), compressive sampling matched pursuit (CoSaMP), iterative hard thresholding (IHT) with different M values for each and the PES-ℓ_1 method, respectively. BP algorithm needs λ values for BPDN, so λ is chosen as 0.1, 1,and 5 in this thesis. As known from previous sections, sparsity levels should be estimated for OMP, CoSaMP and IHT methods, so the estimated sparsity level is $K = 10$ for the given plots. In addition to $K = 10$, different sparsity levels, such as $K = 50$ and $K = 100$ are calculated. PSNR (dB), SNR (dB), time (sec.) values of each method with sparsity levels and λ values and the number of the detected targets are presented in Tables 3.1 and 3.2.

Tables 3.1 and 3.2 show us PES-ℓ_1 method outperforms CS algorithms with $49,15$ dB PSNR value and $7,68$ dB SNR value. As can be seen, higher scores in terms of PSNR and SNR are generally obtained for $M = 400$ and higher number of measurements. Even though M values should be smaller than N value, $M = 4096$ condition is also calculated because our aim is to use the CS idea for denoising in this thesis. According to "Time" column, PES-ℓ_1 is one of the fastest methods with $6,70$ sec. However, there can be many possible scenarios to compare the performances of these methods, so measurements between %1-%70

of measurements are calculated for four methods with $K = 10, 50, 100$ sparsity level estimations and shown in Figure 3.3. The red dashed line points the PES-ℓ_1 method for both of them. As can be observed, PES-ℓ_1 still outperforms the CS algorithms, but not all. In general, OMP, CoSaMP and IHT methods have higher PSNR and SNR values for $K = 10$ after %10 of measurements as compared to PES-ℓ_1 method.

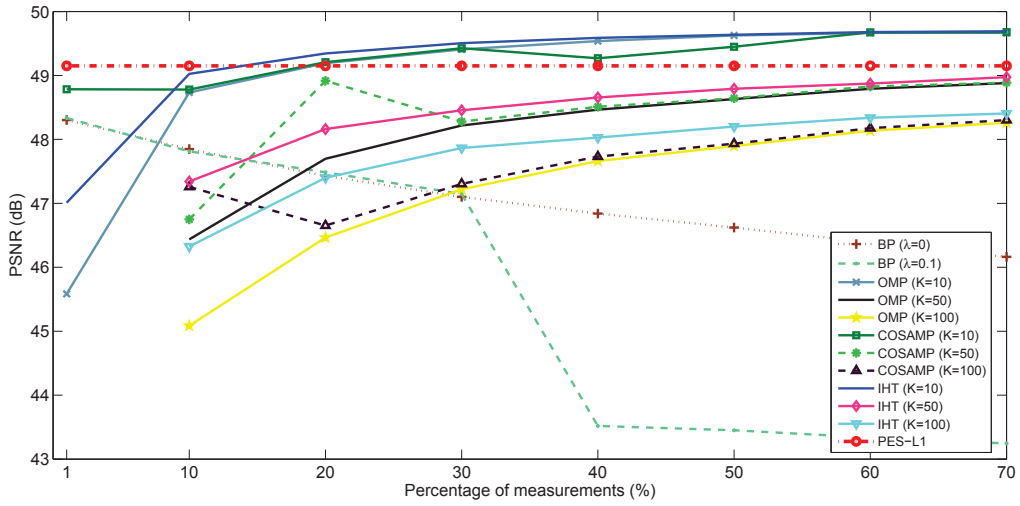

(a)

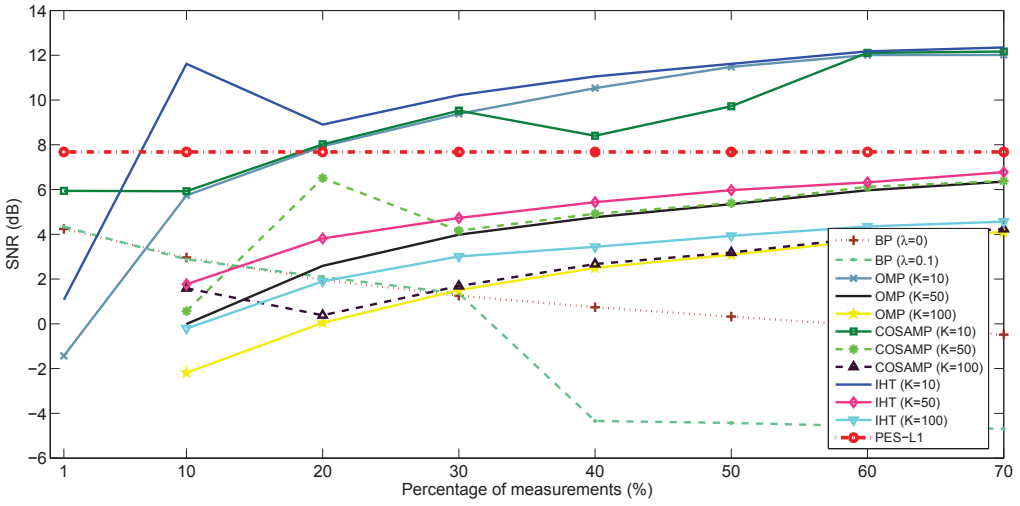

(b)

Figure 3.3: (a) PSNR; and (b) SNR values of CS methods and PES-ℓ_1 in the range of %1 - %70 measurements.

Table 3.1: PSNR, SNR, time values for reconstruction (Time-1), time values for matrix multiplications (Time-2) and the number of the detected targets of methods mentioned above for $M = 40,\ 400,\ 1000$.

Measurements	Methods	PSNR (dB)	SNR (dB)	Time-1 (sec.)	Time-2 (sec.)	No. of detected targets
M=40	BP ($\lambda = 0$)	48,30	4,24	223,01	17,69	2
	BP ($\lambda = 0.1$)	48,33	4,34	145,74		2
	BP ($\lambda = 1$)	48,00	3,36	116,40		2
	BP ($\lambda = 5$)	48,39	4,53	99,51		2
	OMP ($K = 10$)	45,58	-1,43	6,25		2
	CoSaMP ($K = 10$)	48,78	5,94	22,76		2
	IHT ($K = 10$)	47,01	1,08	5,39		2
M=400	BP ($\lambda = 0$)	47,85	2,97	2000,30	108,34	3
	BP ($\lambda = 0.1$)	48,81	2,88	1215,2		4
	BP ($\lambda = 1$)	47,80	2,84	690,60		5
	BP ($\lambda = 5$)	47,63	3,09	3147,7		5
	OMP ($K = 10$)	48,73	5,74	37,70		4
	OMP ($K = 50$)	46,44	-0.01	38,37		2
	OMP ($K = 100$)	45,09	-2,19	1969,5		2
	CoSaMP ($K = 10$)	48,78	5,92	17,67		3
	CoSaMP ($K = 50$)	46,75	0,57	93,54		2
	CoSaMP ($K = 100$)	47,26	1,59	416,36		5
	IHT ($K = 10$)	49,03	7,03	6,82		3
	IHT ($K = 50$)	47,34	1,77	38,98		2
	IHT ($K = 100$)	46,33	-0,20	79,80		2
M=1000	BP ($\lambda = 0$)	47,22	1,51	4787,7	236,43	6
	BP ($\lambda = 0.1$)	47,28	1,64	2177,1		6
	BP ($\lambda = 1$)	47,30	1,67	1878,5		6
	BP ($\lambda = 5$)	47,30	1,66	1041,1		6
	OMP ($K = 10$)	49,37	9,10	13,71		5
	OMP ($K = 50$)	48,00	3,34	79,64		6
	OMP ($K = 100$)	46,91	0,89	209,06		5
	CoSaMP ($K = 10$)	49,33	8,81	11,87		5
	CoSaMP ($K = 50$)	48,02	3,41	42,35		5
	CoSaMP ($K = 100$)	46,98	1,01	236,36		5
	IHT ($K = 10$)	49,41	9,43	9,04		5
	IHT ($K = 50$)	48,42	4,62	12,88		5
	IHT ($K = 100$)	48,32	4,31	30,61		6
PES-ℓ_1		49,15	7,68	6,70		6
FFT based AF		45,51	-1,53	3,87		6

Table 3.2: PSNR, SNR, time values for reconstruction (Time-1), time values for matrix multiplications (Time-2) and the number of the detected targets of methods mentioned above for $M = 2000,\ 4096$.

Measurements	Methods	PSNR (dB)	SNR (dB)	Time-1 (sec.)	Time-2 (sec.)	No. of detected targets
M=2000	BP ($\lambda = 0$)	46,62	0.33	23875	446,99	6
	BP ($\lambda = 0.1$)	46,62	0,32	6763,9		6
	BP ($\lambda = 1$)	46,63	0,34	3098,2		6
	BP ($\lambda = 5$)	46,66	0,40	1916,5		6
	OMP ($K = 10$)	49,62	11,48	60,84		6
	OMP ($K = 50$)	48,63	5,35	270,67		6
	OMP ($K = 100$)	47,90	3,09	757,07		6
	CoSaMP ($K = 10$)	49,45	9,72	39,87		6
	CoSaMP ($K = 50$)	48,64	5,39	123,23		6
	CoSaMP ($K = 100$)	47,93	3,19	368,92		6
	IHT ($K = 10$)	49,64	11,61	21,96		6
	IHT ($K = 50$)	48,79	5,97	122,88		6
	IHT ($K = 100$)	48,20	3,93	153,05		6
M=4096	BP ($\lambda = 0$)	49,9	17,75	18,95	977,76	6
	BP ($\lambda = 0.1$)	49,91	18,17	17,17		6
	BP ($\lambda = 1$)	49,91	17,99	21,93		6
	BP ($\lambda = 5$)	49,92	18,49	18,83		6
	OMP ($K = 10$)	49,72	12,92	53,49		6
	OMP ($K = 50$)	49,07	7,25	551,37		6
	OMP ($K = 100$)	48,50	4,90	1289,1		6
	CoSaMP ($K = 10$)	49,73	12,95	39,74		6
	CoSaMP ($K = 50$)	49,07	7,28	341,93		6
	CoSaMP ($K = 100$)	48,53	4,99	566,57		6
	IHT ($K = 10$)	49,74	13,13	21,99		6
	IHT ($K = 50$)	49,15	7,70	69,11		6
	IHT ($K = 100$)	48,71	5,65	39,79		6
PES-ℓ_1		49,15	7,68	6,70		6
FFT based AF		45,51	-1,53	3,87		6

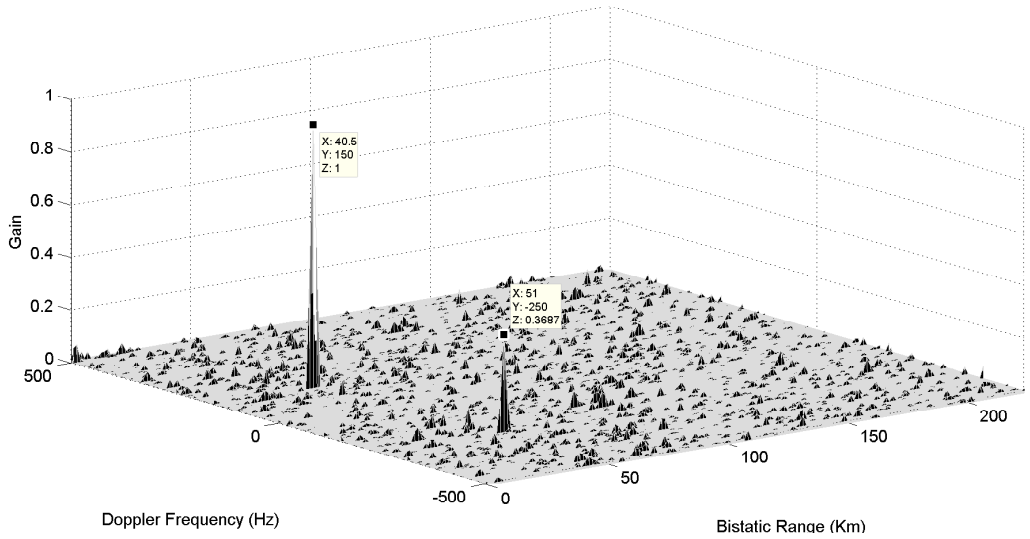

(a)

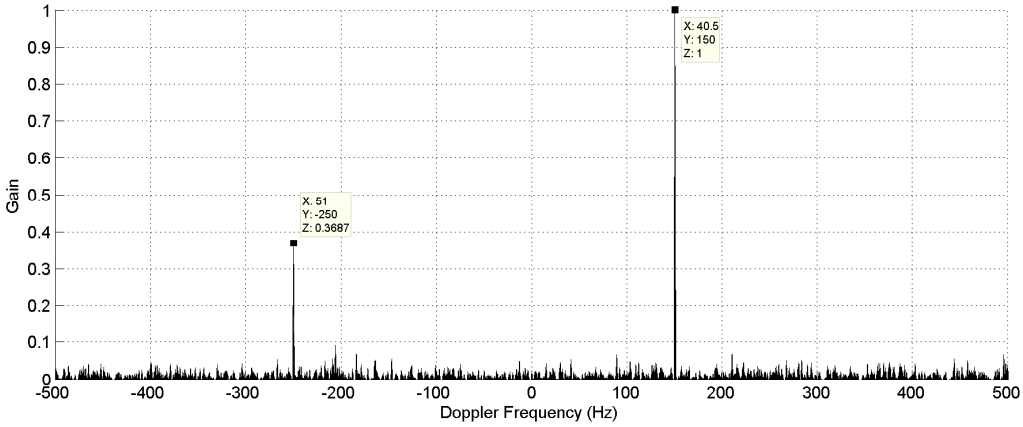

(b)

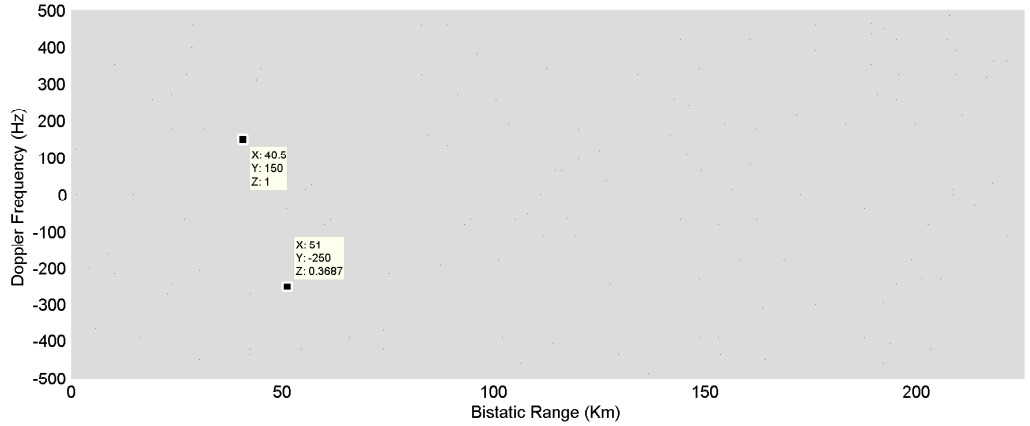

(c)

Figure 3.4: Simulation result for BP with $M = 40$ and $\lambda = 0$: (a) 3D plot; (b) Doppler frequency plot; (c) view from the top.

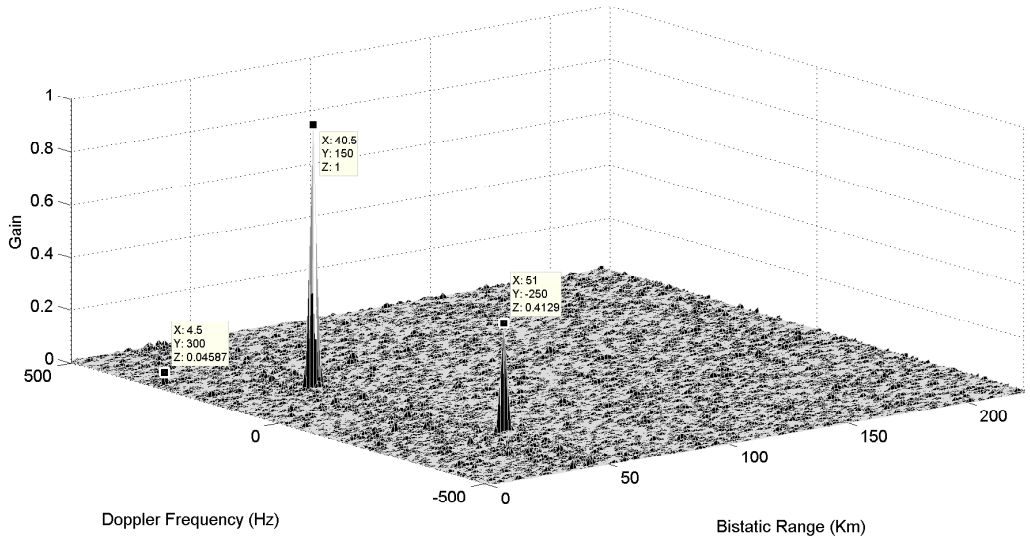

(a)

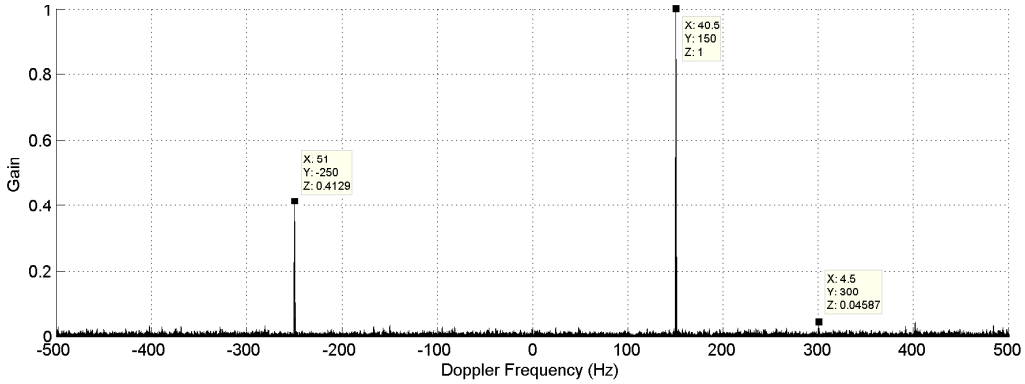

(b)

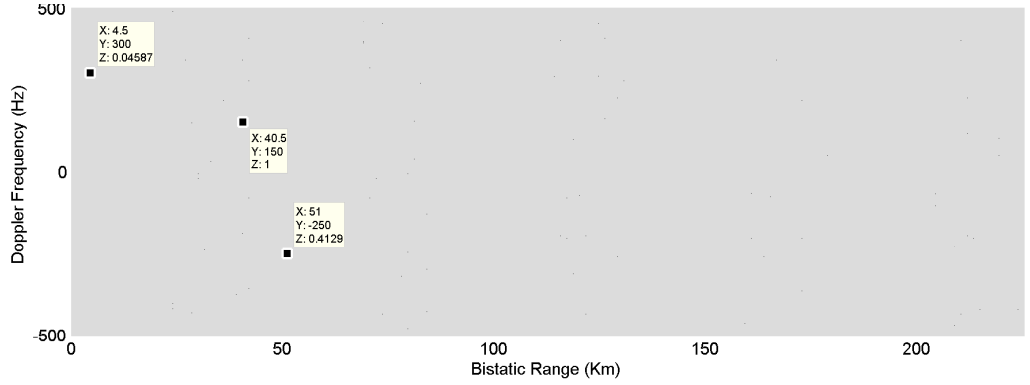

(c)

Figure 3.5: Simulation result for BP with $M = 400$ and $\lambda = 0$: (a) 3D plot; (b) Doppler frequency plot; (c) view from the top.

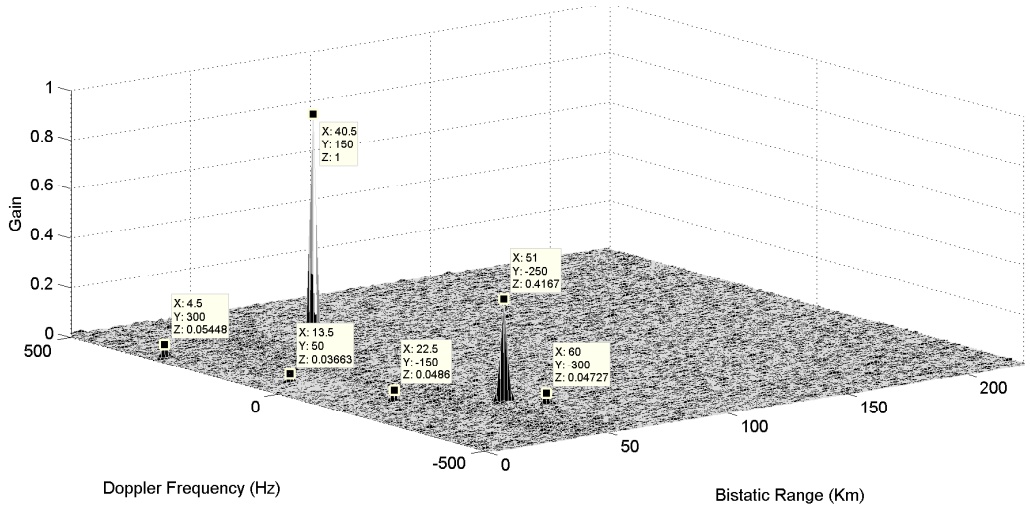

(a)

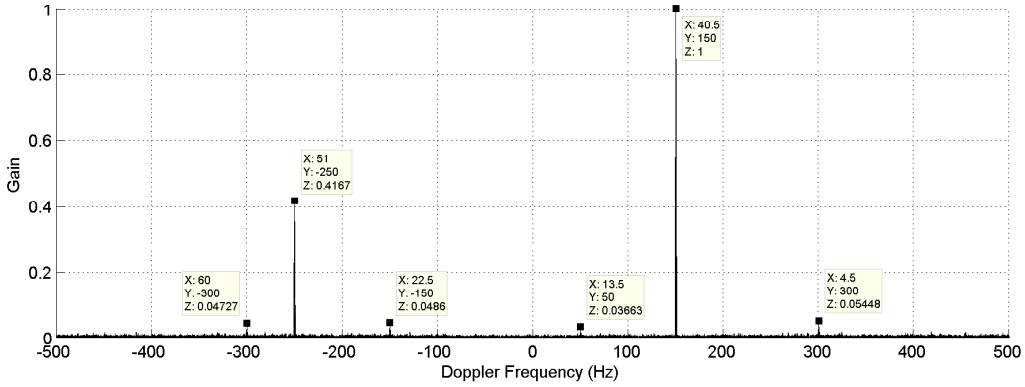

(b)

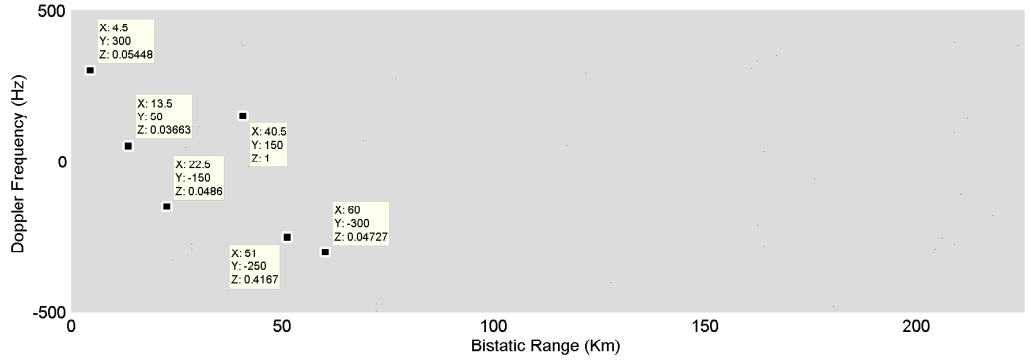

(c)

Figure 3.6: Simulation result for BP with $M = 2000$ and $\lambda = 0$: (a) 3D plot; (b) Doppler frequency plot; (c) view from the top.

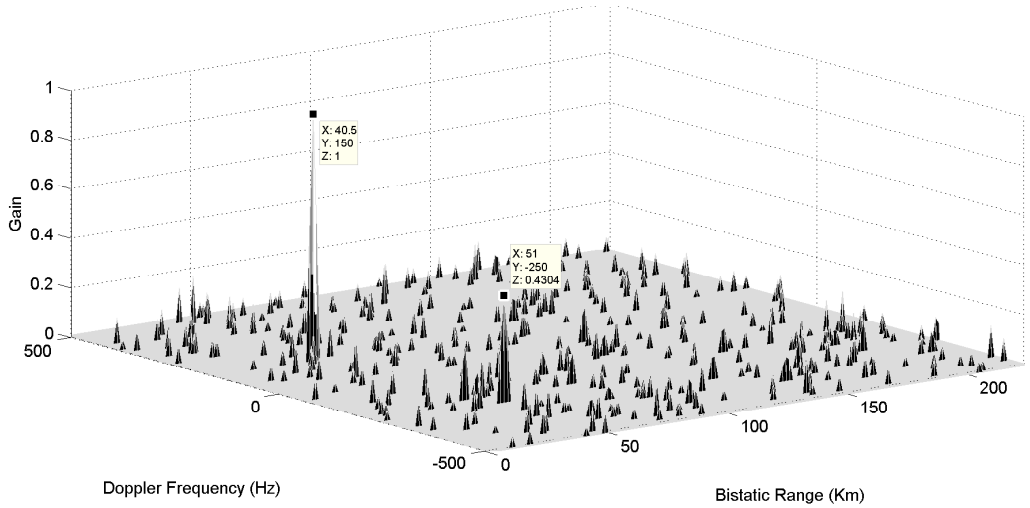

(a)

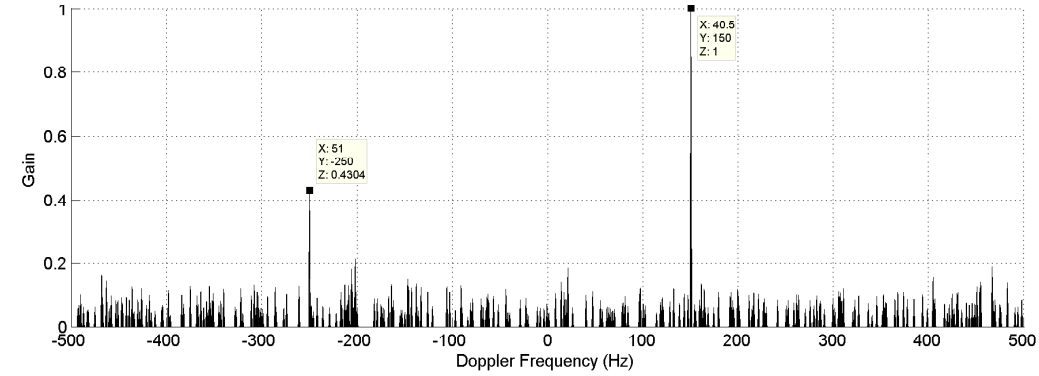

(b)

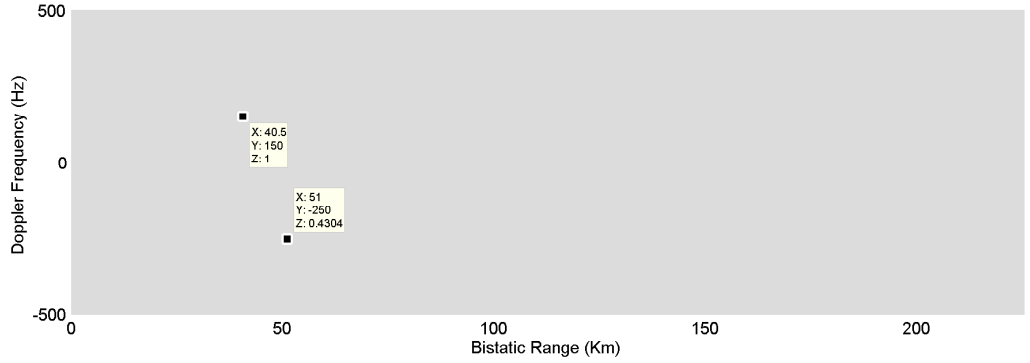

(c)

Figure 3.7: Simulation result for OMP with $M = 40$ and $K = 10$: (a) 3D plot; (b) Doppler frequency plot; (c) view from the top.

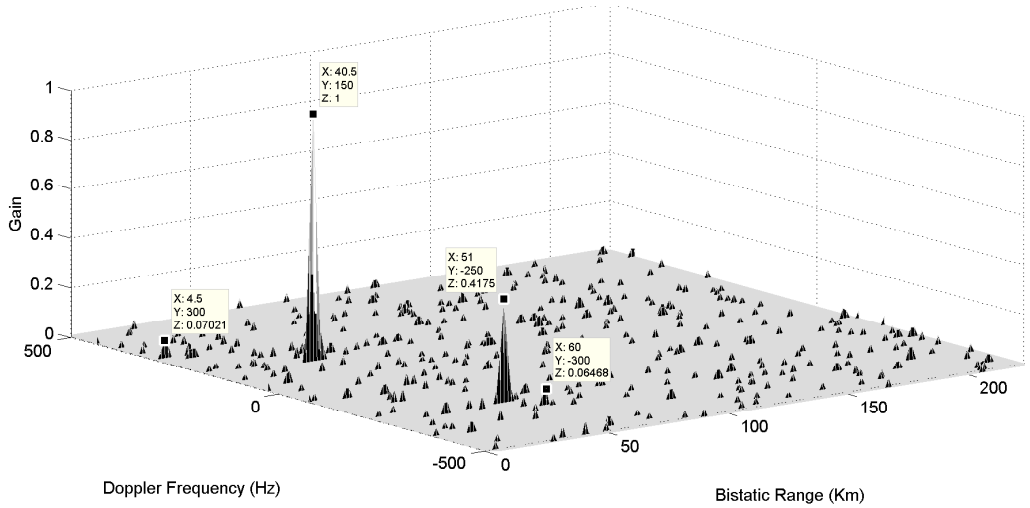

(a)

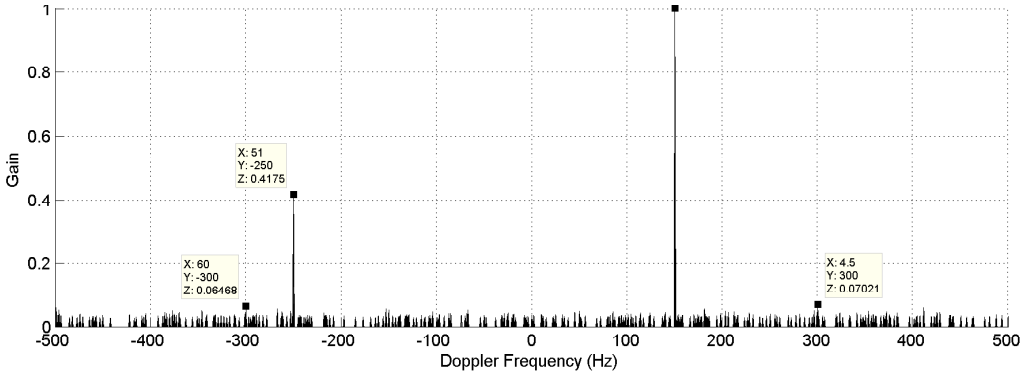

(b)

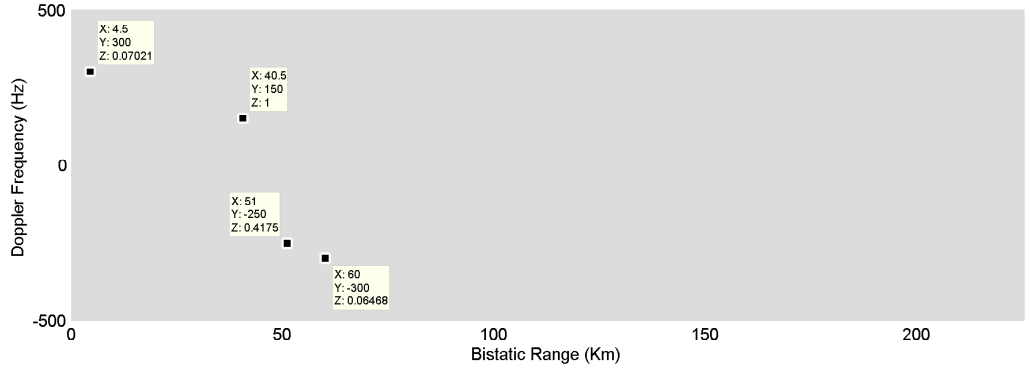

(c)

Figure 3.8: Simulation result for OMP with $M = 400$ and $K = 10$: (a) 3D plot; (b) Doppler frequency plot; (c) view from the top.

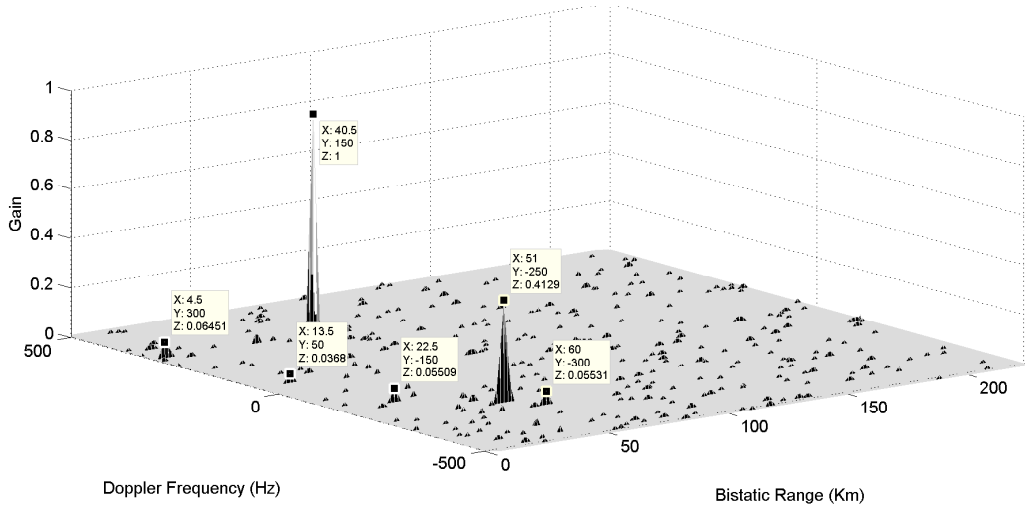

(a)

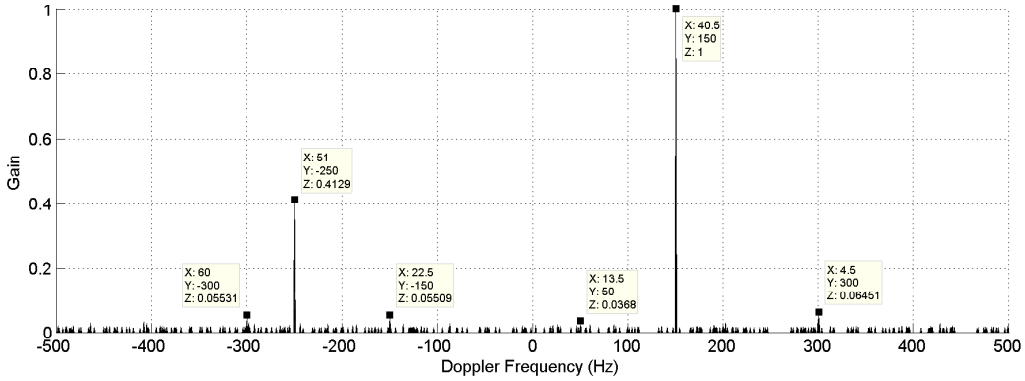

(b)

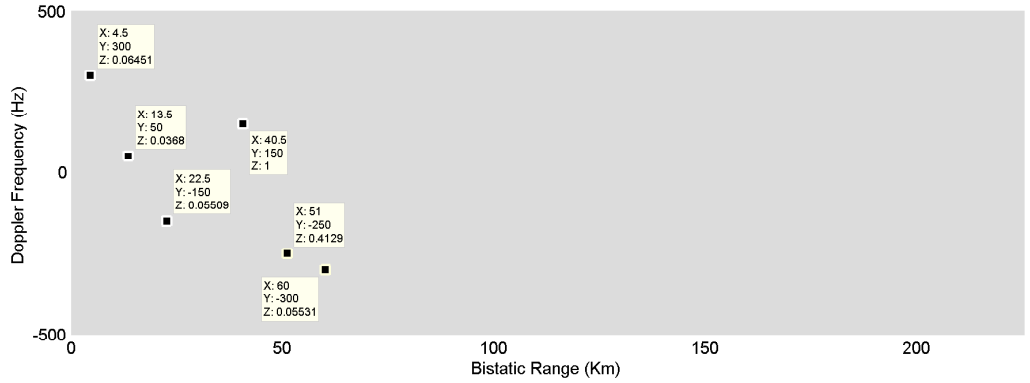

(c)

Figure 3.9: Simulation result for OMP with $M = 2000$ and $K = 10$: (a) 3D plot; (b) Doppler frequency plot; (c) view from the top.

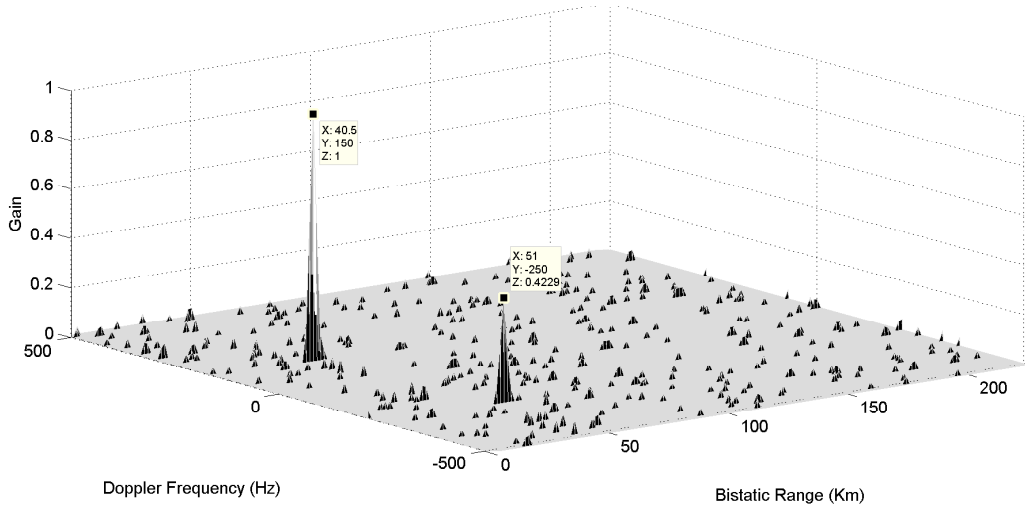

(a)

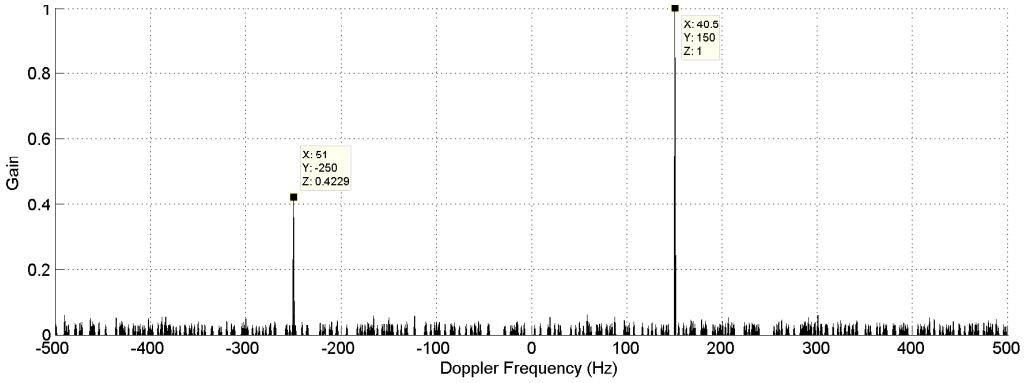

(b)

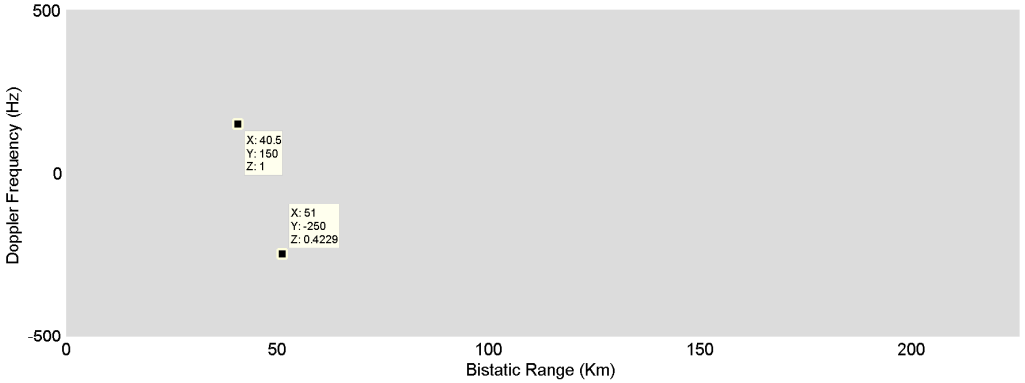

(c)

Figure 3.10: Simulation result for CoSaMP with $M = 40$ and $K = 10$: (a) 3D plot; (b) Doppler frequency plot; (c) view from the top.

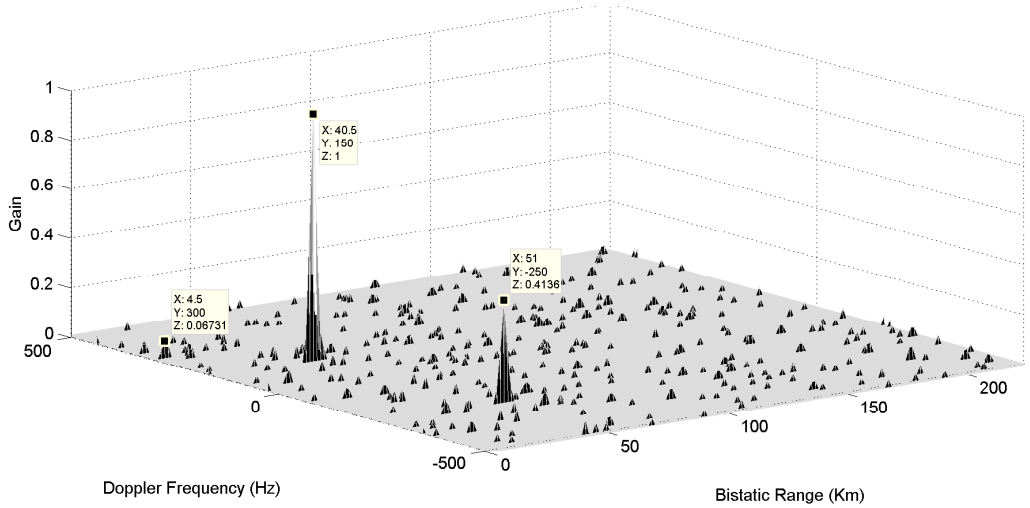

(a)

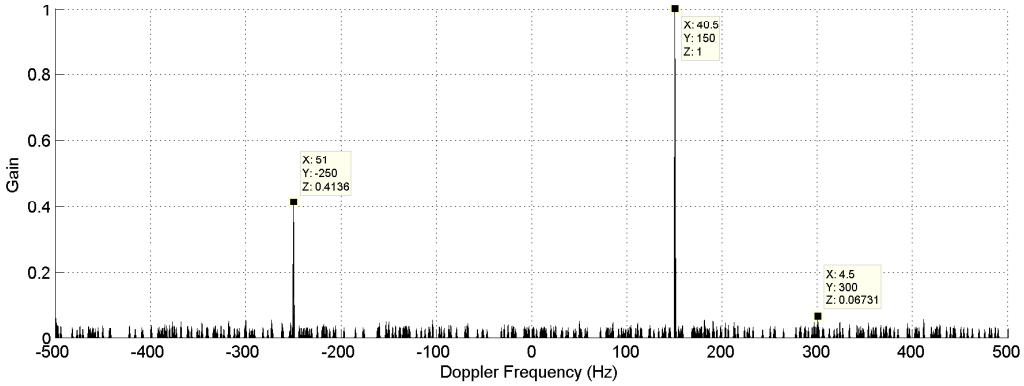

(b)

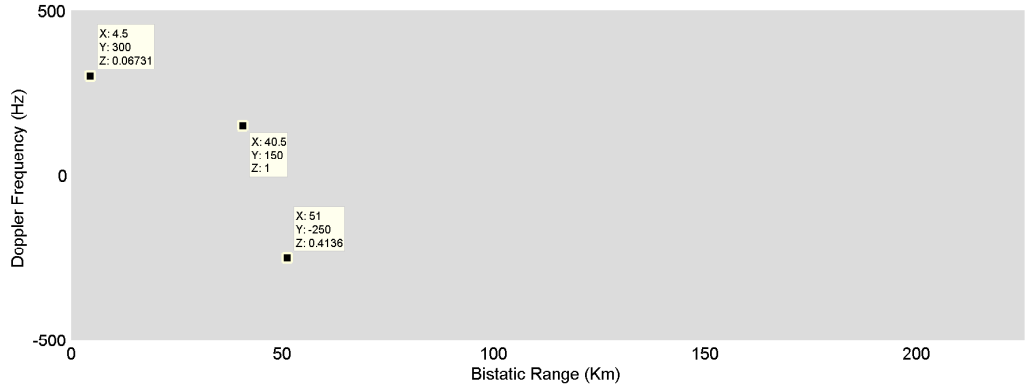

(c)

Figure 3.11: Simulation result for CoSaMP with $M = 400$ and $K = 10$: (a) 3D plot; (b) Doppler frequency plot; (c) view from the top.

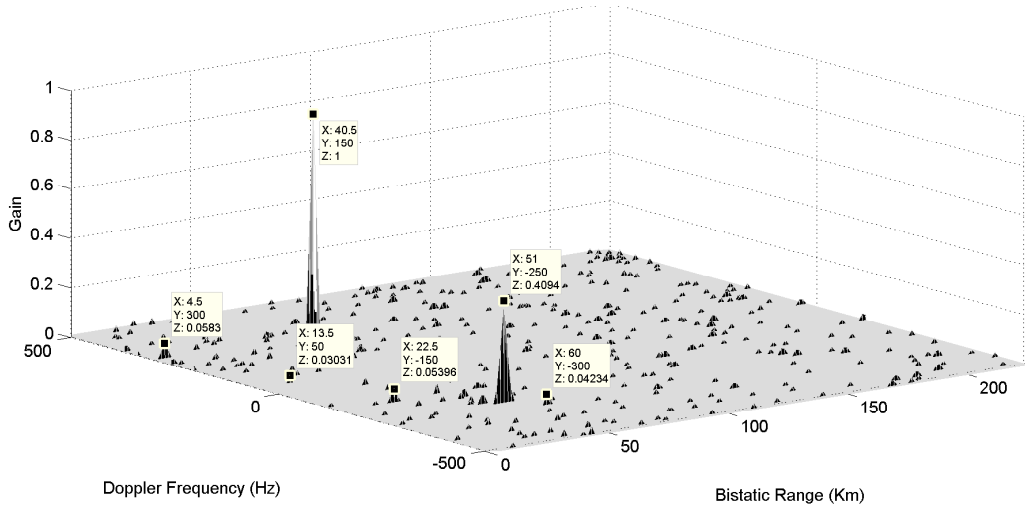

(a)

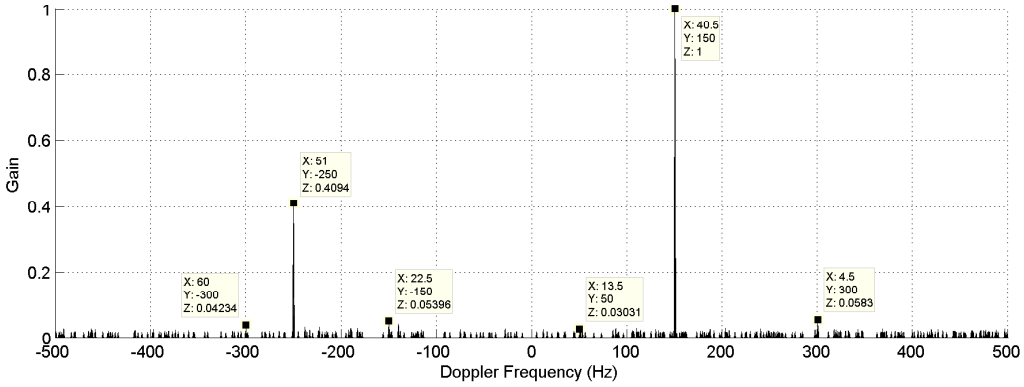

(b)

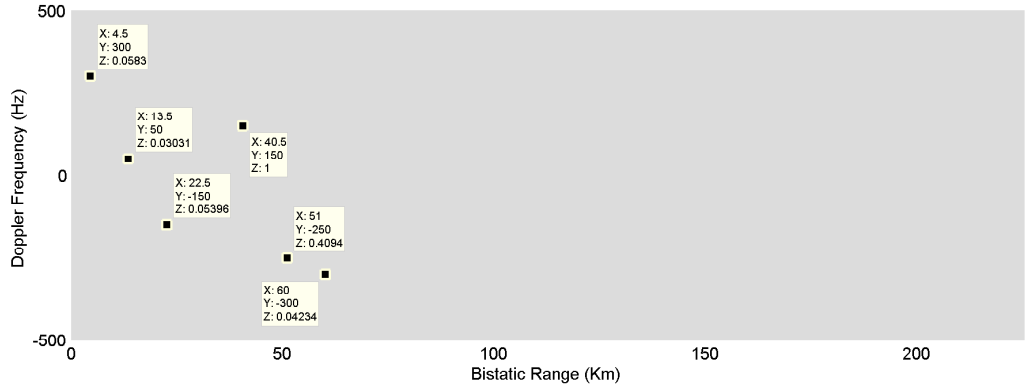

(c)

Figure 3.12: Simulation result for CoSaMP with $M = 2000$ and $K = 10$: (a) 3D plot; (b) Doppler frequency plot; (c) view from the top.

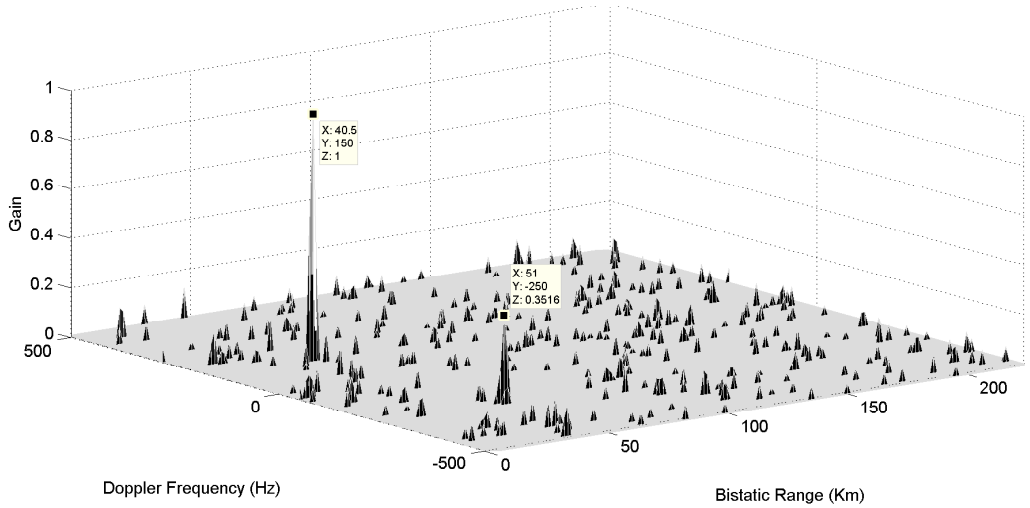

(a)

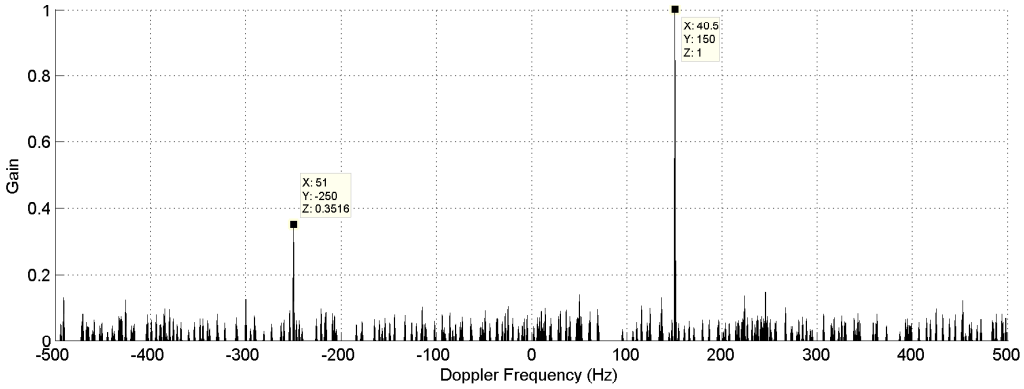

(b)

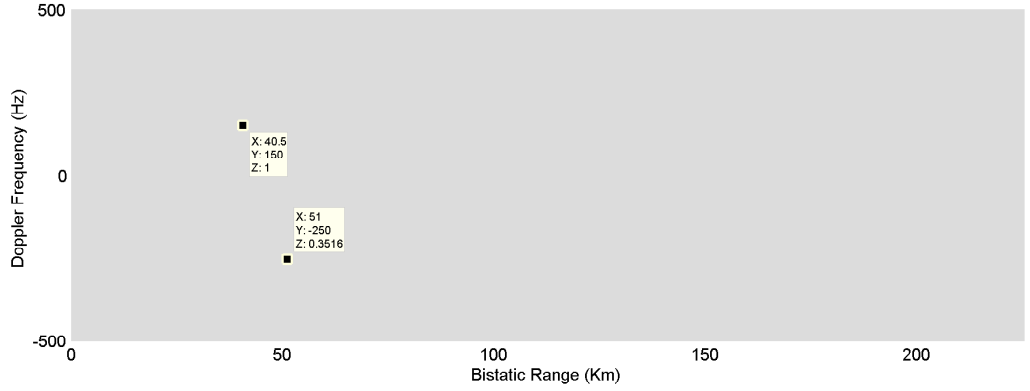

(c)

Figure 3.13: Simulation result for IHT with $M = 40$ and $K = 10$: (a) 3D plot; (b) Doppler frequency plot; (c) view from the top.

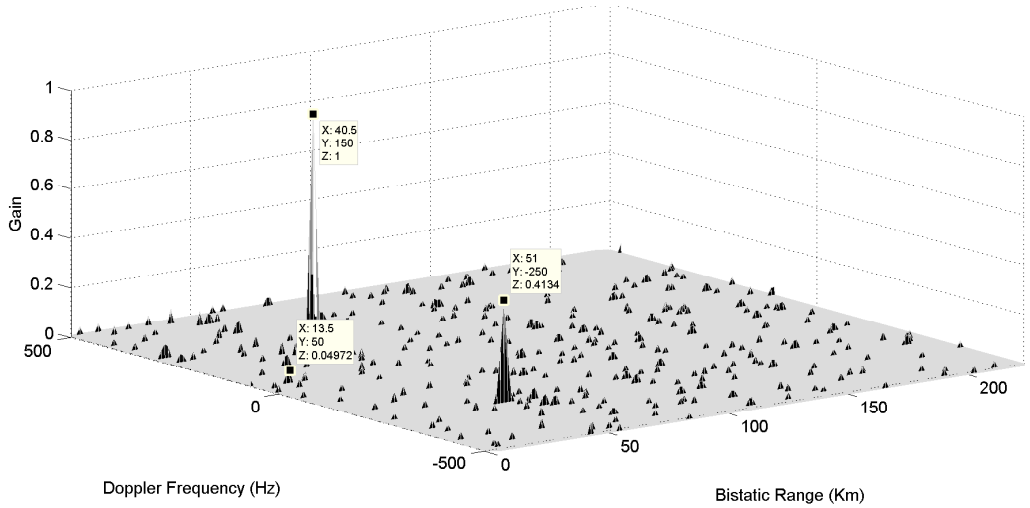

(a)

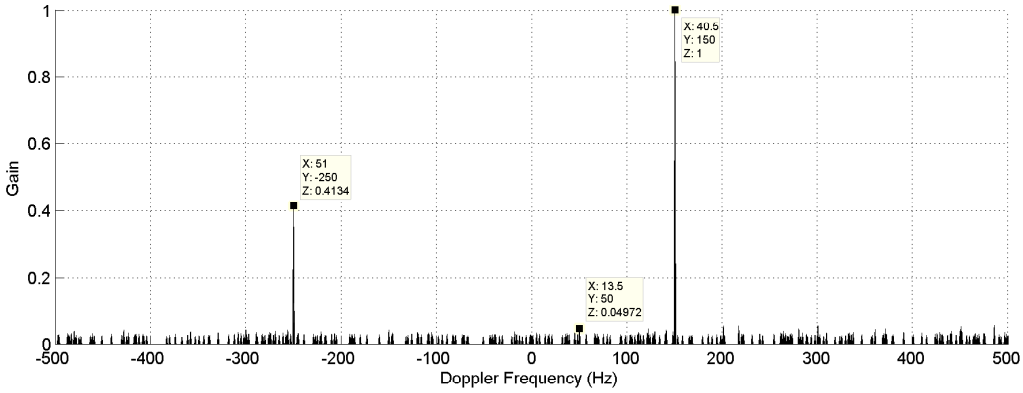

(b)

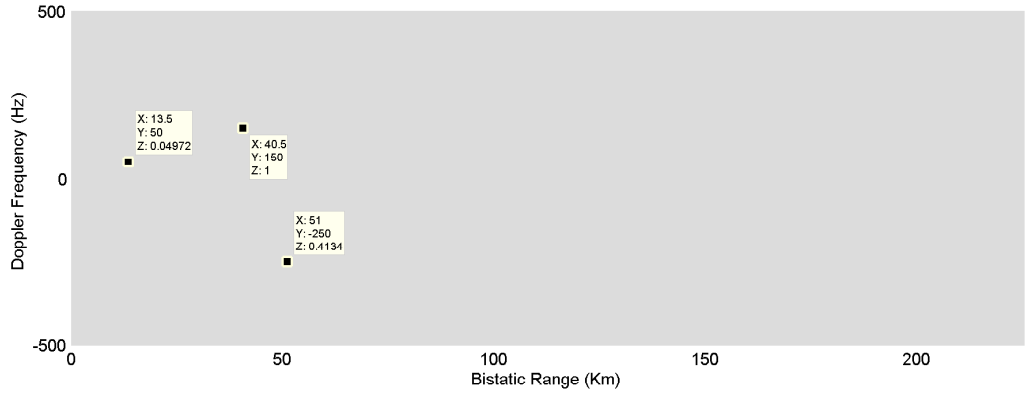

(c)

Figure 3.14: Simulation result for IHT with $M = 400$ and $K = 10$: (a) 3D plot; (b) Doppler frequency plot; (c) view from the top.

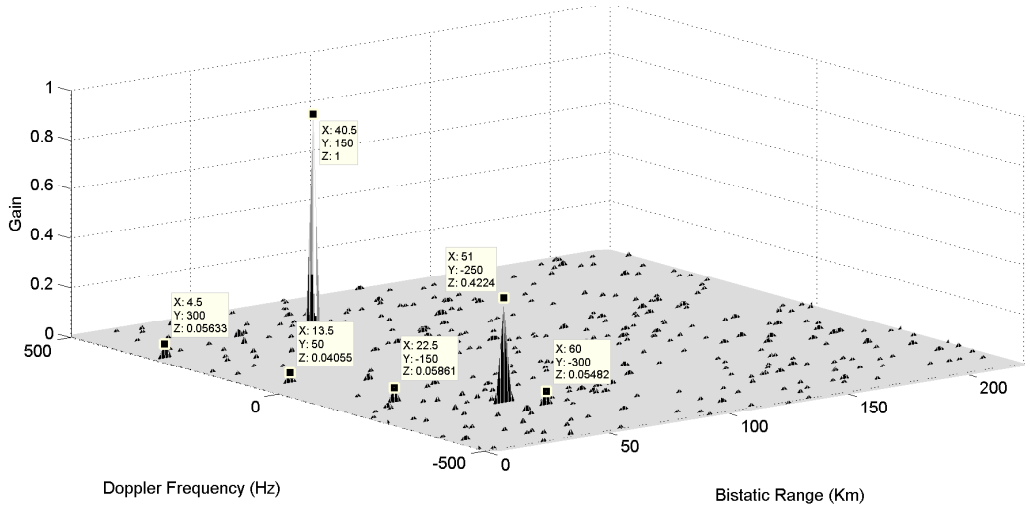

(a)

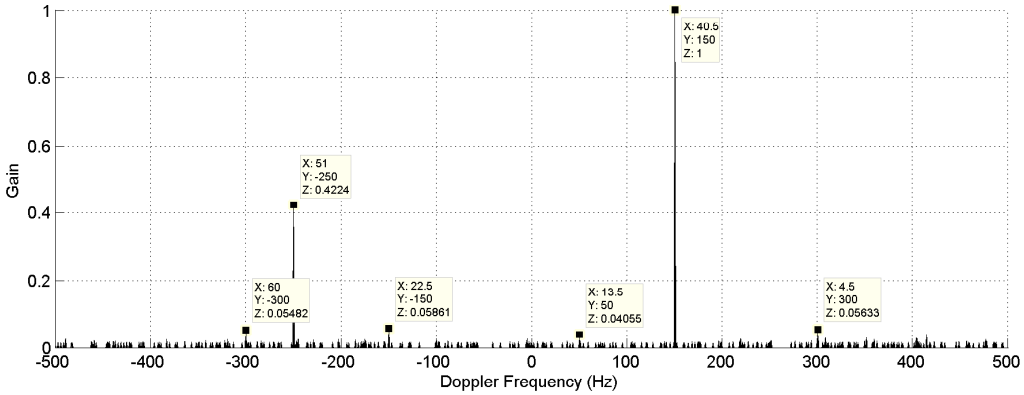

(b)

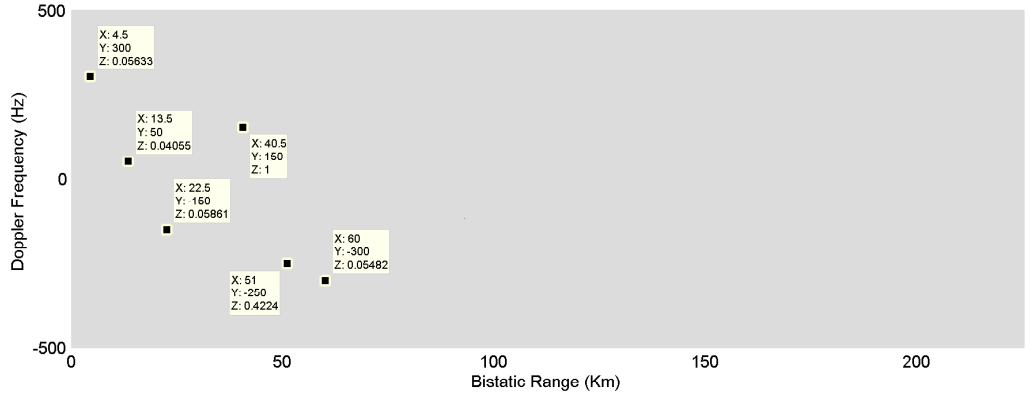

(c)

Figure 3.15: Simulation result for IHT with $M = 2000$ and $K = 10$: (a) 3D plot; (b) Doppler frequency plot; (c) view from the top.

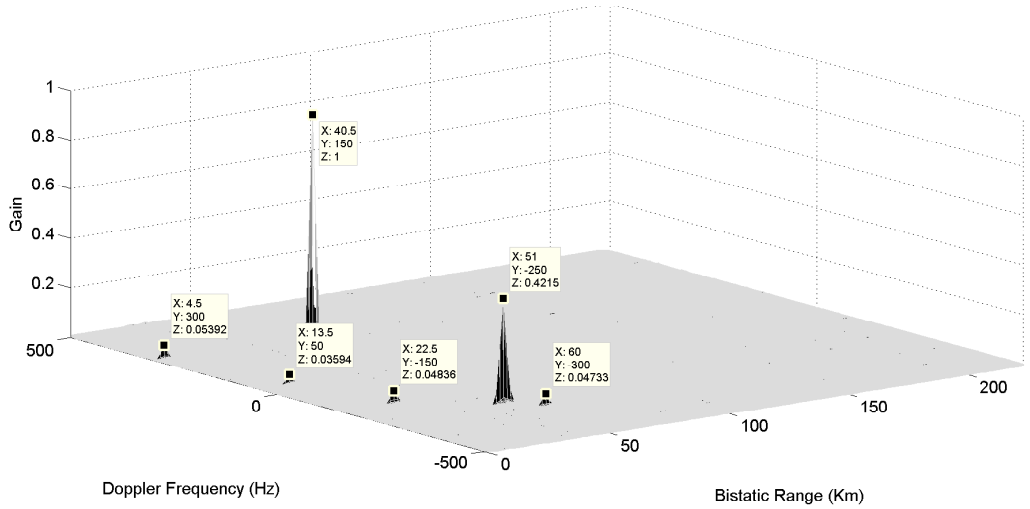

(a)

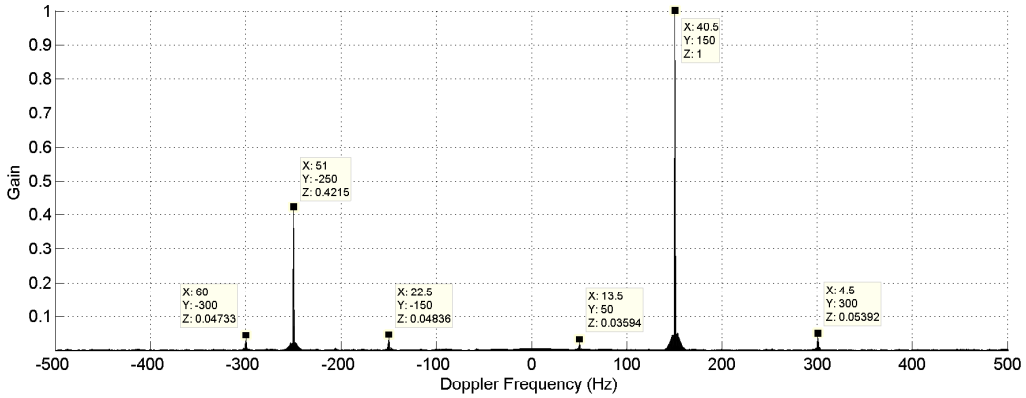

(b)

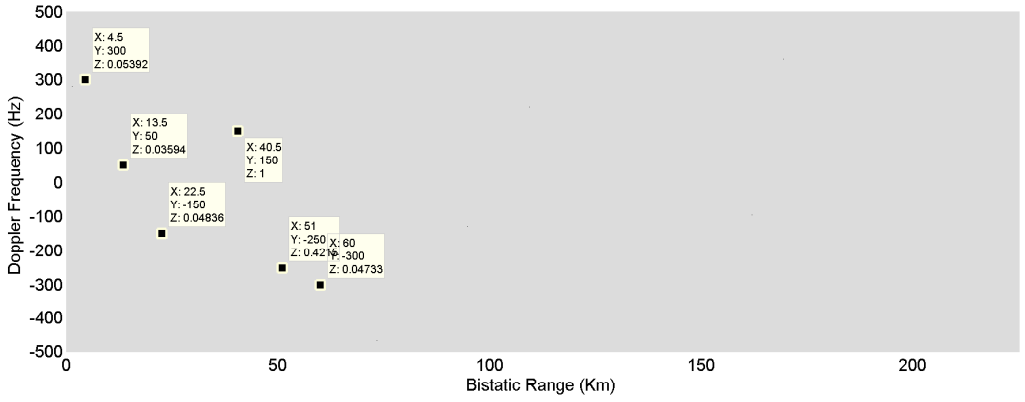

(c)

Figure 3.16: Simulation result for PES-ℓ_1: (a) 3D plot; (b) Doppler frequency plot; (c) view from the top.

3.5 Summary

In this section, compressive sensing based denoising and PES-ℓ_1 methods are introduced. After brief background information, BP, OMP, CoSaMP and IHT methods with different measurement values and sparsity levels are applied to the given CS problem. Results in terms of PSNR (dB), SNR (dB), time (sec.) and the number of the detected targets are given in a table and compared within a graph. In addition, some range-Doppler maps for $M = 40, 400, 1000, 2000, 4096$ of results given that table is plotted. It is shown that the proposed algorithm, PES-ℓ_1 mostly outperforms the other CS based denoising methods for many measurements and sparsity level estimations.

Chapter 4

New Correlation Algorithm For Passive Radar Target Detection

Specifying relationships between two variables has received a renewed interest in signal processing and science. There are many ways to do it. The most well-known function is the correlation coefficient and/or function. Correlation is a measure of similarity between two random variables or two sets of data. It refers any class of statistical relationships of two signals. If somebody wants to compare correlation between two signals or variables, *correlation coefficients* determine how much they effect each other. There are many numerous correlation algorithms used in signal processing applications [53–58]. One of the applications is matched filtering. The matched filter is obtained by correlating two signals. One of these signals is a known signal and the second one is an unknown signal. We know that the radar AF represents the output of the matched filter and it describes the two dimensional range-Doppler plane of the target as described in Section 2.4. AF calculated at $(l, p) = (0, 0)$ is equal to matched filter output, which means that the reference signal matches perfectly to the surveillance signal. When time delay and Doppler shift are added to the reference signal, that signal differs from the surveillance signal. In this section, various correlation algorithms between the surveillance signal and the time delayed and frequency shifted replica of the reference signal are studied.

4.1 Algorithms for Comparing Correlation of Two Signals

In this section, some correlation algorithms, such as maximal information coefficients (MIC) [55, 56], Pearson [57], Spearman [58] and a new method based on the least squares of the bistatic surveillance and reference data are introduced and applied to the PBR system.

Let us define two signals $\mathbf{s}_x$ and $\mathbf{s}_y$ from the surveillance signal and the reference signal as follows:

$$\begin{aligned} \mathbf{s}_y[n] &= s_{surv}[n], \\ \mathbf{s}_{x,(l,p)}[n] &= s^*_{ref}[n-l]e^{-j2\pi pn/N}, \end{aligned} \tag{4.1}$$

respectively. In Eq. 4.1, N is the number of the samples, l is the bistatic range bin and p is the Doppler bin. We can simply calculate the correlation between $\mathbf{s}_{x,(l,p)}[n]$ and $\mathbf{s}_y[n]$ to determine targets. When there is a target at a specific (l^*, p^*) pair, the correlation should be high compared to other (l, p) values. As can be understood from Eq. 4.1, $\mathbf{s}_x$ and $\mathbf{s}_y$ signals are complex valued signals. The correlation between real parts, $\mathbf{s}^r_{x,(l,p)}[n], \mathbf{s}^r_y[n]$ and imaginary parts, $\mathbf{s}^i_{x,(l,p)}[n], \mathbf{s}^i_y[n]$ are processed separately and the magnitude of real and imaginary correlations are combined:

$$\xi[l,p] = \sqrt{r^2_r(\mathbf{s}_{x,(l,p)}, \mathbf{s}_y) + r^2_i(\mathbf{s}_{x,(l,p)}, \mathbf{s}_y)} \tag{4.2}$$

where $r_r(\mathbf{s}_{x,(l,p)}, \mathbf{s}_y)$ is the correlation result of $\mathbf{s}^r_{x,(l,p)}[n], \mathbf{s}^r_y[n]$ values and $r_i(\mathbf{s}_{x,(l,p)}, \mathbf{s}_y)$ is the correlation result of $\mathbf{s}^i_{x,(l,p)}[n], \mathbf{s}^i_y[n]$ obtained using some correlation algorithms.

4.1.1 Maximal Information Coefficient (MIC)

Maximal information coefficients (MIC) is a recently introduced measure of the relationship between two variables $\mathbf{s}_x$ and $\mathbf{s}_y$. MIC is based on mutual information and data binning. Data binning is applied to reduce the small valued

observations of effects in correlation computation. Original data values falling into a small interval, called a bin, can be changed by an another value representing the interval. Data binning is a form of quantization. Mutual information is defined in probability and information theory and tries to find a measure of mutual dependence of variables. The idea behind the MIC algorithm is that both signals are divided into bins and these bins should be chosen in such a way that the mutual information between the two signals are maximized [59]. The mutual information of two discrete signals, $\mathbf{s}_x$ and $\mathbf{s}_y$ is given by

$$I(\mathbf{s}_x, \mathbf{s}_y) = \sum_{y \in \mathbf{s}_y} \sum_{x \in \mathbf{s}_x} p(x, y) \log \Big(\frac{p(x, y)}{p(x)p(y)} \Big) \tag{4.3}$$

where $p(x, y)$ is the joint probability distribution function of x and y and $p(x)$ and $p(y)$ are the marginal probability distribution functions of x and y, respectively. The following condition of maximal information coefficients should be satisfied:

$$H(s_x) = H(s_y) = H(s_x, s_y) \tag{4.4}$$

where $H(\mathbf{s}_x)$ and $H(\mathbf{s}_y)$ are marginal entropies and $H(\mathbf{s}_x, \mathbf{s}_y)$ is the joint entropy.

The MIC algorithm uses real numbered variables, so our technique mentioned in Section 4.1 can work properly because complex numbers are divided into real and imaginary parts. Moreover, the product of the number of bins for $\mathbf{s}_x$ and $\mathbf{s}_y$ is selected smaller than the size $N^{0.6}$ to prevent the trivial dividing in [59] as follows:

$$n_{\mathbf{s}_x} \times n_{\mathbf{s}_y} \leq N^{0.6} \tag{4.5}$$

where N is the size of signals. After calculating the maximal mutual information, MIC algorithm normalizes the scores between 0 and 1 and the highest normalized mutual information obtained by any x-by-y grid can be denoted as $r(\mathbf{s}_x, \mathbf{s}_y)$.

4.1.2 Pearson Correlation Coefficient

Pearson correlation coefficient is also measure of the relationship between two variables $\mathbf{s}_x$ and $\mathbf{s}_y$. It is defined as the covariance of two variables divided by multiplication of their standard deviations. Simply, the Pearson correlation coefficient is calculated as follows:

$$r(\mathbf{s}_x, \mathbf{s}_y) = \frac{cov(\mathbf{s}_x, \mathbf{s}_y)}{\sigma_{\mathbf{s}_x}\sigma_{\mathbf{s}_y}} \tag{4.6}$$

where $cov(.)$ denotes the covariance, $\sigma_{\mathbf{s}_x}$ is the standard deviation of $\mathbf{s}_x$. This algorithm produces normalized values between -1 and +1.

4.1.3 Spearman's Rank Correlation Coefficient

Spearman's rank correlation coefficient is a statistical dependence measure between two variables. This method is similar to the Pearson correlation coefficient method. The difference is to use ranked variables instead of the original variables. Spearman's rank correlation coefficient is calculated as follows:

$$r(\mathbf{s}_x, \mathbf{s}_y) = \frac{6\sum_{i=1}^{n} d_i^2}{n(n^2-1)} \tag{4.7}$$

where d_i is the difference ranks of $\mathbf{s}_x$ and $\mathbf{s}_y$ variables positioned in the ascending order. Here is an example. Let us assume that we observe two vectors $\mathbf{s}_x = [0.6,\ 1.4\ , 1.4,\ 2.5]$ and $\mathbf{s}_y = [0.2,\ 0.5\ , 0.8,\ 5]$. The positions of $\mathbf{s}_x$ and $\mathbf{s}_y$ in the ascending order is given by $[1,\ 2,\ 3,\ 4]$, then the ranks of $\mathbf{s}_x$ and $\mathbf{s}_y$ can be calculated by $[1,\ 2.5,\ 2.5,\ 4]$ and $[1,\ 2,\ 3,\ 4]$, respectively. Then, if there are same variables in a vector, ranks of them are averaged for both of them. Other ranks will be the same. The difference between ranks are $d_{1,2,3,4} = [0,\ 1.5, 1.5\ 0]$. The result of this correlation between $\mathbf{s}_x$ and $\mathbf{s}_y$: $r(\mathbf{s}_x, \mathbf{s}_y) = \frac{6\times 4.5}{4(16-1)} = 0.45$. The output of this algorithm $r(\mathbf{s}_x, \mathbf{s}_y)$ is normalized between -1 and +1.

4.1.4 Cross-term Free Least Squares (CLS) Method

In this method, our aim is to compare correlation between signals $\mathbf{s}_x$ and $\mathbf{s}_y$ by using least squares method. In standard least squares approach the following distance problem is minimized:

$$\text{MSE}(l,p) = \sum_n (s_{surv}[n] - a_{l,p} s^*_{ref}[n-l] e^{-j2\pi pn/N})^2 \tag{4.8}$$

Whenever there is a target at specific *(l,p)* pair, the magnitude $|a_{l,p}|$ of $a_{l,p}$ becomes significantly larger than the other *(l,p)* pairs. Actually, the solution of the above LS minimization is the same as AF approach. This can be easily proved as follows: The least squares solution corresponds to the solution of

$$\mathbf{s}_y = a_{l,p} \mathbf{s}_{x,(l,p)} \tag{4.9}$$

where $\mathbf{s}_{x,(l,p)}[n] = \mathbf{s}^*_{ref}[n-l] e^{-j2\pi pn/N}$ and $\mathbf{s}_y[n] = \mathbf{s}_{surv}[n]$. Therefore,

$$a^*_{l,p} = \frac{\mathbf{s}^H_{x,(l,p)} \mathbf{s}_y}{\| \mathbf{s}_y \|^2}, \tag{4.10}$$

where $a^*_{l,p}$ is the optimal value. Obviously, the numerator of Eq. 4.10 is the AF function or the matched filter solution expressing the correlation between $\mathbf{s}_{x,(l,p)}$ and $\mathbf{s}_y$ vectors. However, this suffers from cross-terms when a multichannel FM based PBR system is used.

We heuristically solve two least squares problems separating the real and imaginary parts of the original LS problem 4.8:

$$\min_{a_1} \| \mathbf{s}^r_y - a_{1,(l,p)} \mathbf{s}^r_{x,(l,p)} \|^2 \tag{4.11}$$

and

$$\min_{b_1} \| \mathbf{s}^i_y - b_{1,(l,p)} \mathbf{s}^i_{x,(l,p)} \|^2, \tag{4.12}$$

where $\mathbf{s}^r_{x,(l,p)}$, $\mathbf{s}^i_{x,(l,p)}$ and $\mathbf{s}^r_y$, $\mathbf{s}^i_y$ are real and imaginary parts of $\mathbf{s}_{x,(l,p)}$ and $\mathbf{s}_y$, respectively. Our heuristic approach is based on the idea that 4.11 and 4.12

do not contain any cross-terms. We can minimize 4.11 and 4.12 using `CVX` or `polyfit` functions of MATLAB. We define the Cross-term free Least Squares (CLS) as follows:

$$\mathrm{CLS}(l,p) = a^2_{1,(l,p)} + b^2_{1,(l,p)}, \tag{4.13}$$

where $a_{1,(l,p)}$ and $b_{1,(l,p)}$ are optimal values for least squares problem.

Example scatter plots of $\mathbf{s}_{x,(l,p)}$ and $\mathbf{s}_y$ with target/no target scenarios are shown in Figure 4.1. In Figures 4.1(a) and 4.1(b), the scatter plots with a target are shown. In Figures 4.1(c) and 4.1(d), scatter plots without a target are shown. As can be seen, it is not possible to visually distinguish these plots, but the CLS coefficients for no target case are 0.0086 and 0.0107, respectively. In contrast, the CLS coefficients are 1.34 and 1.32, respectively when there is a target.

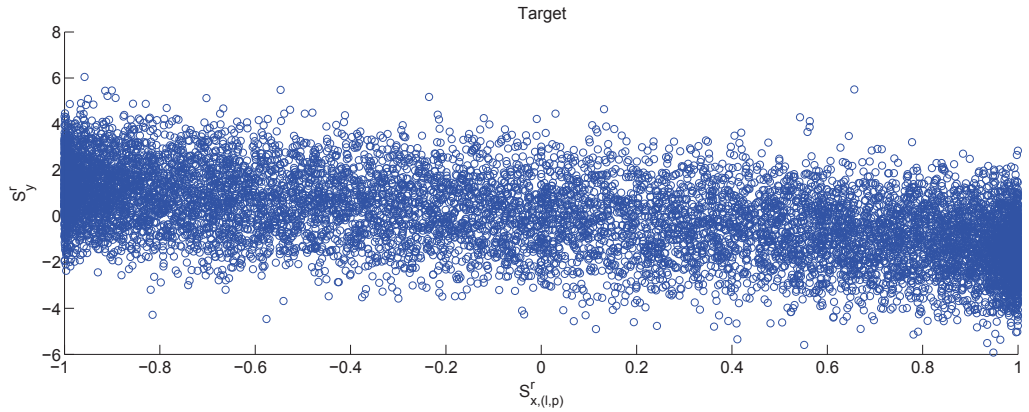

(a)

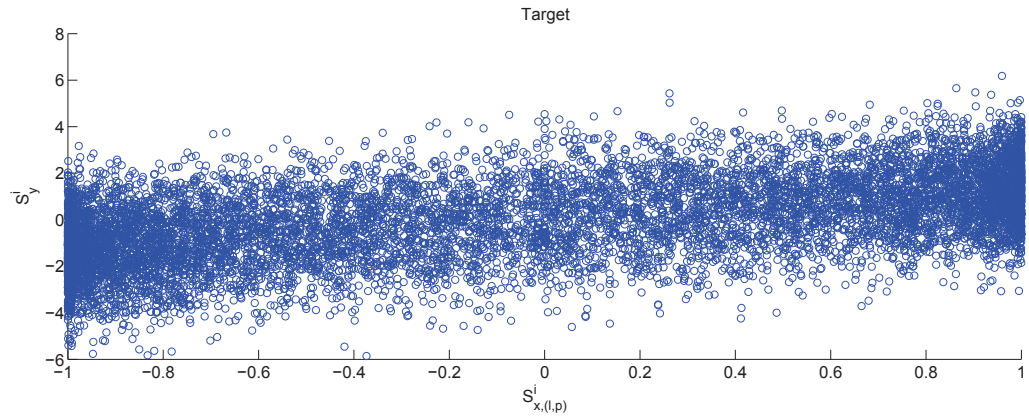

(b)

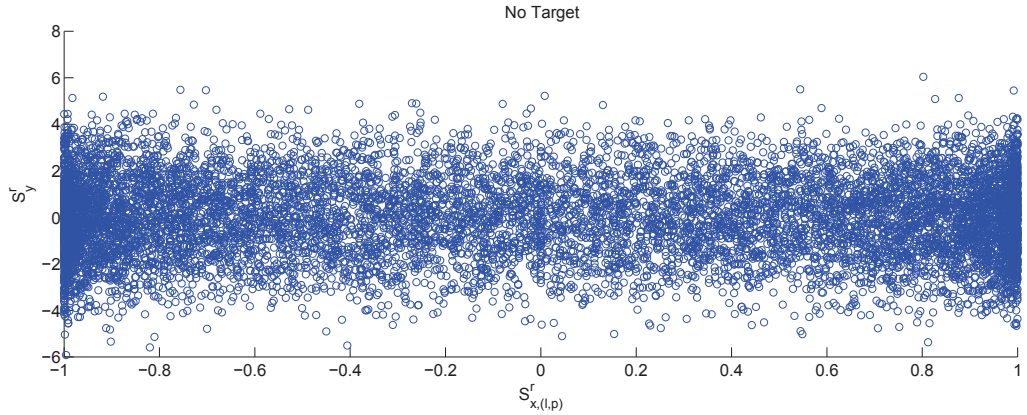

(c)

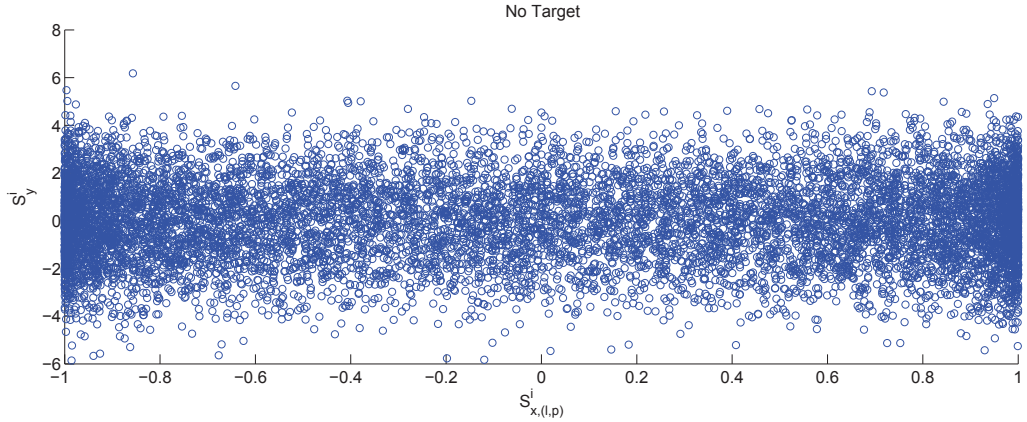

(d)

Figure 4.1: Scatter plots of $\mathbf{s}_{x,(l,p)}$ and $\mathbf{s}_y$ for a target with: (a) real parts (CLS=1.34); (b) imaginary parts (CLS=1.32); (c) real parts (CLS=0.0086); (d) imaginary parts (CLS=0.0107) of $\mathbf{s}_{x,(l,p)}$ and $\mathbf{s}_y$ with no target.

4.2 Simulation Results

This section presents the simulation results of each method mentioned above. Because of the long time problem and high cost in MATLAB simulation program, a new passive radar system scenario is generated as shown in Table 4.1. Sampling frequency and integration time are $f_s = 2 \times 10^5$ Hz and 1 sec., respectively, so we can get signals with 2×10^5 size. However, it takes too much time for the simulation results. For this reason, a signal portion in 1×10^4 size is taken and

used in our simulations. There are 3 targets and 6 clutters in this scenario. AF is calculated according to these specifications and shown in Figure 4.2. Normal procedure is performed with lms adaptive filter for all calculations. As can be seen in Figure 4.2(b), the range-Doppler map turns out to be noisy. With the following algorithms, targets are detected and noise level are decreased.

Table 4.1: System specifications for 3 targets.

	Target 1	Target 2	Target 3
Bistatic Range (Km)	40,65	51,63	14,14
Doppler Frequency (Hz)	300	-300	-100
Gain (dB)	4,1	-3,8	-7,5

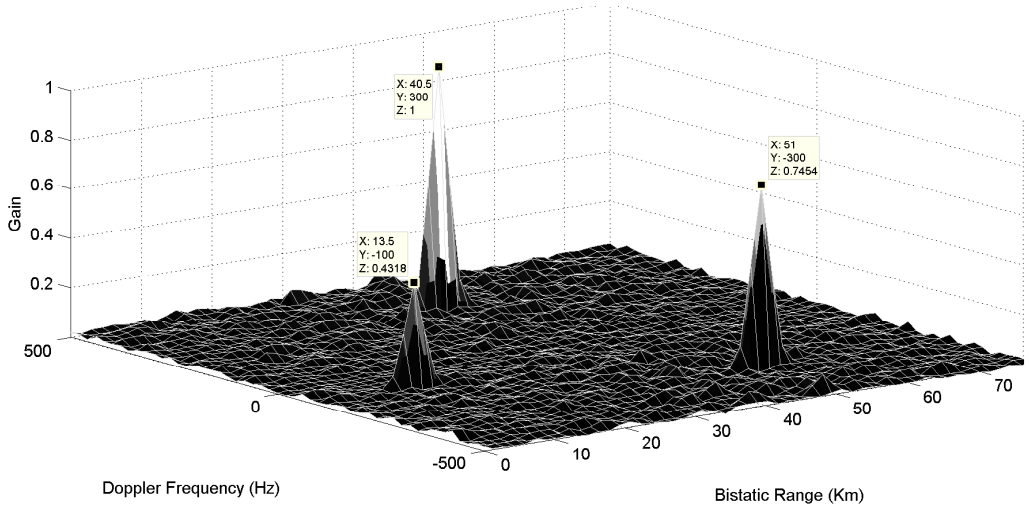

(a)

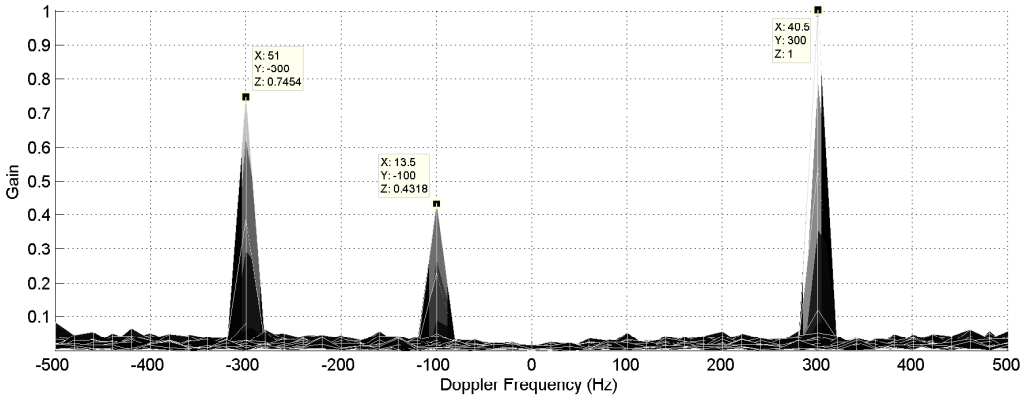

(b)

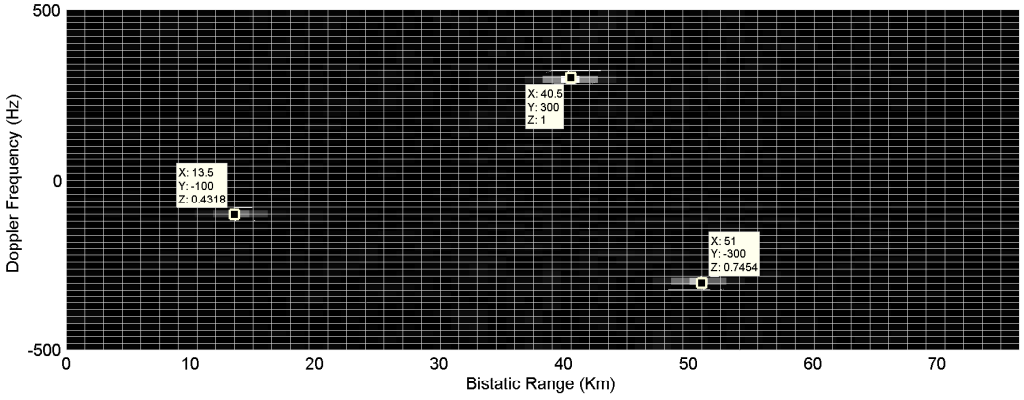

(c)

Figure 4.2: Illustration of three targets according to system scenario (4.1): (a) 3D plot; (b) Doppler frequency plot; (c) view from the top.

In Figures 4.3, 4.4, 4.5 and 4.6, the PBR system scenario with 3 targets and 6 clutters is implemented with MIC, Pearson, Spearman and cross-term free least squares methods, respectively. PSNR and SNR values are calculated to compare which method gives the more successful results and these values are listed in Table 4.2. Moreover, "FFT" means normal FFT based AF result with noise shown in Figure 4.2. As can be seen figures and the table, the best result occurs with the CLS method. Noise level is reduced as compared to FFT based method and targets are detected correctly with the MIC and proposed method. PSNR and SNR values for Pearson and Spearman algorithms are below the normal FFT based method. In addition, the running time for CLS method took 1136.8 sec. This shows the computational cost of CLS method is high even if it outperforms other correlation algorithms.

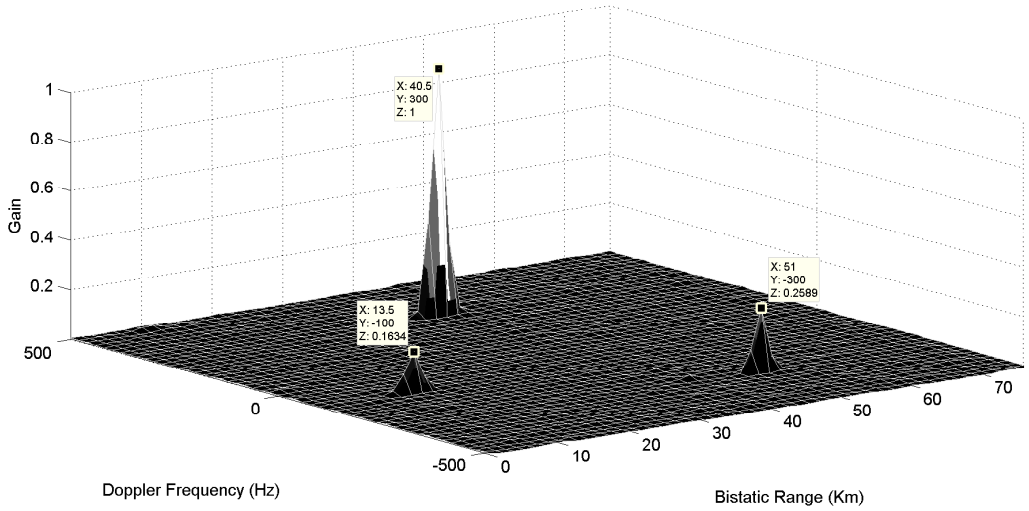

(a)

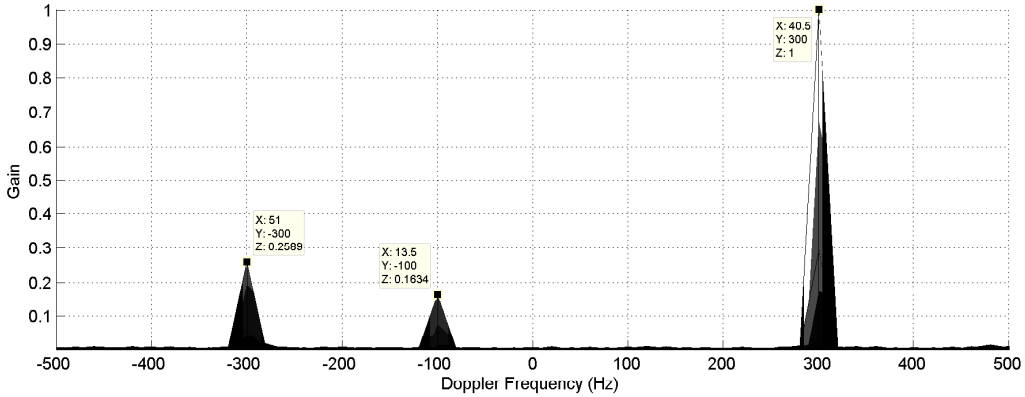

(b)

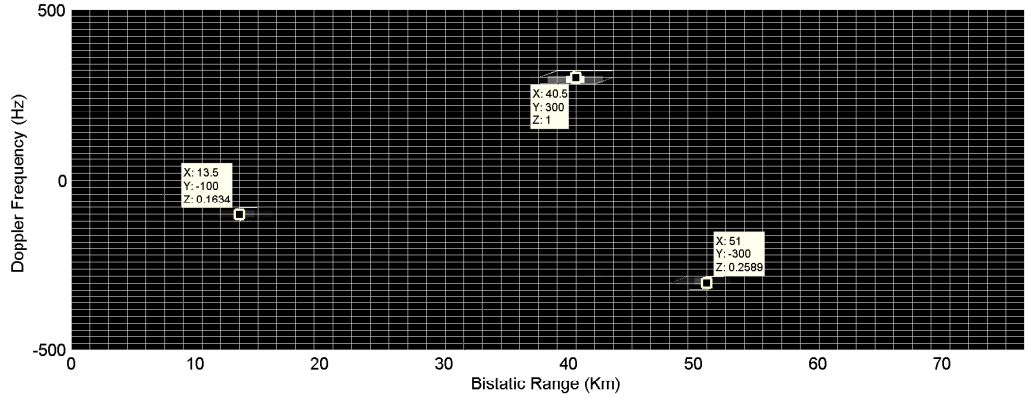

(c)

Figure 4.3: Simulation result for maximal information coefficient (MIC): (a) 3D plot; (b) Doppler frequency plot; (c) view from the top.

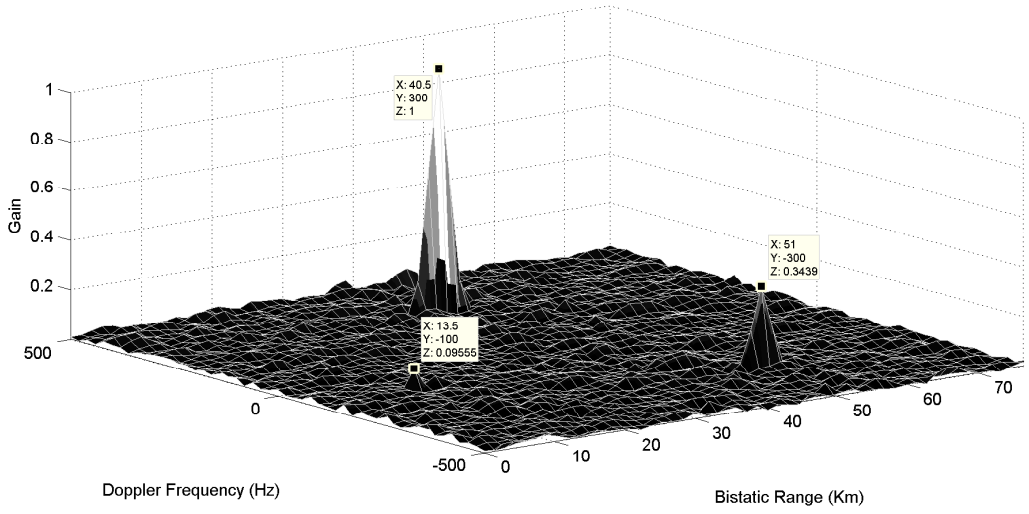

(a)

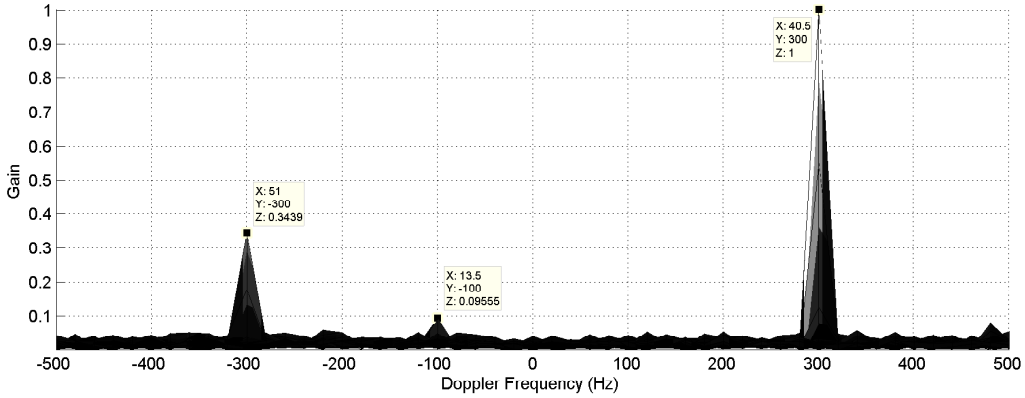

(b)

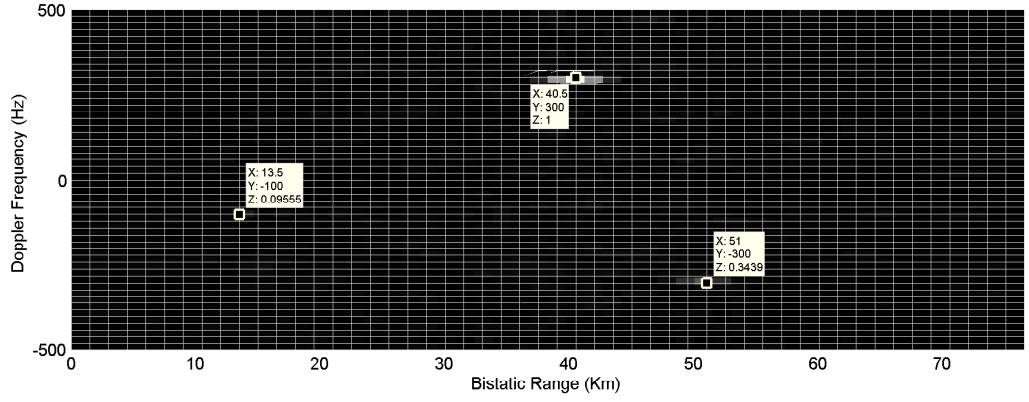

(c)

Figure 4.4: Simulation result for Pearson correlation coefficient: (a) 3D plot; (b) Doppler frequency plot; (c) view from the top.

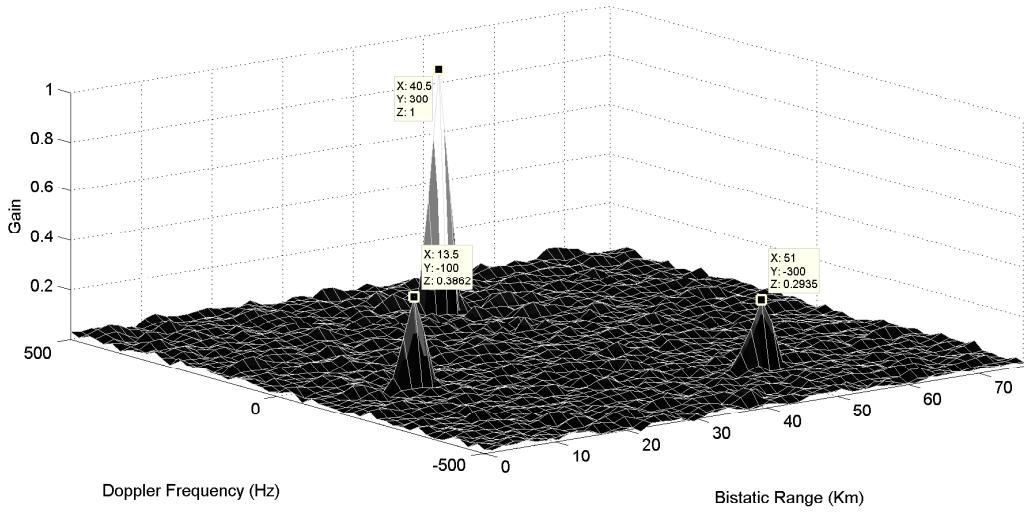

(a)

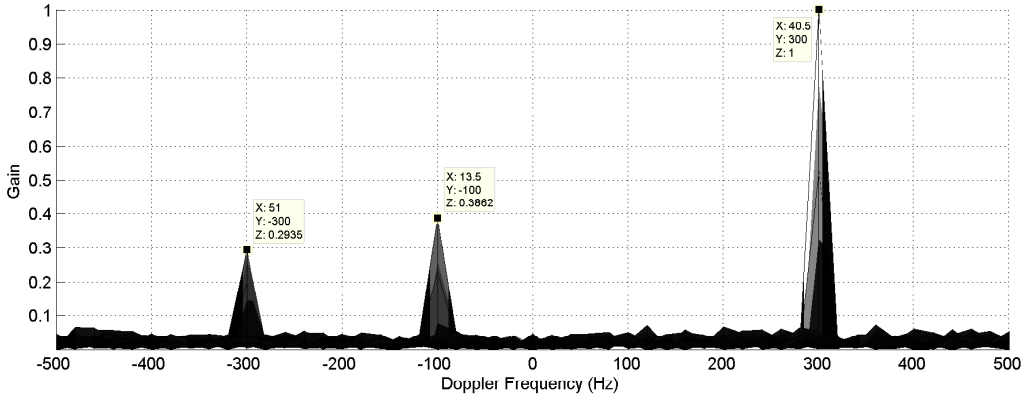

(b)

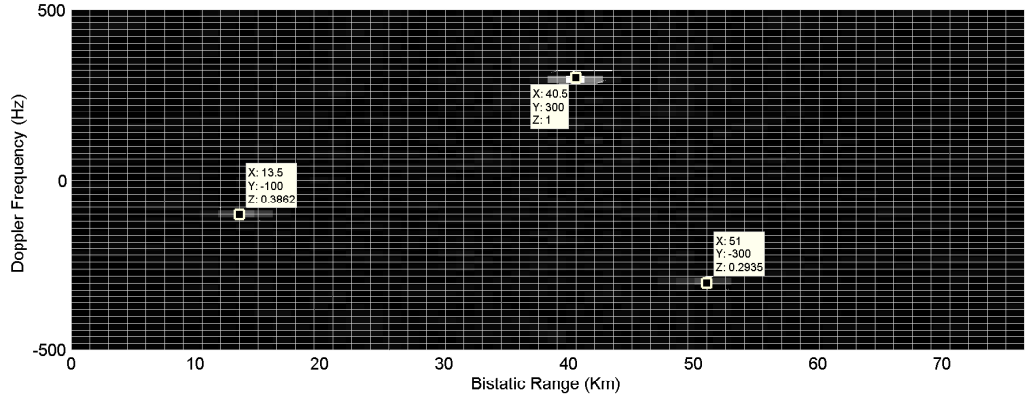

(c)

Figure 4.5: Simulation result for Spearman's rank correlation coefficient: (a) 3D plot; (b) Doppler frequency plot; (c) view from the top.

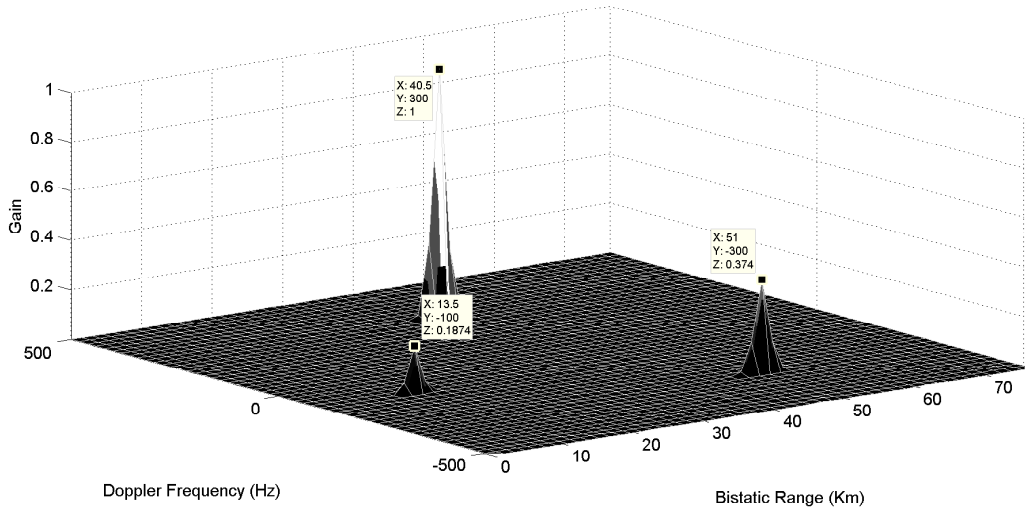

(a)

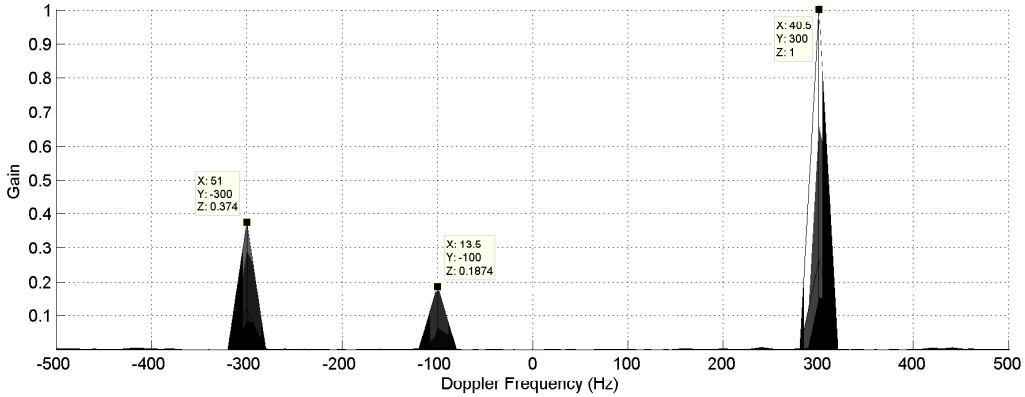

(b)

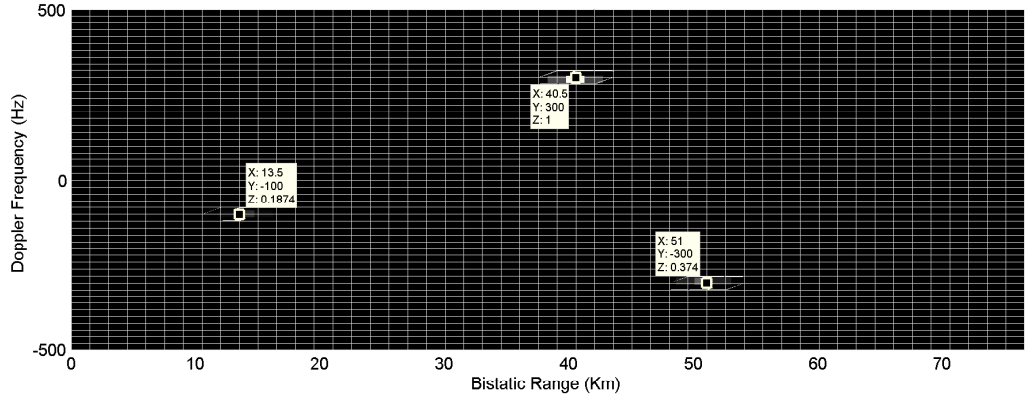

(c)

Figure 4.6: Simulation result for CLS method: (a) 3D plot; (b) Doppler frequency plot; (c) view from the top.

Table 4.2: PSNR and SNR values of results.

	PSNR (dB)	SNR (dB)
Maximal information coefficient (MIC)	35,14	5,57
Pearson correlation coefficient	31,74	2,08
Spearman's rank correlation coefficient	30,89	1,22
Cross-term free Least Squares method	36,08	6,54
FFT	33,39	3,76

In Figure 4.7, range-Doppler maps are thresholded within the range of 0 and 1 and plotted versus true detection rate. By doing this, we can learn which method has the best true detection rate versus a threshold. If we analysis this graph, the red line reaches the maximum rate quickly. As the threshold increases, true detection rate converges the maximum rate for all of them because we know that four methods detect three targets clearly at a threshold. As a result by looking at this data, the CLS proposed method outperforms other correlation methods.

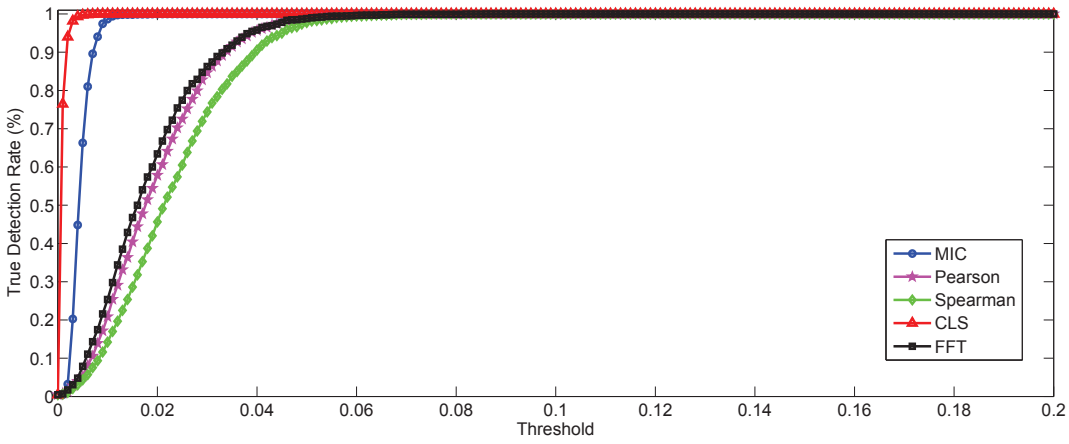

Figure 4.7: True detection rate vs. threshold graph for correlation methods.

In addition, we also aim to solve another problem by using correlation methods for radar target detection. It is possible to see targets with the same Doppler frequency and close bistatic ranges, so the problem is to detect and track close targets on the displaying screen. Let us assume a system scenario shown in Table 4.3 for two close targets and the range-Doppler map is plotted for AF in Figure

4.8. As can be seen, targets are not detected separately. This can cause the tracking problem in real-life work. For this purpose, CLS method is posed to detect targets. Simulation result of close targets for CLS method is shown in Figure 4.9. However, two targets can not be detected using the CLS method as can be observed. The other correlation methods are performed on this scenario and two targets can not be still detected.

In [60], multiple FM radio channels are used to increase the range resolution. Instead of using one FM channel, multiple FM radio channels are proposed to get better resolution for close targets. If we implement the multiple FM channels on our scenario, we can detect close two targets shown in Figure 4.10. Multiple FM channels consists of three channels which broadcasts pop music, rock music and human speaking, respectively. Each channel has a bandwidth of 100 kHz and there are dedicated spaces with 50 kHz between channels. Therefore, total bandwidth of these channels is 400 kHz. However, there can be many sidelobes and still cause some problems, so we apply CLS method on multiple FM channels based PBR system. Again, a signal portion is taken from reference and surveillance signals and used. The simulation result is given in Figure 4.11. It is obvious to understand that the number of sidelobes is decreased and close targets are detected clearly. Superious peaks are negligible compared to AF based close target scenario. In addition, some different scenario examples shown in Tables 4.4, 4.5 and 4.6 are also studied for two and three close targets. The detection examples are shown in Figures 4.13, 4.15 and 4.17, respectively.

Table 4.3: System specifications for two close targets in Figures 4.8, 4.9 4.10 and 4.11.

	Target 1	Target 2
Bistatic Range (Km)	4,875	6
Doppler Frequency (Hz)	40	40
Gain (dB)	-10	-5

Table 4.4: System specifications for two close targets in Figures 4.12 and 4.13.

	Target 1	Target 2
Bistatic Range (Km)	11,25	12,38
Doppler Frequency (Hz)	40	40
Gain (dB)	-10	-5

Table 4.5: System specifications for two close targets in Figures 4.14 and 4.15.

	Target 1	Target 2
Bistatic Range (Km)	19,50	20,63
Doppler Frequency (Hz)	80	80
Gain (dB)	-10	-10

Table 4.6: System specifications for three close targets in Figures 4.16 and 4.17.

	Target 1	Target 2	Target 3
Bistatic Range (Km)	19,50	20,63	21,75
Doppler Frequency (Hz)	96	96	96
Gain (dB)	-10	-10	-10

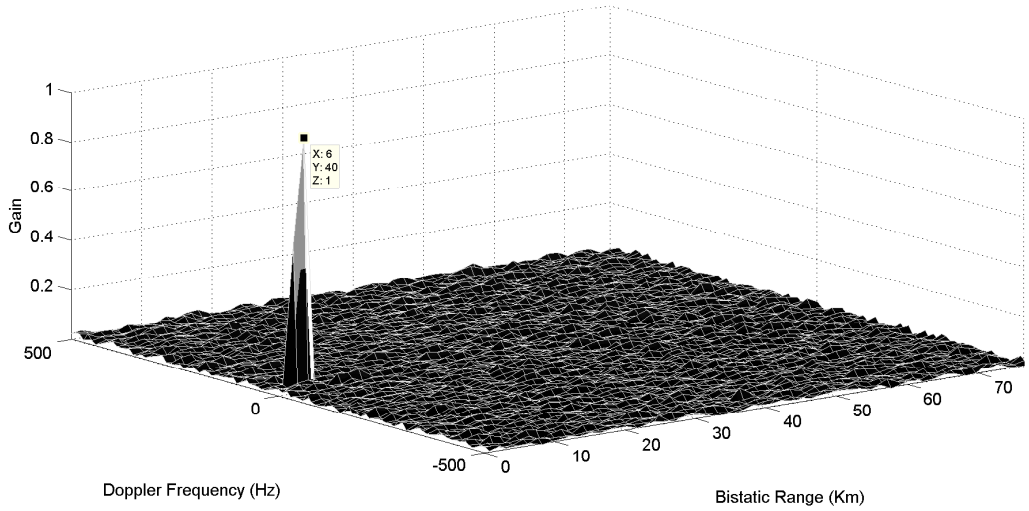

(a)

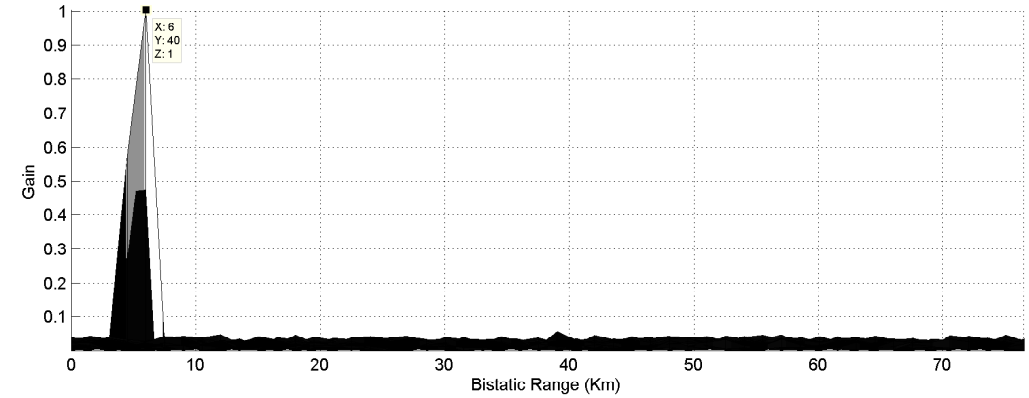

(b)

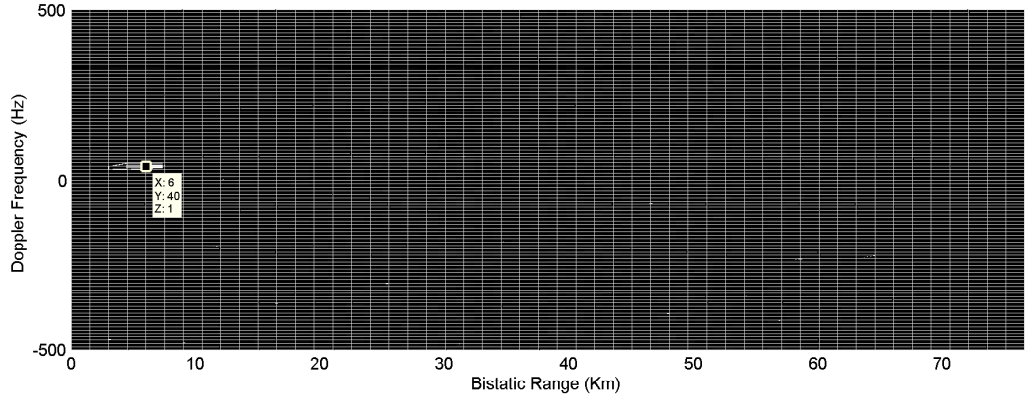

(c)

Figure 4.8: Simulation result of two close targets with $p_{(1,2)} = 40$ Hz, $l_1 = 4.875$ and $l_2 = 6$ km for normal AF: (a) 3D plot; (b) bistatic range plot; (c) view from the top.

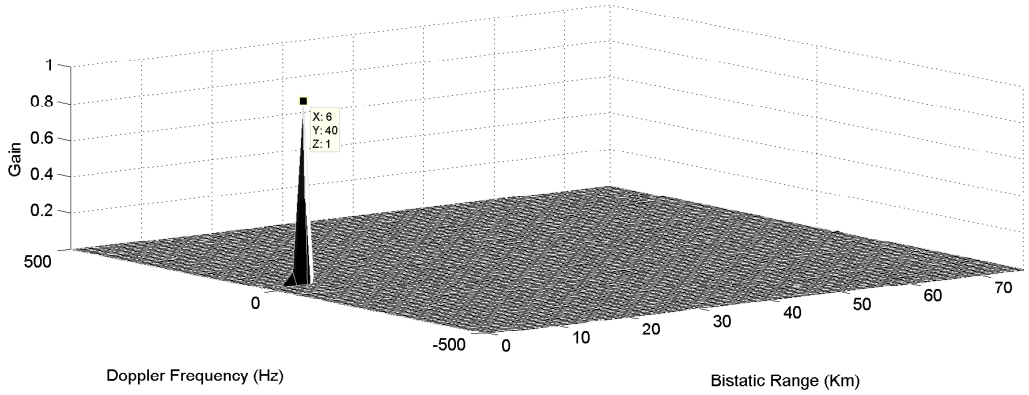

(a)

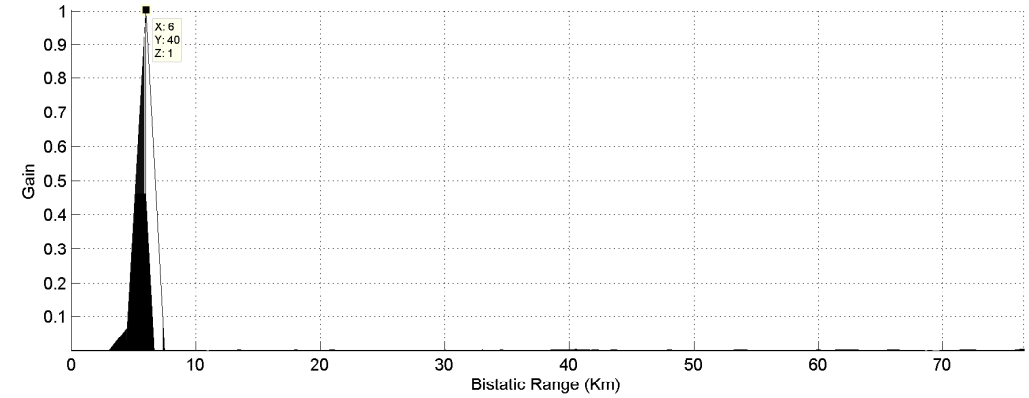

(b)

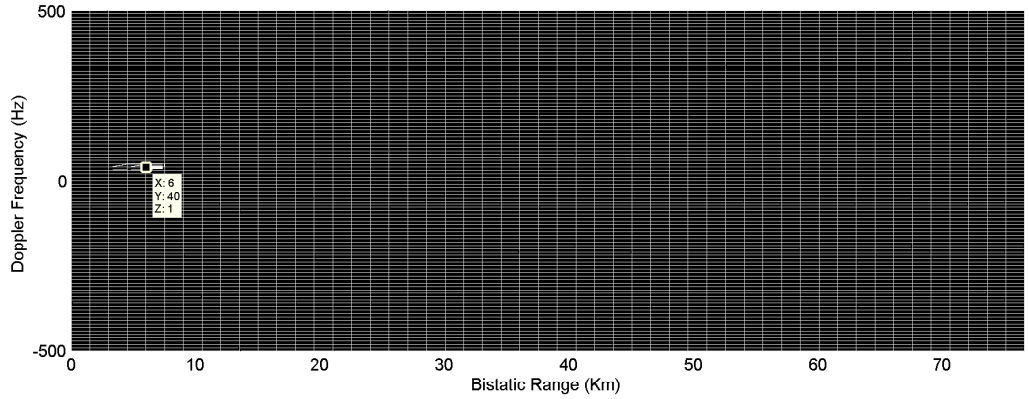

(c)

Figure 4.9: Simulation result of two close targets with $p_{(1,2)} = 40$ Hz, $l_1 = 4.875$ and $l_2 = 6$ km for CLS method: (a) 3D plot; (b) bistatic range plot; (c) view from the top.

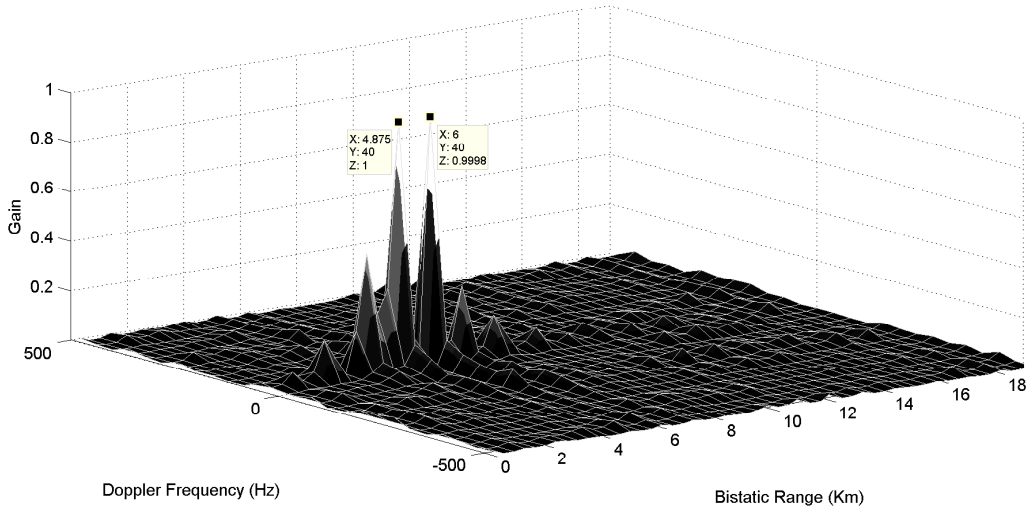

(a)

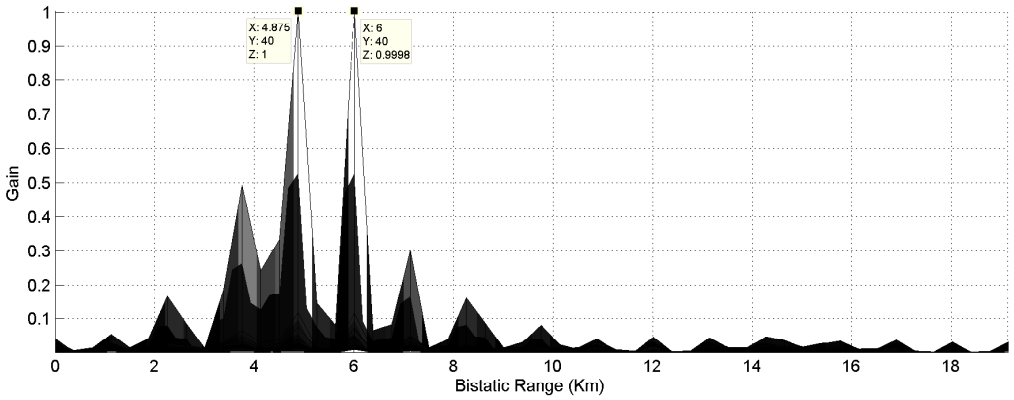

(b)

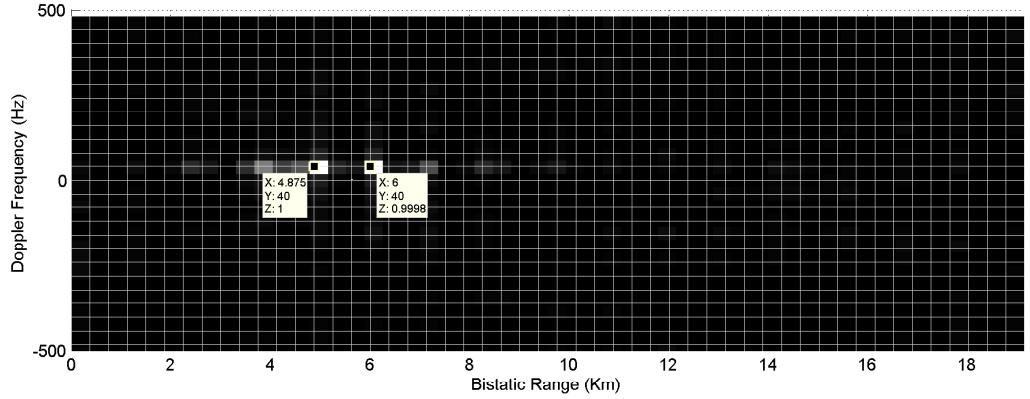

(c)

Figure 4.10: Simulation result of two close targets with $p_{(1,2)} = 40$ Hz, $l_1 = 4.875$ and $l_2 = 6$ km for multiple FM channels based normal AF: (a) 3D plot; (b) bistatic range plot; (c) view from the top.

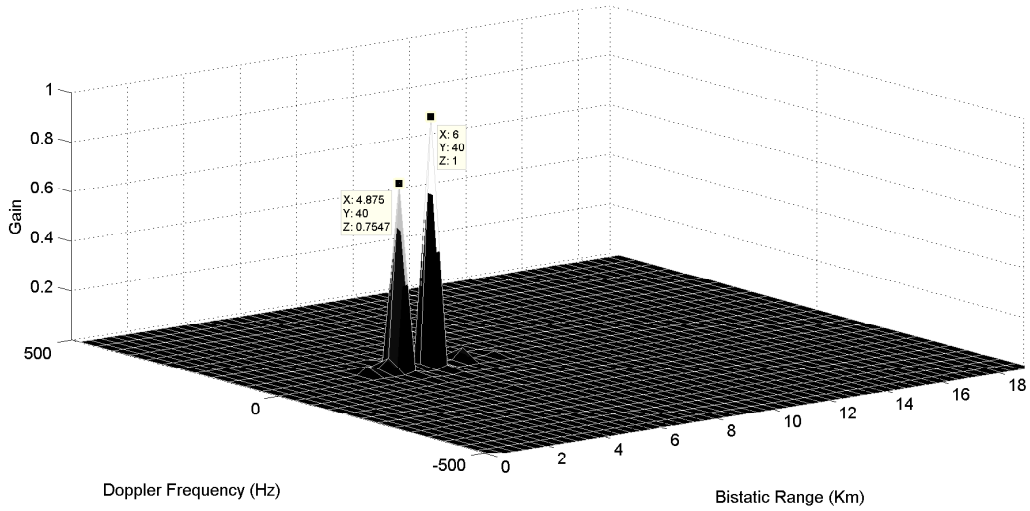

(a)

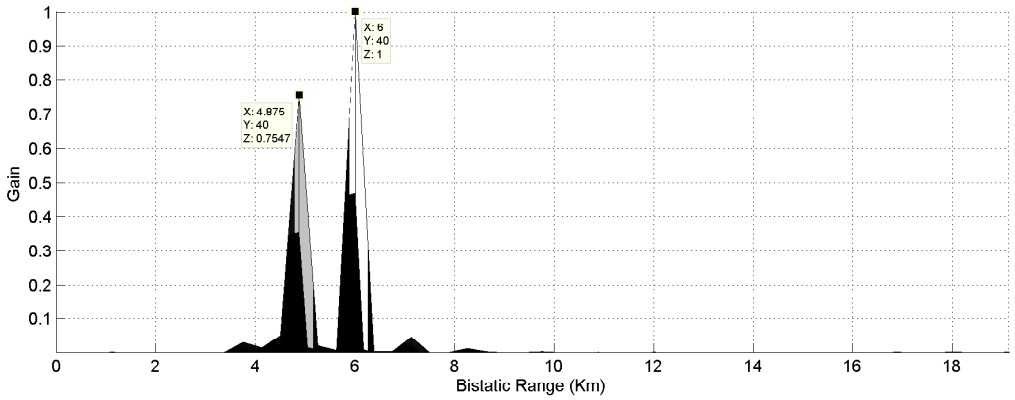

(b)

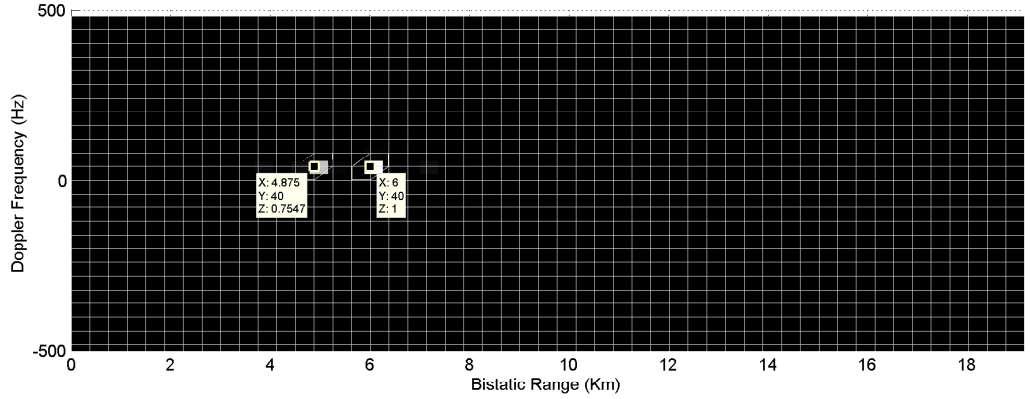

(c)

Figure 4.11: Simulation result of two close targets with $p_{(1,2)} = 40$ Hz, $l_1 = 4.875$ and $l_2 = 6$ km for multiple FM channels based CLS method: (a) 3D plot; (b) bistatic range plot; (c) view from the top.

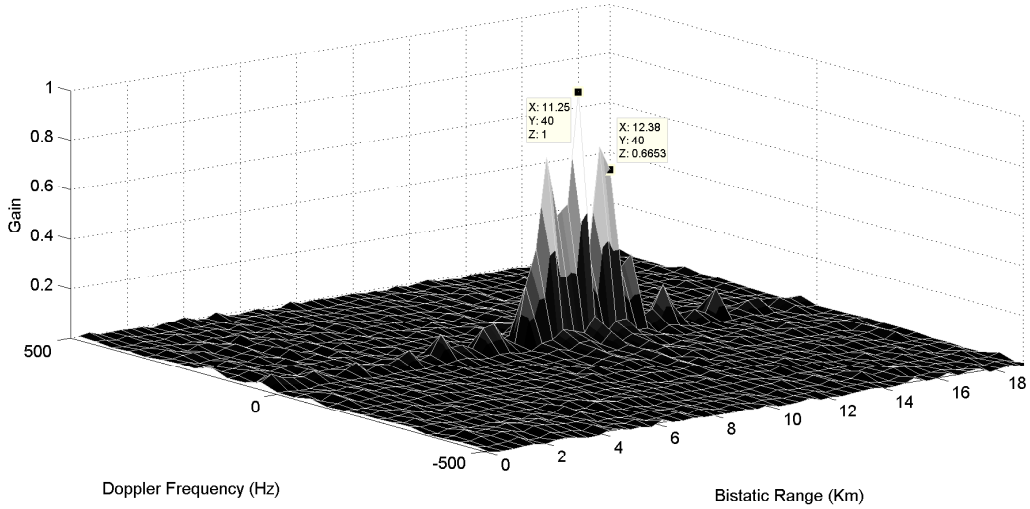

(a)

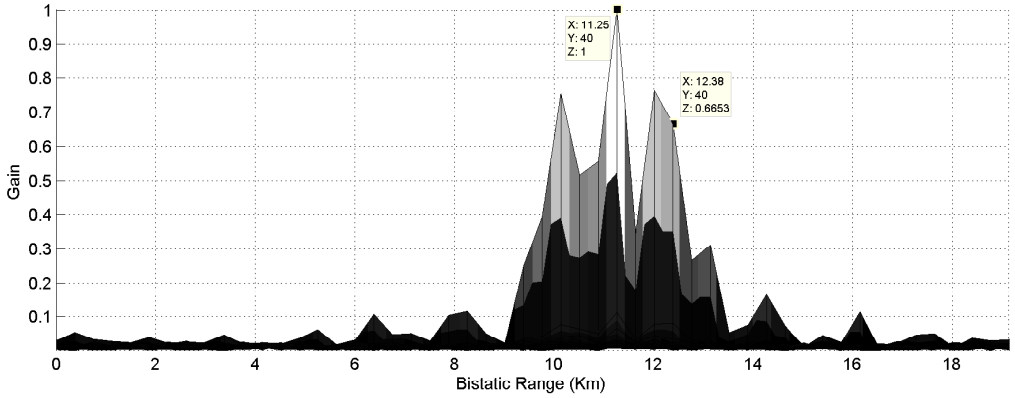

(b)

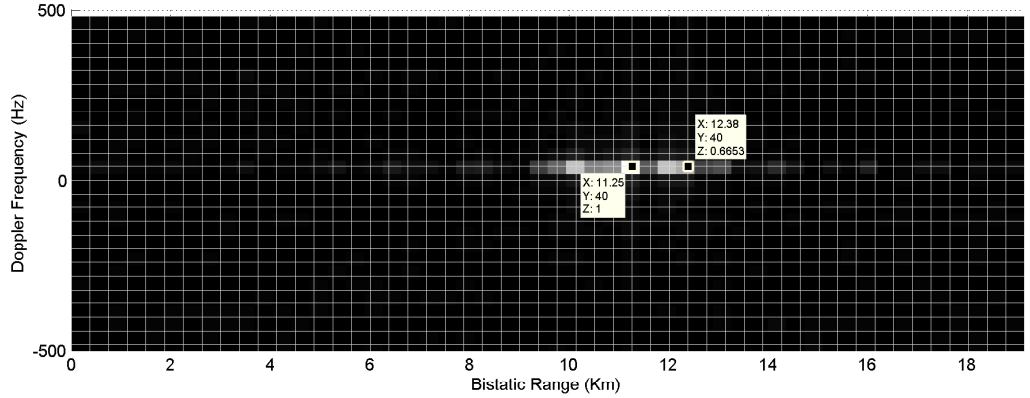

(c)

Figure 4.12: Simulation result of two close targets with $p_{(1,2)} = 40$ Hz, $l_1 = 11,25$ and $l_2 = 12,38$ km for multiple FM channels based normal AF: (a) 3D plot; (b) bistatic range plot; (c) view from the top.

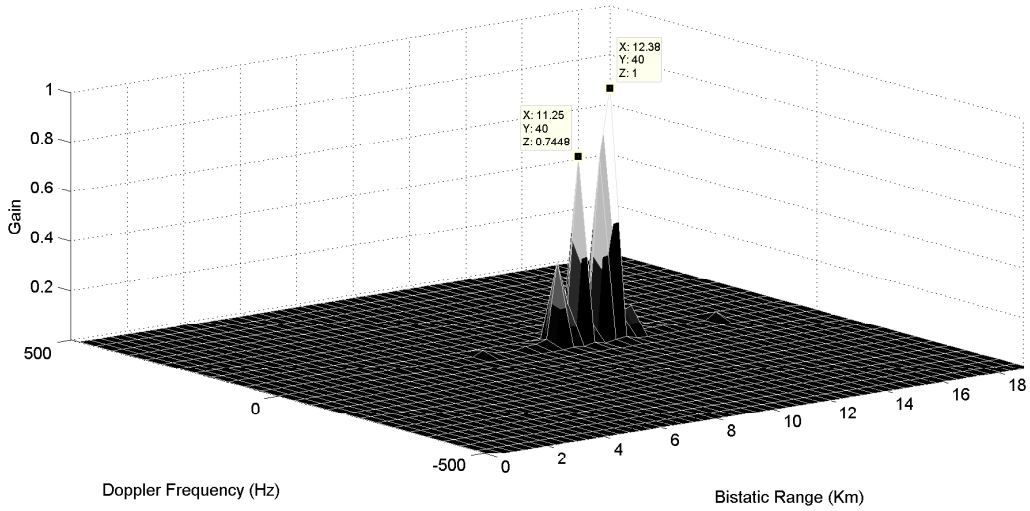

(a)

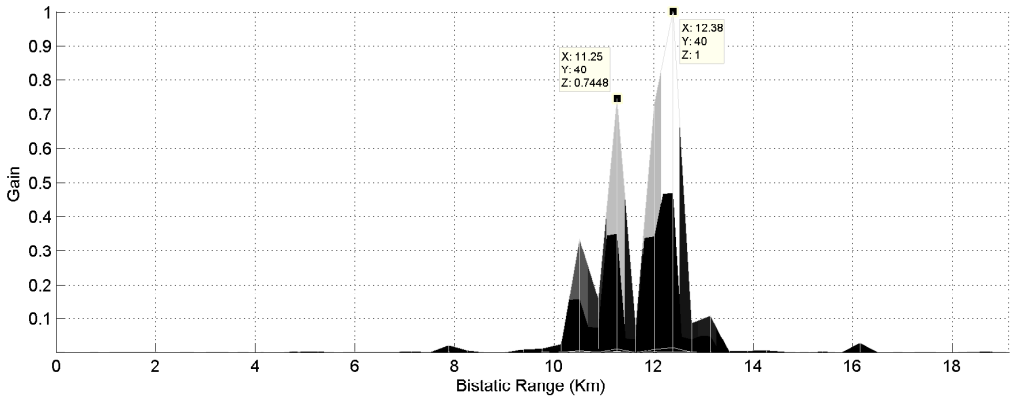

(b)

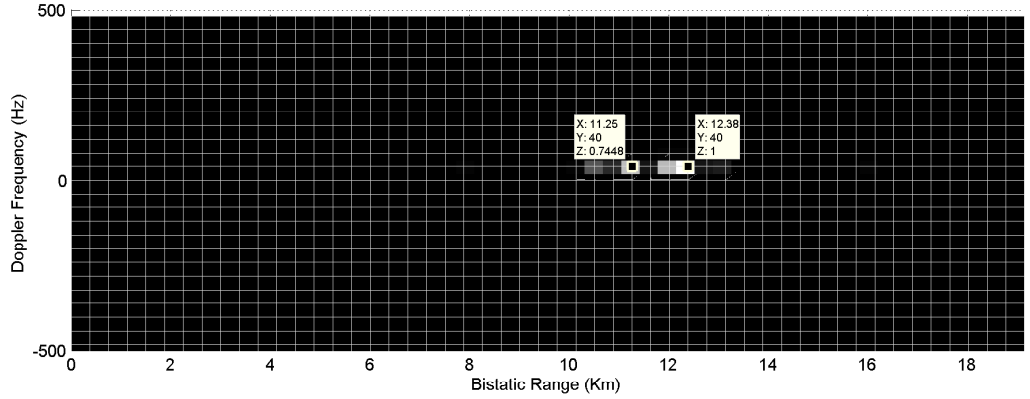

(c)

Figure 4.13: Simulation result of two close targets with $p_{(1,2)} = 40$ Hz, $l_1 = 11,25$ and $l_2 = 12,38$ km for multiple FM channels based CLS method: (a) 3D plot; (b) bistatic range plot; (c) view from the top.

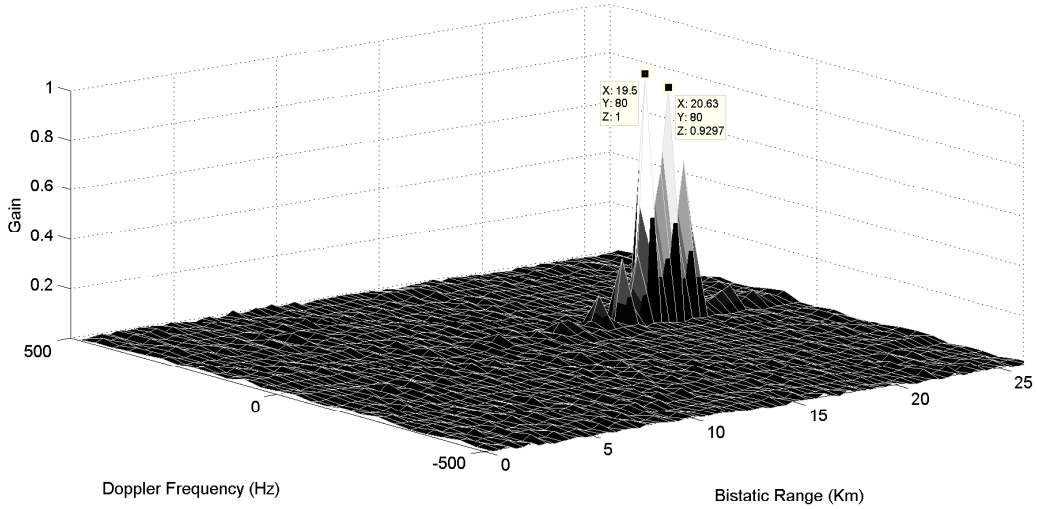

(a)

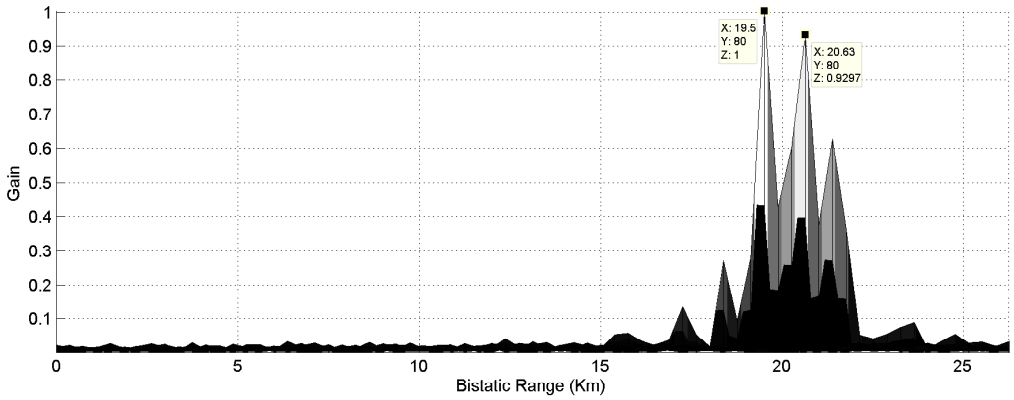

(b)

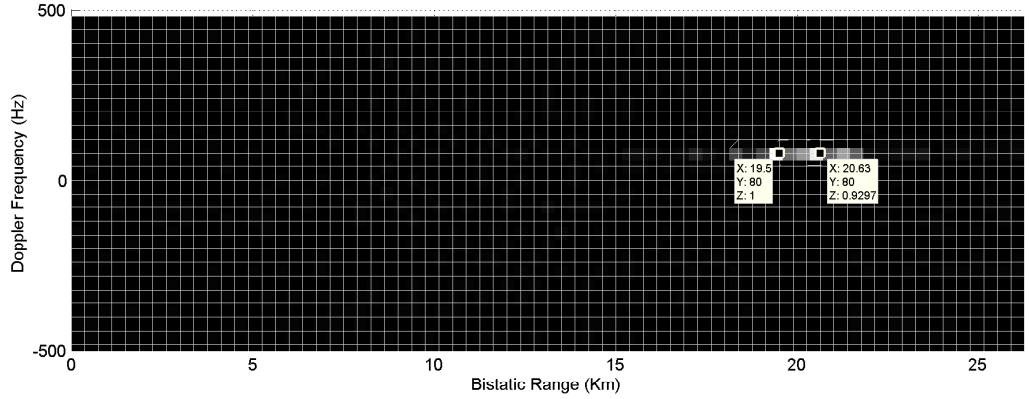

(c)

Figure 4.14: Simulation result of two close targets with $p_{(1,2)} = 80$ Hz, $l_1 = 19.5$ and $l_2 = 20,63$ km for multiple FM channels based normal AF: (a) 3D plot; (b) bistatic range plot; (c) view from the top.

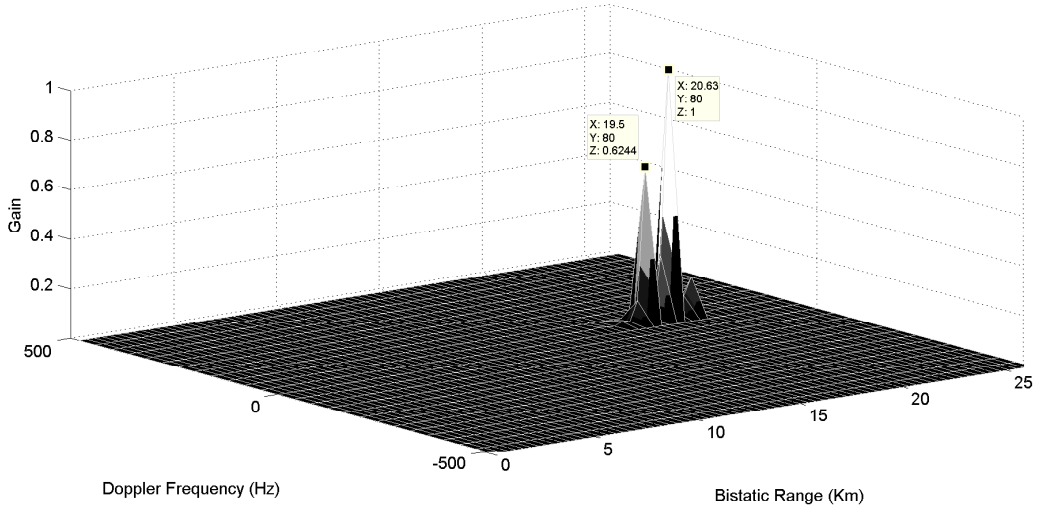

(a)

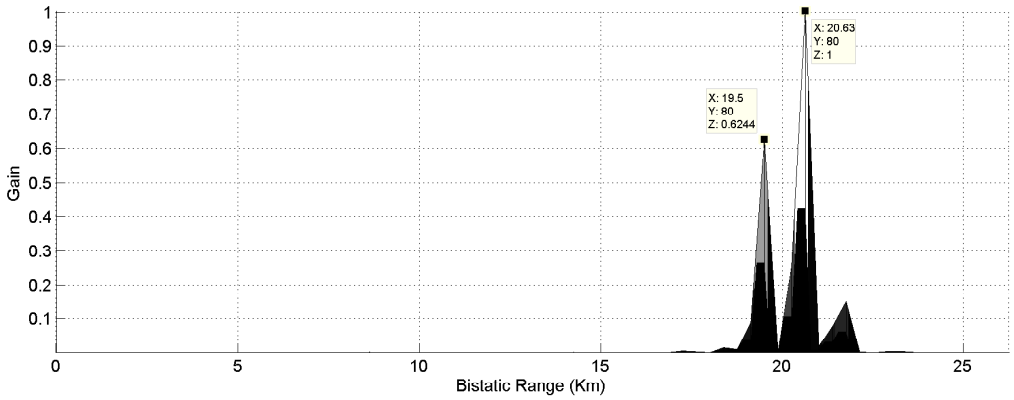

(b)

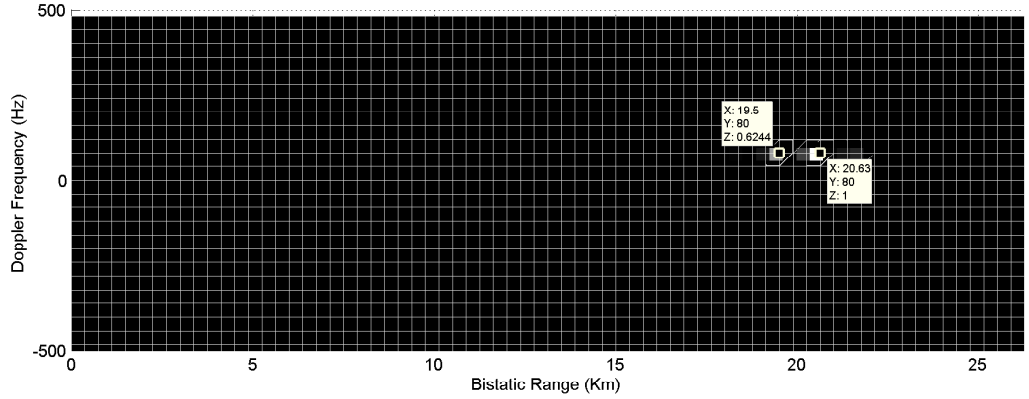

(c)

Figure 4.15: Simulation result of two close targets with $p_{(1,2)} = 80$ Hz, $l_1 = 19.5$ and $l_2 = 20,63$ km for multiple FM channels based CLS method: (a) 3D plot; (b) bistatic range plot; (c) view from the top.

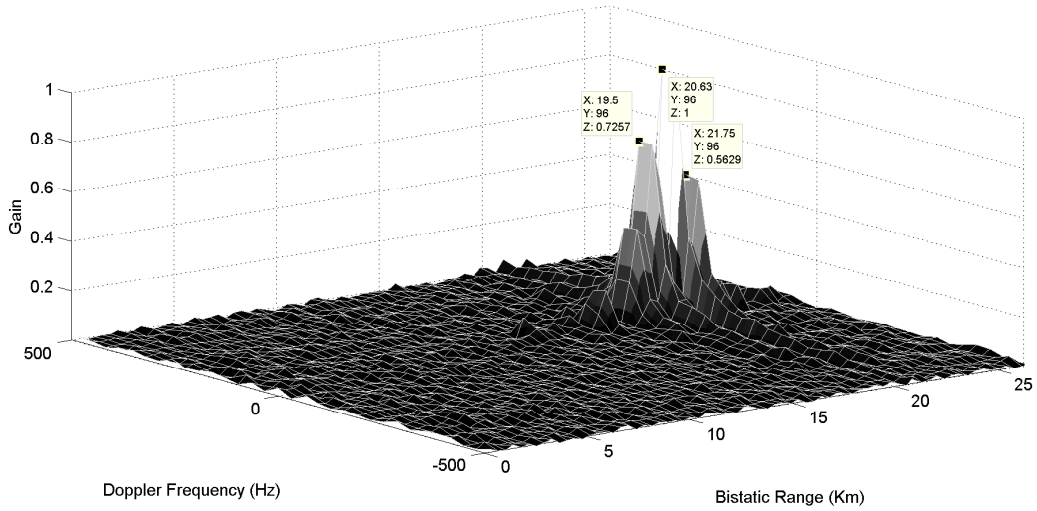

(a)

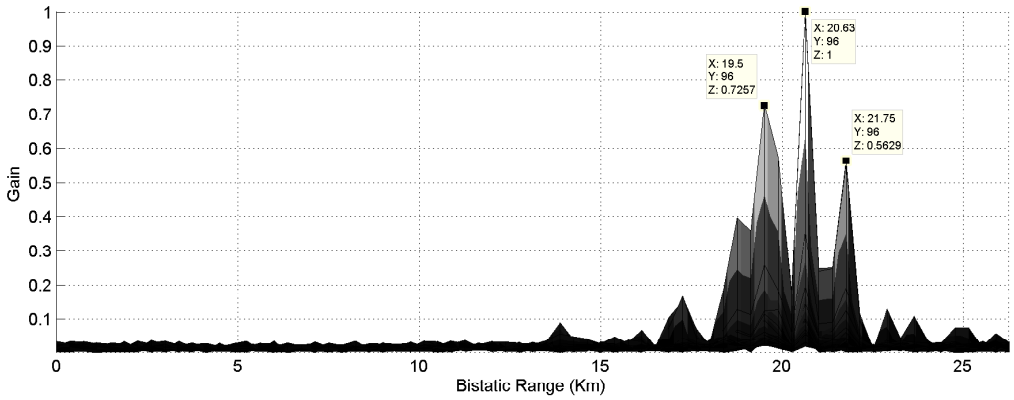

(b)

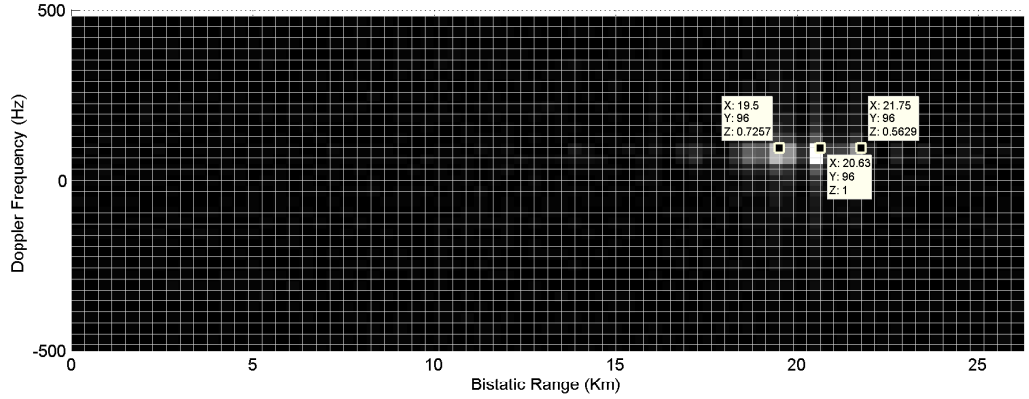

(c)

Figure 4.16: Simulation result of three close targets with $p_{(1,2,3)} = 96$ Hz, $l_1 = 19.5$, $l_2 = 20.63$ and $l_3 = 21.75$ km for multiple FM channels based normal AF: (a) 3D plot; (b) bistatic range plot; (c) view from the top.

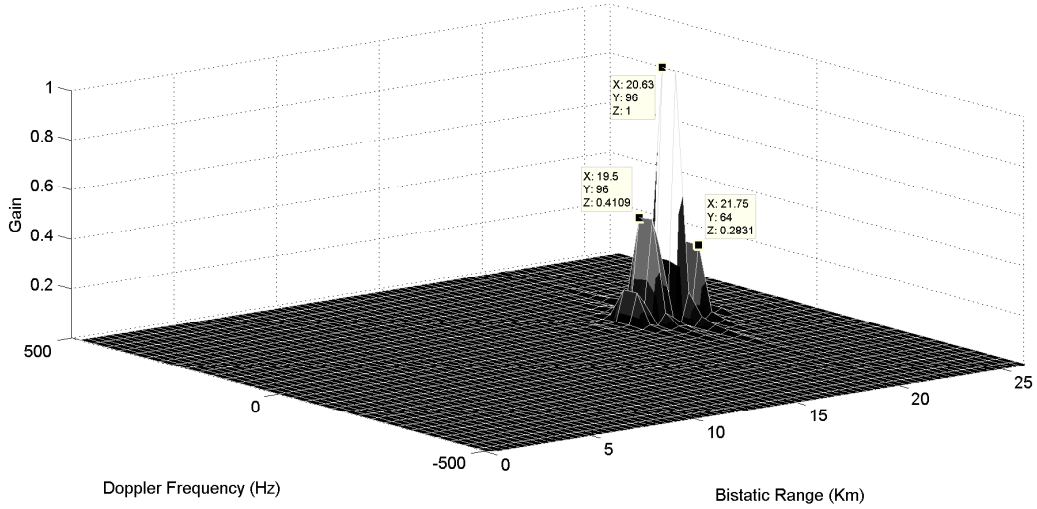

(a)

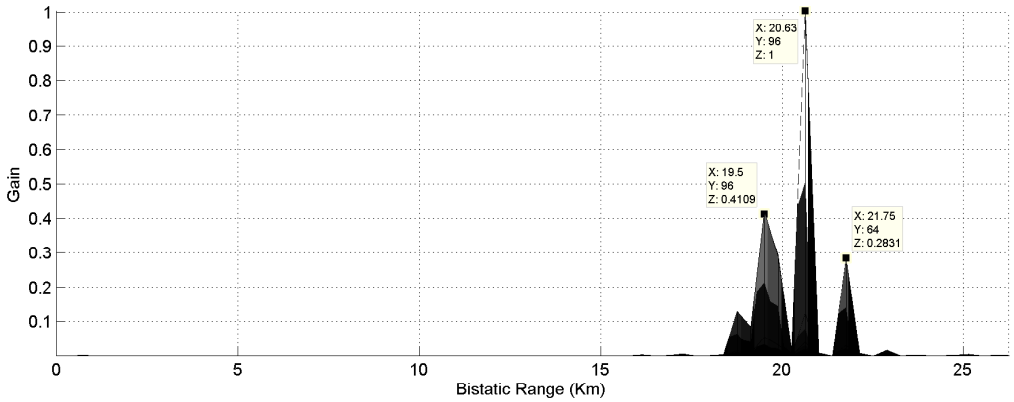

(b)

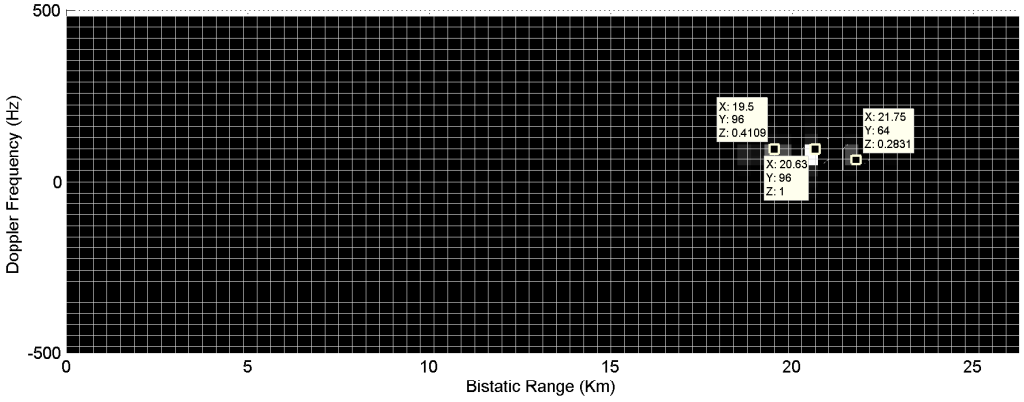

(c)

Figure 4.17: Simulation result of three close targets with $p_{(1,2,3)} = 96$ Hz, $l_1 = 19.5$, $l_2 = 20.63$ and $l_3 = 21.75$ km for multiple FM channels based CLS method: (a) 3D plot; (b) bistatic range plot; (c) view from the top.

4.3 Summary

This chapter discusses whether the recently developed correlation methods can be used in PBR systems. We show that correlation methods can be used instead of the AF for target detection. However the proposed methods have high computational cost compared to the AF based approaches because the AF is computed using the FFT algorithm. MIC, Pearson, Spearman's rank correlation coefficients are the methods used in this thesis. In addition, a new method called Cross-term free Least Squares (CLS) method is proposed and compared with others. Best results are observed with the CLS method. It is experimentally observed that it is possible to resolve close targets when multichannel FM data is used. The advantage of the CLS method compared to AF based approaches is that superious peaks do not appear in the proposed CLS method.

CLS method are also used to detect two close targets with multiple FM channels based signals and one FM channel. Even though one FM channel based PBR system with CLS method can not separate targets, multiple channel system can successfully detect both targets.

Chapter 5

Conclusion and Future Work

Passive bistatic radar (PBR) systems have received major attention from the scientific community in recent years. In this thesis, new target detection methods are introduced and their properties are studied through simulations.

In practice, the AF is corrupted by noise. This especially affects the low SNR-valued targets. The 2-D range-Doppler map is considered as a desired function to be denoised or to be reconstructed from random compressive measurements. As a result, compressive sensing algorithms are used to denoise the AF and PES-ℓ_1 denoising method which does not use any measurement matrix is proposed. The CS approach removes the noise in the AF. However, it may also remove weak targets. To observe the weak targets a large number of measurements are necessary. As a result, the computational cost is high because the matrix multiplication becomes a major burden due to the random nature of the measurement matrix. On the other hand PES-ℓ_1 which is a sparsity based denoising method does not require any measurement computations and it successfully reduces noise and detects weak targets. PES-ℓ_1 can be used in practical systems.

In the second part of thesis, different correlation methods are used to compare the surveillance and time delayed frequency shifted replica of the reference signal. Maximal Information Coefficient (MIC), Pearson correlation coefficient, Spearman's rank correlation coefficient are used for the target detection. However,

they do not produce any improvement over the ordinary AF method.

This thesis proposes a new method called Cross-term free Least Squares (CLS) which outperforms other correlation algorithms in terms of PSNR and SNR. The CLS method is based on least squares coefficients of real and imaginary parts of predicting the surveillance signal using the modulated reference signal. It is observed that close targets can be detected by using CLS method in multichannel based PBR systems. The advantage of the CLS method compared to the ordinary AF approach is that superious peaks do not appear in the range-Doppler map. Computational cost of CLS method is high but it can be used together with the ordinary AF method on suspected superious peak locations.

5.1 Future Work

Unfortunately, we could not use real data in this thesis. Algorithms developed in this thesis will be tested with real data in the near future.

Bibliography

[1] C. J. Baker, "Passive radar-1." `http://esl.eng.ohio-state.edu/~cbaker/`. 03/07/2014.

[2] M. Jackson, "The geometry of bistatic radar systems," *IEE Proceedings Communications, Radar and Signal Processing*, vol. 133, no. 7, pp. 604–612, 1986.

[3] H. Griffiths, "From a different perspective: principles, practice and potential of bistatic radar," in *2003. Proceedings of the International Radar Conference*, pp. 1–7, IEEE, 2003.

[4] J. M. Christiansen, "DVB-T based passive bistatic radar: Simulated and experimental data analysis of range and doppler walk," 2009.

[5] N. J. Willis, *Bistatic Radar*. SciTech Publishing, 2005.

[6] P. Howland, "Editorial: Passive radar systems," in *IEE Proceedings Radar, Sonar and Navigation*, vol. 152, pp. 105–106, IET, 2005.

[7] M. Kaczur, "Passive coherent location," in *Proceedings of the 13th WSEAS International Conference on Mathematical and Computational Methods in Science and Engineering*, pp. 233–236, World Scientific and Engineering Academy and Society (WSEAS), 2011.

[8] B. Chambers, "Symmetrical radar absorbing structures," *Electronics Letters*, vol. 31, no. 5, pp. 404–405, 1995.

[9] H. Griffiths, "New directions in bistatic radar," in *IEEE Radar Conference, RADAR'08*, pp. 1–6, IEEE, 2008.

[10] H. Griffiths, "Passive bistatic radar," *RTO Educational Notes-Lecture Series RTO-EN-SET-133 Waveform Diversity for Advanced Radar Systems, Brno*, 2009.

[11] C. Coleman and H. Yardley, "Passive bistatic radar based on target illuminations by digital audio broadcasting," *IET Radar, Sonar & Navigation*, vol. 2, no. 5, pp. 366–375, 2008.

[12] A. G. Westra, "Radar versus stealth: Passive radar and the future of US military power," tech. rep., DTIC Document, 2009.

[13] H. Griffiths and C. Baker, "Passive coherent location radar systems. part 1: performance prediction," in *IEE Proceedings Radar, Sonar and Navigation*, vol. 152, pp. 153–159, IET, 2005.

[14] M. A. Ringer and G. J. Frazer, "Waveform analysis of transmissions of opportunity for passive radar," in *Proceedings of the Fifth International Symposium on Signal Processing and Its Applications. ISSPA'99*, vol. 2, pp. 511–514, IEEE, 1999.

[15] C. Baker, H. Griffiths, and I. Papoutsis, "Passive coherent location radar systems. part 2: Waveform properties," *IEE Proceedings Radar, Sonar and Navigation*, vol. 152, no. 3, pp. 160–168, 2005.

[16] P. E. Howland, D. Maksimiuk, and G. Reitsma, "Fm radio based bistatic radar," *IEE Proceedings-Radar, Sonar and Navigation*, vol. 152, no. 3, pp. 107–115, 2005.

[17] R. Nitzberg, "Radar signal processing and adaptive systems(book)," *Norwood, MA: Artech House*, 1999.

[18] T. K. Moon and W. C. Stirling, *Mathematical methods and algorithms for signal processing*, vol. 1. Prentice Hall, New York, 2000.

[19] F. Colone, R. Cardinali, and P. Lombardo, "Cancellation of clutter and multipath in passive radar using a sequential approach," in *IEEE Conference on Radar*, pp. 7–pp, IEEE, 2006.

[20] K. Kulpa and Z. Czekala, "Ground clutter suppression in noise radar," in *Proc. Int. Conf. RADAR*, pp. 18–22, 2004.

[21] S. Haykin, "Adaptive filter theory," 2000.

[22] R. Cardinali, F. Colone, C. Ferretti, and P. Lombardo, "Comparison of clutter and multipath cancellation techniques for passive radar," in *IEEE Radar Conference*, pp. 469–474, IEEE, 2007.

[23] M. H. Hayes, "9.4: Recursive least squares," *Statistical Digital Signal Processing and Modeling*, p. 541, 1996.

[24] A. Di Lallo, A. Farina, R. Fulcoli, P. Genovesi, R. Lalli, and R. Mancinelli, "Design, development and test on real data of an fm based prototypical passive radar," in *IEEE Radar Conference*, pp. 26–30, 2008.

[25] H. Rohling, "Radar CFAR thresholding in clutter and multiple target situations," *IEEE Transactions on Aerospace and Electronic Systems*, no. 4, pp. 608–621, 1983.

[26] R. G. Baraniuk, "Single-pixel imaging via compressive sampling," *IEEE Signal Processing Magazine*, vol. 25, no. 2, pp. 83–91, 2008.

[27] M. Lustig, D. Donoho, and J. M. Pauly, "Sparse MRI: The application of compressed sensing for rapid MR imaging," *Magnetic resonance in medicine*, vol. 58, no. 6, pp. 1182–1195, 2007.

[28] W. Bajwa, J. Haupt, A. Sayeed, and R. Nowak, "Compressive wireless sensing," in *Proceedings of the 5th International Conference on Information Processing in Sensor Networks*, pp. 134–142, ACM, 2006.

[29] C. R. Berger, Z. Wang, J. Huang, and S. Zhou, "Application of compressive sensing to sparse channel estimation," *IEEE Communications Magazine*, vol. 48, no. 11, pp. 164–174, 2010.

[30] R. Baraniuk and P. Steeghs, "Compressive radar imaging," in *Radar Conference, 2007 IEEE*, pp. 128–133, IEEE, 2007.

[31] V. M. Patel, G. R. Easley, D. M. Healy Jr, and R. Chellappa, "Compressed synthetic aperture radar," *IEEE Journal of Selected Topics in Signal Processing*, vol. 4, no. 2, pp. 244–254, 2010.

[32] O. Teke, A. C. Gurbuz, and O. Arikan, "A robust compressive sensing based technique for reconstruction of sparse radar scenes," *Digital Signal Processing*, vol. 27, pp. 23–32, 2013.

[33] O. Teke, "Robust compressive sensing techniques," Master's thesis, Bilkent University, 2014.

[34] M. Herman and T. Strohmer, "Compressed sensing radar," in *IEEE Radar Conference, RADAR'08*, pp. 1–6, 2008.

[35] J. H. Ender, "On compressive sensing applied to radar," *Signal Processing*, vol. 90, no. 5, pp. 1402–1414, 2010.

[36] J. A. Tropp and A. C. Gilbert, "Signal recovery from random measurements via orthogonal matching pursuit," *IEEE Transactions on Information Theory*, vol. 53, no. 12, pp. 4655–4666, 2007.

[37] D. Needell and J. A. Tropp, "CoSaMP: Iterative signal recovery from incomplete and inaccurate samples," *Applied and Computational Harmonic Analysis*, vol. 26, no. 3, pp. 301–321, 2009.

[38] T. Blumensath and M. E. Davies, "Iterative hard thresholding for compressed sensing," *Applied and Computational Harmonic Analysis*, vol. 27, no. 3, pp. 265–274, 2009.

[39] A. E. Cetin, A. Bozkurt, O. Gunay, Y. H. Habiboglu, K. Kose, I. Onaran, R. A. Sevimli, and M. Tofighi, "Projections onto convex sets (POCS) based optimization by lifting," *IEEE GlobalSIP 2013, Austin, Texas, USA*, 2013.

[40] G. Chierchia, N. Pustelnik, J.-C. Pesquet, and B. Pesquet-Popescu, "Epigraphical projection and proximal tools for solving constrained convex optimization problems: Part , journal = CoRR, volume = abs/1210.5844, year = 2012, ee = http://arxiv.org/abs/1210.5844, bibsource = DBLP, http://dblp.uni-trier.de,"

[41] "Compressive sensing resources." `http://dsp.rice.edu/cs/`. 03/07/2014.

[42] D. Malioutov, M. Çetin, and A. S. Willsky, "A sparse signal reconstruction perspective for source localization with sensor arrays," *IEEE Transactions on Signal Processing*, vol. 53, no. 8, pp. 3010–3022, 2005.

[43] L. C. Potter, E. Ertin, J. T. Parker, and M. Cetin, "Sparsity and compressed sensing in radar imaging," *Proceedings of the IEEE*, vol. 98, no. 6, pp. 1006–1020, 2010.

[44] R. G. Baraniuk, "Compressive sensing [lecture notes]," *Signal Processing Magazine, IEEE*, vol. 24, no. 4, pp. 118–121, 2007.

[45] E. J. Candes, J. K. Romberg, and T. Tao, "Stable signal recovery from incomplete and inaccurate measurements," *Communications on Pure and Applied Mathematics*, vol. 59, no. 8, pp. 1207–1223, 2006.

[46] J. Haupt and R. Nowak, "Signal reconstruction from noisy random projections," *IEEE Transactions on Information Theory*, vol. 52, no. 9, pp. 4036–4048, 2006.

[47] C. R. Berger, B. Demissie, J. Heckenbach, P. Willett, and S. Zhou, "Signal processing for passive radar using ofdm waveforms," *IEEE Journal of Selected Topics in Signal Processing*, vol. 4, no. 1, pp. 226–238, 2010.

[48] P. Breen, "Algorithms for sparse approximation," *Project, School of Mathematics University of Edinburgh*, 2009.

[49] T. Blumensath and M. E. Davies, "Iterative thresholding for sparse approximations," *Journal of Fourier Analysis and Applications*, vol. 14, no. 5-6, pp. 629–654, 2008.

[50] A. E. Cetin and M. Tofighi, "Denosing using wavelets and projections onto the l1-ball," *ArXiv e-prints 1406.2528*, Jun 2014.

[51] M. Tofighi, K. Kose, and A. Cetin, "Denoising using projections onto the epigraph set of a convex cost function," *IEEE 21st International Conference on Image Processing (ICIP2014)*, Oct 2014.

[52] K. Kose, V. Cevher, and A. E. Cetin, "Filtered variation method for denoising and sparse signal processing," in *IEEE International Conference on Acoustics, Speech and Signal Processing (ICASSP), 2012*, pp. 3329–3332, IEEE, 2012.

[53] C. F. Dietrich, *Uncertainty, Calibration and Probability: The Statistics of Scientific and Industrial Measurement, 331 p.* CRC Press, 1991.

[54] J. S. Bendat and A. G. Piersol, "Engineering applications of correlation and spectral analysis," *New York, Wiley-Interscience, 1980. 315 p.*, vol. 1, 1980.

[55] J. B. Kinney and G. S. Atwal, "Equitability, mutual information, and the maximal information coefficient," *Proceedings of the National Academy of Sciences*, vol. 111, no. 9, pp. 3354–3359, 2014.

[56] D. Reshef, Y. Reshef, M. Mitzenmacher, and P. Sabeti, "Equitability analysis of the maximal information coefficient, with comparisons," *arXiv preprint arXiv:1301.6314*, 2013.

[57] S. Jackson, *Research Methods and Statistics: A Critical Thinking Approach, 159-162 p.* Cengage Learning, 2011.

[58] G. J. Borradaile, *Statistics of Earth Science Data: Their Distribution in Time, space and orientation, 159 p.* Springer, 2003.

[59] D. N. Reshef, Y. A. Reshef, H. K. Finucane, S. R. Grossman, G. McVean, P. J. Turnbaugh, E. S. Lander, M. Mitzenmacher, and P. C. Sabeti, "Detecting novel associations in large data sets," *Science*, vol. 334, no. 6062, pp. 1518–1524, 2011.

[60] A. S. Tasdelen, "Range resolution improvement in passive coherent location radar systems using multiple fm radio channels," Master's thesis, Bilkent University, 2007.

[61] F. Colone, D. O'hagan, P. Lombardo, and C. Baker, "A multistage processing algorithm for disturbance removal and target detection in passive bistatic radar," *IEEE Transactions on Aerospace and Electronic Systems*, vol. 45, no. 2, pp. 698–722, 2009.

[62] L. Der, "Frequency modulation (FM) tutorial," *Silicon Laboratories Inc*, 2008.

[63] A. Lauri, F. Colone, R. Cardinali, C. Bongioanni, and P. Lombardo, "Analysis and emulation of fm radio signals for passive radar," in *IEEE Aerospace Conference*, pp. 1–10, IEEE, 2007.

APPENDIX A

Stereo FM Signal

Frequency Modulation (FM) bases on changing frequency characteristics of high-frequency carrier signal with the low-frequency message signal. In many countries, FM commercial broadcasts are quite common and used in 88-108 Mhz band. A typical FM radio occupies a bandwidth of about 100 kHz. FM signals have appealing features of very broad coverage and it is possible to get high transmit powers. You can either increase performance or decrease the development cost by using FM signals in PBR systems, so there is a good trade-off between them [61]. FM signals have very high-frequency signals in the air due to the high-frequency carrier signal. FM signals are assumed to be baseband signals after coming to antennas, and then these baseband signals are given as complex envelop to radar signal processing parts in our simulations.

Stereo FM signals are created using computed-based program, MATLAB R2013b. In Turkey and some countries, stereo FM has been widely used for radio broadcasting although many countries join the Digital Audio Broadcasting (DAB). It is important to know that we have two channels, such as left (L) and right (R). These channels are summed (L+R) and subtracted (L-R) because they should be compatible with mono receivers. The modulation signal equation for

stereo FM signal is given by

$$m(t) = 0.9 \left[\frac{L+R}{2} + \frac{L-R}{2} sin(4\pi f_p t) \right] + 0.1 \; sin(2\pi f_p t), \tag{A.1}$$

where L and R are audio signals, $f_p = 19KHz$ is is the frequency of pilot tone. To simulate stereo FM better, left and right channels are generated randomly [62]. The modulation signal that we generated in Equation A.1 is inserted to the following equation:

$$s(t) = cos(2\pi k_f m(t)) + j.sin(2\pi k_f m(t)), \tag{A.2}$$

where k_f is the maximum frequency deviation. Equation A.2 gives us complex baseband signal, then we use it as transmit signal [63]. When we generate the modulated signal, $m(t)$, the sampling frequency, $f_s = 200$ kHz, modulated signal bandwidth, $B_m = 10$ kHz, and receiver bandwidth, $B_r = 100$ kHz are taken. Why we use this sampling frequency is that FM radio use bandwidth of 100 kHz as said before, so we should take sampling frequency 200 kHz at least because of Nyquist theorem.

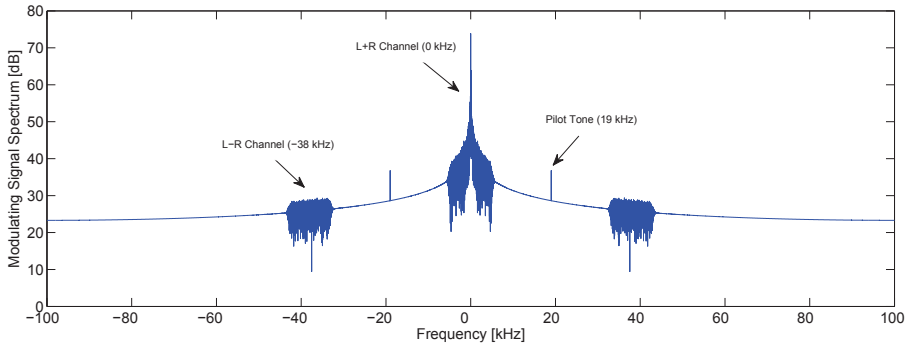

(a)

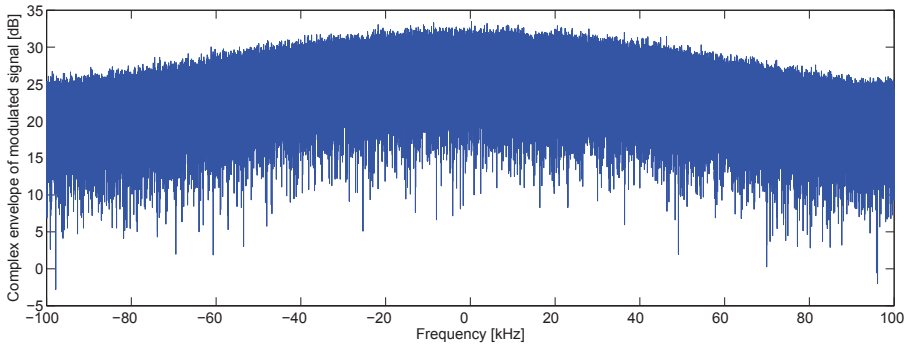

(b)

Figure A.1: Generating stereo FM signal: (a) Modulated signal spectrum;(b) Complex envelope of modulated signal;